A coupled theory for diffusion of hydrogen and large elastic-plastic deformations of metals

by

Claudio V. Di Leo

S.B., Massachusetts Institute of Technology (2010)

Submitted to the Department of Mechanical Engineering
in partial fulfillment of the requirements for the degree of

Master of Science

at the

Massachusetts Institute of Technology

June 2012

Author ....
Department of Mechanical Engineering
May 5, 2012

Certified by ....
Lallit Anand
Warren and Towneley Rohsenow Professor of Mechanical Engineering
Thesis Supervisor

Accepted by ....
David E. Hardt
Chairman, Department Committee on Graduate Students

A coupled theory for diffusion of hydrogen and large elastic-plastic deformations of metals

by

Claudio V. Di Leo

Submitted to the Department of Mechanical Engineering
on May 5, 2012, in partial fulfillment of the
requirements for the degree of
Master of Science

Abstract

A thermodynamically-consistent coupled-theory which accounts for diffusion of hydrogen, trapping of hydrogen, diffusion of heat, and large elastic-plastic deformations of metals is developed. Our theoretical framework places the widely-used notion of an "equilibrium" between hydrogen residing in normal interstitial lattice sites and hydrogen trapped at microstructural defects, within a thermodynamically-consistent framework. The theory has been numerically implemented in a finite element program. Using the numerical capability we study two important problems. First, we show the importance of using a prescribed chemical potential boundary condition in modeling the boundary between a metal system and a hydrogen atmosphere at a given partial pressure and temperature; specifically, we perform simulations using this boundary condition and compare our simulations to those in the published literature. Secondly, the effects of hydrogen on the plastic deformation of metals is studied through simulations of plane-strain tensile deformation and three-point bending of U-Notched specimens. Our simulations on the effects of hydrogen on three-point bending of U-notched specimens are shown to be in good qualitative agreement with published experiments.

Thesis Supervisor: Lallit Anand
Title: Warren and Towneley Rohsenow Professor of Mechanical Engineering

Acknowledgments

First and foremost I would like to thank my advisor Professor Lallit Anand. I have been inspired by his precise and rigorous treatment of the field of solid mechanics and I will continue to draw upon the skills I have learned from him for many years to come.

My colleagues at the mechanics and materials group have provided me with invaluable knowledge and friendship. I would particularly like to thank Kaspar Loeffel, Dr. David Henann, and Dr. Shawn Chester for many fruitful discussions. Dr. Vikas Srivastava was my mentor as an undergraduate research assistant and inspired me to pursue further studies in graduate school, I owe a special debt of gratitude to him. Additionally, I would like to thank Ray Hardin for his help with various administrative issues.

I thank my family, especially my parents, for always making me strive to become a better man. Through example, they have taught me that there is nothing you can not achieve if you work hard. Finally, I thank my wife Lea, she gives meaning and purpose to all my efforts.

Contents

List of Figures 11

List of Tables 13

1 Introduction 15

2 Theoretical framework 19

2.1 Introduction 19
2.2 Notation 19
2.3 Kinematics 19
2.3.1 Standard kinematics 19
2.3.2 An additional microvariable e^p 22
2.4 Frame-indifference 22
2.5 Development of the theory based on the principle of virtual power 23
2.5.1 Principle of virtual power 24
2.5.2 Frame-indifference of the internal power and its consequences 25
2.5.3 Macroscopic force balance 26
2.5.4 Microscopic force balances 27
2.6 Balance law for the diffusion of hydrogen 28
2.7 Balance of energy. Entropy imbalance. Free-energy imbalance 29
2.8 Constitutive theory 31
2.8.1 Basic constitutive equations 31
2.8.2 Thermodynamic restrictions 32
2.8.3 Dissipative constitutive equations 33
2.8.4 Further consequences of thermodynamics 35
2.9 Isotropy 37
2.9.1 Isotropy of the reference configuration 37
2.9.2 Isotropy of the intermediate structural space 38
2.9.3 Isotropic free energy 39
2.10 Summary 42
2.10.1 Constitutive equations 43
2.10.2 Governing partial differential equations 45

2.11 Specialization of the constitutive equations 47
  2.11.1 Free energy 47
  2.11.2 Hydrogen trapping 49
  2.11.3 Microscopic stresses. Microforce balance 51
  2.11.4 Plastic flow resistance 52
  2.11.5 Heat flux 53
  2.11.6 Lattice hydrogen flux 53
  2.11.7 Balance of lattice chemical potential μ_L 54
2.12 Governing partial differential equations for the specialized constitutive equations. Boundary conditions 55
2.13 Numerical implementation 57
2.14 Concluding remarks 58

3 Hydrogen transport near a blunting crack tip **59**
3.1 Introduction 59
3.2 Chemical potential boundary condition 59
3.3 Effect of the chemical potential boundary condition on hydrogen transport near a blunting crack tip 61
  3.3.1 Results using a constant chemical potential boundary condition 64
  3.3.2 Results using a zero flux boundary condition 70
3.4 Concluding remarks 73

4 Effects of hydrogen on the plastic deformation of metals **75**
4.1 Introduction 75
4.2 Effects of hydrogen in plane strain tension 76
  4.2.1 Mesh insensitivity 78
4.3 Effects of hydrogen on three-point bending of a U-notched specimen 87
  4.3.1 Effect of the regularization parameters l and Z on the formation of shear bands in the hydrogen-charged simulations 89
  4.3.2 Effect of the variation in initial yield strength Y_0 89
4.4 Concluding remarks 98

5 Conclusion **99**
5.1 Summary 99
5.2 Future work 100

Bibliography **101**

A Non-equilibrium trapping of hydrogen **105**

B Details on the numerical implementation **107**
B.1 Variational formulation of the macroscopic force balance 107
B.2 Variational formulation for the balance of lattice chemical potential 109
B.3 Variational formulation for the transient heat equation 113
B.4 Variational formulation of the microscopic force balance 115
B.5 Time integration procedure 116

B.5.1 Summary of time-integration procedure 120
B.6 Jacobian matrix 122
B.6.1 Elastic jacobian matrix 122
B.6.2 Plastic jacobian matrix 123

List of Figures

3-1 Schematic of the blunt-crack geometry and boundary conditions used in studying the effects of the chemical potential boundary condition on hydrogen transport near a blunt-crack. . . . 63
3-2 Hydrostatic stress and equivalent tensile plastic strain ahead of the crack tip after loading. . . . 66
3-3 Lattice hydrogen concentration ahead of the crack tip at different times with the use of a constant lattice chemical potential boundary condition. . . . 67
3-4 Lattice chemical potential ahead of the crack tip at different times with the use of a constant lattice chemical potential boundary condition. . . . 67
3-5 Lattice hydrogen concentration ahead of the crack tip at the end of loading for different loading rates with the use of a constant lattice chemical potential boundary condition. . . . 68
3-6 Trapped hydrogen concentration and trapped hydrogen site fraction at the end of loading for different loading rates with the use of a constant lattice chemical potential boundary condition. . . . 69
3-7 Lattice hydrogen concentration ahead of the crack tip at the end of loading for different loading rates with the use of a zero flux boundary condition. . . . 71
3-8 Lattice chemical potential ahead of the crack tip at different times with the use of a zero flux boundary condition. . . . 71
3-9 Trapped hydrogen concentration and trapped hydrogen site fraction at the end of loading for different loading rates with the use of a zero flux boundary condition. . . 72

4-1 Schematic of the geometry and finite element mesh used for plane-strain tension simulations. . . . 79
4-2 Contours of total hydrogen concentration prior to mechanical loading for plane-strain tension simulations. . . . 81
4-3 Contours of total, lattice, and trapped hydrogen concentration at two different nominal end displacements for plane-strain tension simulations. . . . 82
4-4 Contours of equivalent tensile plastic strain for plane-strain tension simulations of hydrogen-charged and uncharged specimens. . . . 83
4-5 Engineering stress versus strain curves for plane-strain tension simulations of hydrogen-charged and uncharged specimens. . . . 83

4-6 Finite element meshes used for studying mesh sensitivity. 84
4-7 Contours of equivalent tensile plastic strain for plane-strain tension simulations with different finite-element meshes. 85
4-8 Engineering stress versus strain curves for plane-strain tension simulations with different finite-element meshes. 86
4-9 Schematic and finite-element mesh used in the U-notched three-point bending simulations. 90
4-10 Contours of total hydrogen concentration for three-point bending simulations before loading. 90
4-11 Initial variation in the yield strength Y_0 for three-point bending simulations. 91
4-12 Contours of equivalent tensile plastic strain for three-point bending simulations of a hydrogen-charged and an uncharged U-notched metal specimen. 92
4-13 Contours of equivalent tensile plastic strain near the notch for three-point bending simulations of a hydrogen-charged and an uncharged U-notched metal specimen. . . 93
4-14 Force versus mid-span deflection curves for three-point bending simulations of a hydrogen-charged and an uncharged U-notched metal specimen. 94
4-15 Contours of equivalent tensile plastic strain for three-point bending simulations of a hydrogen-charged U-Notched metal specimen at different times during loading. . . . 95
4-16 Contours of equivalent tensile plastic strain for three-point bending simulations of a hydrogen-charged U-notched metal specimen while varying the gradient regularization parameters. 96
4-17 Initial yield strength prior to mechanical loading and contours of equivalent tensile plastic strain for simulations with and without a random variation in the initial yield strength. 97

A-1 Schematic of the energy landscape for hydrogen trapping. 106

List of Tables

4.1 Initial and boundary conditions for the lattice chemical potential in the plane-strain tension simulations. 77
4.2 Representative material properties for a BCC Iron system. 80
4.3 Initial and boundary conditions for the lattice chemical potential in the three-point bending simulations. 88

Chapter 1

Introduction

Hydrogen is expected to play an increasingly important role in the development of a “clean” source of energy.[1] However, hydrogen is a gas at ambient conditions, and the storage and distribution of hydrogen in its molecular or atomic form is a technological challenge which must be overcome in order to make this source of energy economically viable (cf., e.g., Züttel et al., 2010; Zheng et al., 2011). Atomic hydrogen, being the smallest of gaseous impurities, readily dissolves in and permeates through most materials. Hydrogen dissolution and permeation can be significant at high pressures, and since hydrogen can have deleterious effects on a material it may affect the integrity of structural components used for hydrogen storage and distribution.

Accordingly, it is important to understand and model the coupled diffusion-mechanics response of metallic components used to contain this gas, and this topic is receiving increasing attention because of its potential application to the development of large-scale production, storage, and distribution of hydrogen (cf., e.g., San Marchi et al., 2007; Dadfarnia et al., 2009).

The deleterious effects of hydrogen on the mechanical response of iron and steel are well-known (cf., e.g. Hirth, 1980). The precise microscopic mechanisms by which hydrogen embrittles steels are still not very well understood or modeled. As reviewed by Dadfarnia et al. (2010), research to date has identified two possible mechanisms for hydrogen embrittlement at room temperature: (i) hydrogen-enhanced localized plasticity (HELP), and (ii) hydrogen-induced decohesion (HID). The HELP mechanism is based on the observation that hydrogen reduces the strength of the barriers to dislocation motion and thus enhances the mobility of dislocations. This leads to a reduction in the resistance to plastic flow in regions where the hydrogen concentration is locally high. The precise mechanism by which hydrogen embrittles steels continues to be the focus of intensive theoretical and experimental research (cf., e.g., Ramasubramaniam et al., 2008; Serebrinsky et al., 2004; Novak et al., 2010; Dadfarnia et al., 2010) and is *not the focus of this work.* Instead, our focus here is on the development of a thermodynamically-consistent continuum-level theory for the diffusion of hydrogen coupled with the thermo-elastic-plastic response of materials. The development of such

---

[1] Hydrogen is produced from water by electricity through an electrolyser, and the hydrogen so-produced is a “renewable” fuel only if its produced directly from solar light, or indirectly from a renewable source, e.g., wind- or hydro-power Züttel et al. (2010).

a theory is an *essential* prerequisite to any attempt to address the issue of hydrogen-embrittlement related failures in structural components.

It has long been observed that there is an asymmetry between the kinetics of absorption and the kinetics of evolution of hydrogen in steels, in that absorption proceeds with a larger apparent diffusivity than does evolution. This asymmetry in diffusivities is attributed to trapping of the hydrogen atoms at various microstructural "trapping sites," which include interfaces between the matrix and various second-phase particles, grain boundaries, and dislocation cores. A widely-used micro-mechanical model for describing the asymmetry in diffusivities is that of Oriani (1970). His model is based on a crucial assumption regarding the effects of the microstructure on hydrogen transport and trapping. Oriani postulated that within a continuum-level material point, and for a specific range of trap binding energies, the microstructure affects the local distribution of hydrogen in a manner such that the population of hydrogen in trapping sites is always in *equilibrium* with the population associated with normal interstitial lattice sites.

One of the earliest papers which attempts to couple nonlinear diffusion of hydrogen with large elastoplastic deformation of metals is the seminal paper of Sofronis and McMeeking (1989), who formulated a theory which has Oriani's postulate of "local equilibrium" as one of its central arguments. The theory of Sofronis and McMeeking was extended by Krom et al. (1999) to account for the effects of an increase in the number of trapping sites due to plastic deformation, and by Lufrano and Sofronis (1998) to account for lattice-dilatation due to the presence of hydrogen. These components are all present in the work of Taha and Sofronis (2001) which, with minor modifications, is at present most often used to analyze the effects of interactions of hydrogen transport, elastic-plastic deformation, lattice-dilatation, and hydrogen-induced reduction of the resistance to plastic flow. These coupled theories are not formulated in a thermodynamically-consistent manner and always have Oriani's postulate of "local equilibrium" as a central argument.

The purpose of this work is to develop a thermodynamically-consistent thermo-mechanically-coupled theory accounting for diffusion of hydrogen, trapping of hydrogen, diffusion of heat, and large elastic-plastic deformations within a modern continuum-mechanical framework. In formulating our theory, we limit our considerations to *isotropic materials* and develop a reasonably general theory in Sections 2.1 through 2.10 of Chapter 2. In Sections 2.11 and 2.12 of Chapter 2 we discuss a special set of constitutive equations which should be useful for applications. We have enhanced our theory with a strain-gradient component in order to avoid mesh-dependent results when modeling materials which plastically soften, this is important to the problem of hydrogen embrittlement of steels since the HELP mechanism suggests that the resistance to plastic flow should decrease in regions of high hydrogen content.

Our specialized theory is similar in spirit to that of Taha and Sofronis (2001), but has the following distinctive characteristics: (i) we do not use Oriani's hypothesis as a central argument to our theory of trapping; rather, based on thermodynamically consistent constitutive choices, we recover his argument as a special case of our theory; (ii) it is phrased entirely at the continuum-level; (iii) it is consistent with modern continuum thermodynamics; (iv) it is properly frame-indifferent; (v) it is not restricted to isothermal conditions.

In Chapters 3 and 4 we present numerical simulations using the chosen constitutive equations and compare our numerical results to some of the published literature. We close in Chapter 5 with a brief summary and listing some outstanding issues that need further research.

In Appendix A we illustrate how our theoretical framework may be used to model hydrogen trapping without the use of Oriani's hypothesis in a thermodynamically-consistent manner. In

Appendix B we provide details on the numerical implementation of our specialized constitutive theory.

Chapter 2

Theoretical framework

2.1 Introduction

In this chapter we present our thermodynamically-consistent continuum-level theory for the diffusion of hydrogen, trapping of hydrogen, and large elastic-plastic deformation of metals. In Sections 2.2 through 2.10 we present a relatively general theoretical framework. In Sections 2.11 and 2.12 we discuss a special set of constitutive equations which should be useful in applications.

2.2 Notation

We use standard notation of modern continuum mechanics (Gurtin et al., 2010). Specifically: ∇ and Div denote the gradient and divergence with respect to the material point $\mathbf{X}$ in the reference configuration; grad and div denote these operators with respect to the point $\mathbf{x} = \chi(\mathbf{X}, t)$ in the deformed body; a superposed dot denotes the material time-derivative. Throughout, we write $\mathbf{F}^{e-1} = (\mathbf{F}^e)^{-1}$, $\mathbf{F}^{e-\top} = (\mathbf{F}^e)^{-\top}$, etc. We write $\mathrm{tr}\,\mathbf{A}$, $\mathrm{sym}\,\mathbf{A}$, $\mathrm{skw}\,\mathbf{A}$, $\mathbf{A}_0$, and $\mathrm{sym}_0\mathbf{A}$ respectively, for the trace, symmetric, skew, deviatoric, and symmetric-deviatoric parts of a tensor $\mathbf{A}$. Also, the inner product of tensors $\mathbf{A}$ and $\mathbf{B}$ is denoted by $\mathbf{A}:\mathbf{B}$, and the magnitude of $\mathbf{A}$ by $|\mathbf{A}| = \sqrt{\mathbf{A}:\mathbf{A}}$.

2.3 Kinematics

2.3.1 Standard kinematics

Consider a macroscopically-homogeneous body B with the region of space it occupies in a fixed *reference configuration*, and denote by $\mathbf{X}$ an arbitrary material point of B. A *motion* of B is then a smooth one-to-one mapping $\mathbf{x} = \chi(\mathbf{X}, t)$, with *deformation gradient*, *velocity*, and *velocity gradient* given by

$$\mathbf{F} = \nabla\chi, \qquad \mathbf{v} = \dot{\chi}, \qquad \mathbf{L} = \mathrm{grad}\,\mathbf{v} = \dot{\mathbf{F}}\mathbf{F}^{-1}. \tag{2.1}$$

Following modern developments of large-deformation plasticity theory (cf., e.g., Anand and Gurtin, 2003; Gurtin and Anand, 2005), we assume that the deformation gradient $\mathbf{F}$ may be multiplicatively decomposed as (Kröner, 1960; Lee, 1969)

$$\mathbf{F} = \mathbf{F}^e\mathbf{F}^p. \tag{2.2}$$

Here, suppressing the argument t

- $\mathbf{F}^p(\mathbf{X})$ represents the *local* deformation of the material in an infinitesimal neighborhood of $\mathbf{X}$ due to "plastic" mechanisms. This local deformation carries the material into - and ultimately "pins" the material to - a *coherent structure* that resides in the *intermediate space* at $\mathbf{X}$ (as represented by the range $\mathbf{F}^p(\mathbf{X})$);
- $\mathbf{F}^e(\mathbf{X})$ represents the subsequent stretching and rotation of this coherent structure, and thereby represents an "elastic" mechanism.

We refer to $\mathbf{F}^p$ and $\mathbf{F}^e$ as the *plastic and elastic distortions.*

The deformation gradient $\mathbf{F}(\mathbf{X})$ maps material vectors to spatial vectors; thus consistent with (2.2), the domain of $\mathbf{F}^p(\mathbf{X})$ is the reference space, the space of material vectors, and the range of $\mathbf{F}^e(\mathbf{X})$ is the observed space, the space of spatial vectors. By (2.2) the output of $\mathbf{F}^p(\mathbf{X})$ must equal the input of $\mathbf{F}^e(\mathbf{X})$; that is

$$\text{the range of } \mathbf{F}^p(\mathbf{X}) = \text{the domain of } \mathbf{F}^e(\mathbf{X}) \overset{\text{def}}{=} \mathcal{I}(\mathbf{X}). \tag{2.3}$$

We refer to $\mathcal{I}(\mathbf{X})$ as the *intermediate space* for $\mathbf{X}$. Thus, for any material point $\mathbf{X}$, $\mathbf{F}^p(\mathbf{X})$ maps material vectors to vectors in $\mathcal{I}(\mathbf{X})$, and $\mathbf{F}^e(\mathbf{X})$ maps vectors in $\mathcal{I}(\mathbf{X})$ to spatial vectors.

By $(2.1)_3$ and (2.2)

$$\mathbf{L} = \mathbf{L}^e + \mathbf{F}^e\mathbf{L}^p\mathbf{F}^{e-1} \tag{2.4}$$

with

$$\mathbf{L}^e = \dot{\mathbf{F}}^e\mathbf{F}^{e-1}, \qquad \text{and} \qquad \mathbf{L}^p = \dot{\mathbf{F}}^p\mathbf{F}^{p-1}. \tag{2.5}$$

The elastic and plastic stretching and spin tensors are defined through

$$\left.\begin{aligned} \mathbf{D}^e &= \operatorname{sym}\mathbf{L}^e, \qquad & \mathbf{W}^e &= \operatorname{skw}\mathbf{L}^e, \\ \mathbf{D}^p &= \operatorname{sym}\mathbf{L}^p, \qquad & \mathbf{W}^p &= \operatorname{skw}\mathbf{L}^p. \end{aligned}\right\} \tag{2.6}$$

We assume that

$$J \overset{\text{def}}{=} \det\mathbf{F} > 0 \tag{2.7}$$

and hence, using (2.2),

$$J = J^eJ^p, \quad \text{where} \quad J^e \overset{\text{def}}{=} \det\mathbf{F}^e > 0 \quad \text{and} \quad J^p \overset{\text{def}}{=} \det\mathbf{F}^p > 0, \tag{2.8}$$

so that $\mathbf{F}^e$ and $\mathbf{F}^p$ are invertible.

The right polar decomposition of $\mathbf{F}^e$ is given by

$$\mathbf{F}^e = \mathbf{R}^e\mathbf{U}^e, \tag{2.9}$$

where $\mathbf{R}^e$ is a rotation, while $\mathbf{U}^e$ is a symmetric, positive-definite tensor with

$$\mathbf{U}^e = \sqrt{\mathbf{F}^{e\top}\mathbf{F}^e}. \tag{2.10}$$

The right elastic Cauchy-Green strain tensor is given by

$$\mathbf{C}^e = (\mathbf{U}^e)^2 = \mathbf{F}^{e\top}\mathbf{F}^e. \tag{2.11}$$

Differentiating (2.11) results in the following expression for the time rate of change of $\mathbf{C}^e$

$$\frac{1}{2}\dot{\mathbf{C}}^e = \mathrm{sym}(\mathbf{F}^{e\top}\dot{\mathbf{F}}^e), \tag{2.12}$$

a result that we reserve for later use.

We make two basic kinematical assumptions concerning plastic flow:

(i) First, we make the standard assumption that *plastic flow is incompressible*, so that

$$J^p = \det\mathbf{F}^p = 1 \qquad \text{and} \qquad \mathrm{tr}\,\mathbf{L}^p = \mathrm{tr}\,\mathbf{D}^p = 0. \tag{2.13}$$

Hence, using (2.8)

$$J = J^e. \tag{2.14}$$

(ii) Second, from the outset we limit our discussion to isotropic materials, for which it is widely assumed that plastic flow is *irrotational* in the sense that[1]

$$\mathbf{W}^p = \mathbf{0}. \tag{2.15}$$

Then, trivially, $\mathbf{L}^p \equiv \mathbf{D}^p$ and

$$\dot{\mathbf{F}}^p = \mathbf{D}^p\mathbf{F}^p. \tag{2.16}$$

Let

$$\dot{\bar{\epsilon}}^p \overset{\text{def}}{=} \sqrt{2/3}|\mathbf{D}^p| \tag{2.17}$$

define an *equivalent tensile plastic strain rate.*[2] Then, as is traditional, we define an *equivalent tensile plastic strain* by

$$\bar{\epsilon}^p(\mathbf{X},t) \overset{\text{def}}{=} \int_0^t \dot{\bar{\epsilon}}^p(\mathbf{X},\zeta)d\zeta, \quad \text{subject to the initial condition} \quad \bar{\epsilon}^p(\mathbf{X},0) = 0. \tag{2.18}$$

Whenever $|\mathbf{D}^p| \neq 0$,

$$\mathbf{N}^p = \frac{\mathbf{D}^p}{|\mathbf{D}^p|}, \quad \text{with} \quad \mathrm{tr}\,\mathbf{N}^p = 0, \tag{2.19}$$

defines the *plastic flow direction*, and therefore

$$\mathbf{D}^p = \sqrt{3/2}\dot{\bar{\epsilon}}^p\mathbf{N}^p. \tag{2.20}$$

---

[1] This assumption is based solely on pragmatic grounds: when discussing finite deformations for isotropic materials the theory without plastic spin is far simpler than one with plastic spin.

[2] This is a slight abuse in notation in the sense that $\dot{\bar{\epsilon}}^p$ is *not the material time derivative of* $\bar{\epsilon}^p$.

Using (2.1), (2.4), (2.5), (2.16), and (2.20) the rates $\dot{\chi}$, $\dot{\mathbf{F}}^e$, and $\dot{\bar{\epsilon}}^p$ are related through

$$(\nabla\dot{\chi})\mathbf{F}^{-1} = \dot{\mathbf{F}}^e\mathbf{F}^{e-1} + \sqrt{3/2}\dot{\bar{\epsilon}}^p\mathbf{F}^e\mathbf{N}^p\mathbf{F}^{e-1}, \tag{2.21}$$

a result that we reserve for later use.

2.3.2 An additional microvariable e^p

We view $\bar{\epsilon}^p$ as an isotropic measure of the past history of plastic strain in the material. For the purpose of **mathematical regularization and ease of computation** in the modeling of materials involving strain softening and localized deformation, following Anand et al. (2012) and Forest (2009), we introduce a positive-valued scalar microvariable e^p.

- The microvariable e^p serves as an additional microscopic kinematical degree of freedom in developing a gradient theory. Specifically, in contrast to traditional gradient theories which are based on $\bar{\epsilon}^p$ and $\nabla\bar{\epsilon}^p$, here we develop a theory which depends on $\bar{\epsilon}^p$, e^p, and the gradient ∇e^p of the microvariable e^p.

2.4 Frame-indifference

A change in frame, at each fixed time t, is a transformation - defined by a rotation $\mathbf{Q}(t)$ and a spatial point $\mathbf{y}(t)$ - which transforms spatial points $\mathbf{x}$ to spatial points

$$\begin{aligned}\mathbf{x}^* &= \mathcal{F}(\mathbf{x})\\ &= \mathbf{y}(t) + \mathbf{Q}(t)(\mathbf{x} - \mathbf{o}).\end{aligned} \tag{2.22}$$

The function $\mathcal{F}$ represents a rigid mapping of the observed space into itself, with $\mathbf{o}$ a fixed spatial origin. By (2.22) the transformation law for the motion $\mathbf{x} = \chi(\mathbf{X}, t)$ has the form

$$\chi^*(\mathbf{X}, t) = \mathbf{y}(t) + \mathbf{Q}(t)(\chi(\mathbf{X}, t) - \mathbf{o}). \tag{2.23}$$

Then, under a change in observer, the deformation gradient transforms according to

$$\mathbf{F}^* = \mathbf{Q}\mathbf{F}. \tag{2.24}$$

The reference configuration and the intermediate structural space are independent of the choice of such changes in frame; thus

$$\mathbf{F}^p \quad \text{is invariant under a change in frame,} \tag{2.25}$$

and, by (2.5),

$$\mathbf{L}^p \quad \text{and hence} \quad \mathbf{D}^p \quad \text{are invariant under a change in frame.} \tag{2.26}$$

Then, (2.2) and (2.24) yield the transformation law

$$\mathbf{F}^{e*} = \mathbf{Q}\mathbf{F}^e \tag{2.27}$$

and

$$\dot{\mathbf{F}}^{e*} = \mathbf{Q}\dot{\mathbf{F}}^{e} + \dot{\mathbf{Q}}\mathbf{F}^{e}. \tag{2.28}$$

Also, by $(2.5)_1$ and (2.28)

$$\mathbf{L}^{e*} = \mathbf{Q}\mathbf{L}^{e}\mathbf{Q}^{\top} + \dot{\mathbf{Q}}\mathbf{Q}^{\top} \tag{2.29}$$

and hence

$$\mathbf{D}^{e*} = \mathbf{Q}\mathbf{D}^{e}\mathbf{Q}^{\top}, \quad \text{and} \quad \mathbf{W}^{e*} = \mathbf{Q}\mathbf{W}^{e}\mathbf{Q}^{\top} + \dot{\mathbf{Q}}\mathbf{Q}^{\top}. \tag{2.30}$$

Further, by (2.9),

$$\mathbf{F}^{e*} = \mathbf{Q}\mathbf{R}^{e}\mathbf{U}^{e} \tag{2.31}$$

and we may conclude from the uniqueness of the polar decomposition that

$$\mathbf{R}^{e*} = \mathbf{Q}\mathbf{R}^{e}, \quad \text{and} \quad \mathbf{U}^{e}\,\text{is invariant}, \tag{2.32}$$

and on account of the definition (2.11)

$$\mathbf{C}^{e}\,\text{is invariant}. \tag{2.33}$$

Finally, the scalar microvariable e^p is invariant, and ∇e^p is also invariant since "∇" represents a gradient in the reference body.

2.5 Development of the theory based on the principle of virtual power

Following Anand et al. (2012) and the virtual-power method of Gurtin (2000, 2002) and Gurtin and Anand (2005, 2009) the theory presented here is based on the belief that

- the power expended by each independent "rate-like" kinematical descriport - $\dot{\boldsymbol{\chi}}$, $\dot{\mathbf{F}}^e$, $\dot{\bar{\epsilon}}^p$, $\dot{e}^p$, and $\nabla\dot{e}^p$ - be expressible in terms of an associated force system consistent with its own balance.

However, it is not apparent what forms the associated force balances should take. For that reason we determine these balances using the principle of virtual power. We note that the rates $\dot{\boldsymbol{\chi}}, \dot{\mathbf{F}}^e$, and $\dot{\bar{\epsilon}}^p$ are not independent but are constrained through

$$(\nabla\dot{\boldsymbol{\chi}})\mathbf{F}^{-1} = \dot{\mathbf{F}}^{e}\mathbf{F}^{e-1} + \sqrt{3/2}\,\dot{\bar{\epsilon}}^{p}\mathbf{F}^{e}\mathbf{N}^{p}\mathbf{F}^{e-1}, \tag{2.34}$$

which is reiterated from (2.21). Also, $\nabla\dot{e}^p$ is simply the material gradient of $\dot{e}^p$.

We denote by P an arbitrary part (subregion) of the reference body B with $\mathbf{n}_{\mathrm{R}}$ the outward unit normal on the boundary ∂P of P. With each evolution of the body we associate macroscopic and microscopic force systems. The macroscopic systems, which are standard, are defined by:

(a) a traction $\mathbf{t}_{\mathrm{R}}(\mathbf{n}_{\mathrm{R}})$ (for each unit vector $\mathbf{n}_{\mathrm{R}}$) that expends power over the velocity $\dot{\boldsymbol{\chi}}$ on the boundary of the part;

(b) a body force $\mathbf{b}_{0\mathrm{R}}$ that also expends power over $\dot{\boldsymbol{\chi}}$;[3]

---

[3] We neglect any inertial effects in the development of this theory.

(c) an elastic stress $\mathbf{S}^e$ that expends power over the elastic distortion rate $\dot{\mathbf{F}}^e$.

The microscopic systems, which are nonstandard, are defined by:

(a) a scalar positive-valued microscopic stress π that expends power over the equivalent tensile plastic strain rate $\dot{\bar{\epsilon}}^p$;

(b) a scalar microscopic stress p that expends power over the rate $\dot{\mathsf{e}}^p$ of the microvariable e^p;

(c) a vector microscopic stress $\boldsymbol{\xi}$ that expends power over the gradient $\nabla\dot{\mathsf{e}}^p$.

(d) a scalar microscopic traction $\chi(\mathbf{n}_{\rm R})$ (for each unit vector $\mathbf{n}_{\rm R}$) that expends power over $\dot{\mathsf{e}}^p$ on the boundary of the part;

We characterize the force systems through the manner in which these forces expend power. Given any part P, the power expended on P by material *external* to P is specified through $\mathcal{W}_{\rm ext}$, and the power expended *within* P is specified through $\mathcal{W}_{\rm int}$. Specifically,

$$\left.\begin{aligned} \mathcal{W}_{\rm ext}({\rm P}) &= \int\limits_{\partial{\rm P}} \mathbf{t}_{\rm R}(\mathbf{n}_{\rm R})\cdot\dot{\boldsymbol{\chi}}\,dA_{\rm R},+\int\limits_{\rm P}\mathbf{b}_{0\rm R}\cdot\dot{\boldsymbol{\chi}}\,dV_{\rm R}+\int\limits_{\partial{\rm P}}\chi(\mathbf{n}_{\rm R})\dot{\mathsf{e}}^p\,dA_{\rm R},\\ \mathcal{W}_{\rm int}({\rm P}) &= \int\limits_{\rm P}\Big(\mathbf{S}^e:\dot{\mathbf{F}}^e+\pi\dot{\bar{\epsilon}}^p+\mathsf{p}\dot{\mathsf{e}}^p+\boldsymbol{\xi}\cdot\nabla\dot{\mathsf{e}}^p\Big)\,dV_{\rm R}, \end{aligned}\right\} \tag{2.35}$$

where $\mathbf{S}^e, \pi, \mathsf{p}$ and $\boldsymbol{\xi}$ are defined over the body for all time.

2.5.1 Principle of virtual power

Assume that, at some arbitrarily chosen but *fixed time*, the fields $\boldsymbol{\chi}$, $\mathbf{F}^e$ (and hence $\mathbf{F}$ and $\mathbf{F}^p$), and $\mathbf{N}^p$ are known, and consider the fields $\dot{\boldsymbol{\chi}}$, $\dot{\mathbf{F}}^e$, and $\dot{\bar{\epsilon}}^p$ as virtual velocities to be specified independently in a manner consistent with (2.34). That is, denoting the virtual fields by $\tilde{\boldsymbol{\chi}}, \tilde{\mathbf{F}}^e$, and $\tilde{\bar{\epsilon}}^p$ to differentiate them from fields associated with the actual evolution of the body, we require that

$$(\nabla\tilde{\boldsymbol{\chi}})\mathbf{F}^{-1}=\tilde{\mathbf{F}}^e\mathbf{F}^{e-1}+\sqrt{3/2}\tilde{\bar{\epsilon}}^p\mathbf{F}^e\mathbf{N}^p\mathbf{F}^{e-1}. \tag{2.36}$$

Further, also considering $\dot{\mathsf{e}}^p$ to be a virtual velocity, and denoting its virtual counterpart by $\tilde{\mathsf{e}}^p$, we define a generalized virtual velocity to be a list

$$\mathcal{V}=(\tilde{\boldsymbol{\chi}},\tilde{\mathbf{F}}^e,\tilde{\bar{\epsilon}}^p,\tilde{\mathsf{e}}^p), \tag{2.37}$$

consistent with (2.36). Writing

$$\left.\begin{aligned} \mathcal{W}_{\rm ext}({\rm P}) &= \int\limits_{\partial{\rm P}} \mathbf{t}_{\rm R}(\mathbf{n}_{\rm R})\cdot\tilde{\boldsymbol{\chi}}\,dA_{\rm R},+\int\limits_{\rm P}\mathbf{b}_{0\rm R}\cdot\tilde{\boldsymbol{\chi}}\,dV_{\rm R}+\int\limits_{\partial{\rm P}}\chi(\mathbf{n}_{\rm R})\tilde{\mathsf{e}}^p\,dA_{\rm R},\\ \mathcal{W}_{\rm int}({\rm P}) &= \int\limits_{\rm P}\Big(\mathbf{S}^e:\tilde{\mathbf{F}}^e+\pi\tilde{\bar{\epsilon}}^p+\mathsf{p}\tilde{\mathsf{e}}^p+\boldsymbol{\xi}\cdot\nabla\tilde{\mathsf{e}}^p\Big)\,dV_{\rm R}, \end{aligned}\right\} \tag{2.38}$$

respectively, for the external and internal expenditures of virtual power, the *principle of virtual power* is the requirement that the external and internal powers be balanced. That is, given any part P,

$$\mathcal{W}_{\text{ext}}(\mathrm{P},\mathcal{V}) = \mathcal{W}_{\text{int}}(\mathrm{P},\mathcal{V}) \quad \text{for all generalized virtual velocities} \quad \mathcal{V}. \tag{2.39}$$

2.5.2 Frame-indifference of the internal power and its consequences

We assume that the internal power $\mathcal{W}_{\text{int}}(\mathrm{P},\mathcal{V})$ is invariant under a change in frame, and that the virtual fields transform in a manner identical to their nonvirtual counterparts. Then given a change in frame, invariance of the internal power requires that

$$\mathcal{W}^*(\mathrm{P},\mathcal{V}^*) = \mathcal{W}(\mathrm{P},\mathcal{V}), \tag{2.40}$$

where $\mathcal{V}^*$ is the generalized virtual velocity in the new frame. In the new frame $\mathbf{S}^e$ transforms to $\mathbf{S}^{e*}$, $\boldsymbol{\xi}$ transforms to $\boldsymbol{\xi}^*$, and from (2.28) $\tilde{\mathbf{F}}^e$ transforms to

$$\tilde{\mathbf{F}}^{e*} = \mathbf{Q}\tilde{\mathbf{F}}^e + \dot{\mathbf{Q}}\mathbf{F}^e.$$

Further,

$$\pi,\ \tilde{\bar{\epsilon}}^p,\ \mathsf{p} \text{ and } \tilde{\mathsf{e}}^p \text{ are invariant,}$$

since they are scalar fields, and because "∇" represents a gradient in the reference body, the transformation rule for $\nabla\tilde{\mathsf{e}}^p$ is

$$(\nabla\tilde{\mathsf{e}}^p)^* = \nabla\tilde{\mathsf{e}}^p.$$

Thus, under a change in frame $\mathcal{W}_{\text{int}}(\mathrm{P},\mathcal{V})$ transforms to

$$\begin{aligned}
\mathcal{W}^*_{\text{int}}(\mathrm{P},\mathcal{V}^*) &= \int\limits_{\mathrm{P}} \Big\{\mathbf{S}^{e*}\colon\Big(\mathbf{Q}\tilde{\mathbf{F}}^e + \dot{\mathbf{Q}}\mathbf{F}^e\Big) + \pi\,\tilde{\bar{\epsilon}}^p + \mathsf{p}\tilde{\mathsf{e}}^p + \boldsymbol{\xi}^*\cdot\nabla\tilde{\mathsf{e}}^p\Big\}\,dV_{\mathrm{R}} \\
&= \int\limits_{\mathrm{P}} \Big\{\mathbf{Q}^{\top}\mathbf{S}^{e*}\colon\Big(\tilde{\mathbf{F}}^e + \mathbf{Q}^{\top}\dot{\mathbf{Q}}\mathbf{F}^e\Big) + \pi\,\tilde{\bar{\epsilon}}^p + \mathsf{p}\tilde{\mathsf{e}}^p + \boldsymbol{\xi}^*\cdot\nabla\tilde{\mathsf{e}}^p\Big\}\,dV_{\mathrm{R}}.
\end{aligned} \tag{2.41}$$

Then (2.40) implies that

$$\begin{aligned}
&\int\limits_{\mathrm{P}} \Big\{\mathbf{Q}^{\top}\mathbf{S}^{e*}\colon\Big(\tilde{\mathbf{F}}^e + \mathbf{Q}^{\top}\dot{\mathbf{Q}}\mathbf{F}^e\Big) + \pi\,\tilde{\bar{\epsilon}}^p + \mathsf{p}\tilde{\mathsf{e}}^p + \boldsymbol{\xi}^*\cdot\nabla\tilde{\mathsf{e}}^p\Big\}\,dV_{\mathrm{R}} \\
&= \int\limits_{\mathrm{P}} \Big(\mathbf{S}^e\colon\tilde{\mathbf{F}}^e + \pi\tilde{\bar{\epsilon}}^p + \mathsf{p}\tilde{\mathsf{e}}^p + \boldsymbol{\xi}\cdot\nabla\tilde{\mathsf{e}}^p\Big)\,dV_{\mathrm{R}},
\end{aligned} \tag{2.42}$$

or equivalently, since the part P is arbitrary,

$$\mathbf{Q}^{\top}\mathbf{S}^{e*}\colon\Big(\tilde{\mathbf{F}}^e + \mathbf{Q}^{\top}\dot{\mathbf{Q}}\mathbf{F}^e\Big) + \boldsymbol{\xi}^*\cdot\nabla\tilde{\mathsf{e}}^p = \mathbf{S}^e\colon\tilde{\mathbf{F}}^e + \boldsymbol{\xi}\cdot\nabla\tilde{\mathsf{e}}^p.$$

Also, since the change in frame is arbitrary, if we choose it such that $\mathbf{Q}$ is an arbitrary *time-independent* rotation, so that $\dot{\mathbf{Q}} = \mathbf{0}$, we find that

$$\Big(\mathbf{S}^e - (\mathbf{Q}^\top \mathbf{S}^{e*})\Big) : \tilde{\mathbf{F}}^e + \Big(\boldsymbol{\xi} - \boldsymbol{\xi}^*\Big) \cdot \nabla \tilde{e}^p = 0\,.$$

Since this must hold for all $\tilde{\mathbf{F}}^e$ and all $\nabla \tilde{e}^p$, we find that the stress $\mathbf{S}^e$ transforms according to

$$\mathbf{S}^{e*} = \mathbf{Q}\mathbf{S}^e, \tag{2.43}$$

and the microforce $\boldsymbol{\xi}$ is invariant

$$\boldsymbol{\xi}^* = \boldsymbol{\xi}. \tag{2.44}$$

Next, if we assume that $\mathbf{Q} = \mathbf{1}$ at the time in question, so that $\dot{\mathbf{Q}}$ is an arbitrary *skew* tensor, we find that

$$(\mathbf{S}^e \mathbf{F}^{e\top}) : \dot{\mathbf{Q}} = 0,$$

or that the stress $(\mathbf{S}^e \mathbf{F}^{e\top})$ is symmetric,

$$\mathbf{S}^e \mathbf{F}^{e\top} = \mathbf{F}^e \mathbf{S}^{e\top}\,. \tag{2.45}$$

Next, to deduce the consequences of the principle of virtual power, assume that (2.39) is satisfied. In applying the virtual balance (2.39) we are at liberty to choose any $\mathcal{V}$ consistent with the constraint (2.36).

2.5.3 Macroscopic force balance

Consider a generalized virtual velocity with both $\tilde{\bar{\epsilon}}^p \equiv 0$ and $\tilde{e}^p \equiv 0$, so that according to (2.36) $(\nabla \tilde{\boldsymbol{\chi}})\mathbf{F}^{p-1} = \tilde{\mathbf{F}}^e$. For this choice of $\mathcal{V}$, (2.39) and (2.38) yield

$$\int\limits_{\partial \mathrm{P}} \mathbf{t}_{\mathrm{R}}(\mathbf{n}_{\mathrm{R}}) \cdot \tilde{\boldsymbol{\chi}}\, dA_{\mathrm{R}} + \int\limits_{\mathrm{P}} \mathbf{b}_{0\mathrm{R}} \cdot \tilde{\boldsymbol{\chi}}\, dV_{\mathrm{R}} = \int\limits_{\mathrm{P}} \mathbf{S}^e : \tilde{\mathbf{F}}^e\, dV_{\mathrm{R}} = \int\limits_{\mathrm{P}} (\mathbf{S}^e \mathbf{F}^{p-\top}) : \nabla \tilde{\boldsymbol{\chi}}\, dV_{\mathrm{R}}, \tag{2.46}$$

which, by defining

$$\mathbf{T}_{\mathrm{R}} \overset{\text{def}}{=} \mathbf{S}^e \mathbf{F}^{p-\top}, \tag{2.47}$$

may be rewritten as

$$\int\limits_{\partial \mathrm{P}} \mathbf{t}_{\mathrm{R}}(\mathbf{n}_{\mathrm{R}}) \cdot \tilde{\boldsymbol{\chi}}\, dA_{\mathrm{R}} = \int\limits_{\mathrm{P}} \Big(\mathbf{T}_{\mathrm{R}} : \nabla \tilde{\boldsymbol{\chi}} - \mathbf{b}_{0\mathrm{R}} \cdot \tilde{\boldsymbol{\chi}}\Big)\, dV_{\mathrm{R}}, \tag{2.48}$$

and using the divergence theorem we may conclude that

$$\int\limits_{\partial \mathrm{P}} \Big(\mathbf{t}_{\mathrm{R}}(\mathbf{n}_{\mathrm{R}}) - \mathbf{T}_{\mathrm{R}} \mathbf{n}_{\mathrm{R}}\Big) \cdot \tilde{\boldsymbol{\chi}}\, dA_{\mathrm{R}} + \int\limits_{\mathrm{P}} \Big(\mathrm{Div}\, \mathbf{T}_{\mathrm{R}} + \mathbf{b}_{0\mathrm{R}}\Big) \cdot \tilde{\boldsymbol{\chi}}\, dV_{\mathrm{R}} = 0. \tag{2.49}$$

Since this relation must hold for all P and all $\tilde{\boldsymbol{\chi}}$, standard variational arguments yield the macroscopic traction condition

$$\boxed{\mathbf{t}_{\mathrm{R}}(\mathbf{n}_{\mathrm{R}}) = \mathbf{T}_{\mathrm{R}} \mathbf{n}_{\mathrm{R}},} \tag{2.50}$$

and the local macroscopic force balance

$$\boxed{\operatorname{Div}\mathbf{T}_{\mathrm{R}} + \mathbf{b}_{0\mathrm{R}} = \mathbf{0},} \tag{2.51}$$

respectively. Furthermore, (2.45) and (2.47) imply that

$$\boxed{\mathbf{T}_{\mathrm{R}}\mathbf{F}^{\top} = \mathbf{F}\mathbf{T}_{\mathrm{R}}^{\top}.} \tag{2.52}$$

Thus, $\mathbf{T}_{\mathrm{R}}$ represents the classical *Piola stress*, and (2.51) and (2.52) represent the local *macroscopic force and moment balances* in the reference body.

2.5.4 Microscopic force balances

To discuss the microscopic counterparts of macroscopic force balance, consider first a generalized virtual velocity with $\tilde{\boldsymbol{\chi}} \equiv \mathbf{0}$ and $\tilde{e}^p \equiv 0$, and choose the virtual field $\tilde{\bar{\epsilon}}^p$ arbitrarily. Then, (2.36) yields

$$\tilde{\mathbf{F}}^e = -\sqrt{3/2}\,\tilde{\bar{\epsilon}}^p\mathbf{F}^e\mathbf{N}^p \tag{2.53}$$

so that

$$\mathbf{S}^e : \tilde{\mathbf{F}}^e = -\tilde{\bar{\epsilon}}^p\Big(\sqrt{3/2}(\mathbf{F}^{e\top}\mathbf{S}^e) : \mathbf{N}^p)\Big). \tag{2.54}$$

Next, define a Mandel stress by

$$\mathbf{M}^e \overset{\text{def}}{=} \mathbf{F}^{e\top}\mathbf{S}^e, \tag{2.55}$$

and define an *equivalent tensile stress* $\bar{\sigma}$ by the relation

$$\bar{\sigma} = \sqrt{3/2}\mathbf{M}^e_0 : \mathbf{N}^p \tag{2.56}$$

where in writing the last relation we have used the fact that $\mathbf{N}^p$ is deviatoric. The power balance (2.39) along with (2.38) yields

$$0 = \int\limits_{\mathrm{P}} \Big(\mathbf{S}^e : \tilde{\mathbf{F}}^e + \pi\tilde{\bar{\epsilon}}^p\Big)\, dV_{\mathrm{R}} \tag{2.57}$$

which using (2.54), (2.55), and (2.56) may be rewritten as

$$0 = \int\limits_{\mathrm{P}} \Big(\pi - \bar{\sigma}\Big)\tilde{\bar{\epsilon}}^p\, dV_{\mathrm{R}} \tag{2.58}$$

which must be satisfied for all $\tilde{\bar{\epsilon}}^p$ and all P. This yields the first microscopic force balance

$$\boxed{\bar{\sigma} = \pi.} \tag{2.59}$$

Next, consider a generalized virtual velocity with $\tilde{\boldsymbol{\chi}} \equiv \mathbf{0}$ and $\tilde{\bar{\epsilon}}^p \equiv 0$, and choose the virtual field $\tilde{e}^p$ arbitrarily. The power balance (2.39) along with (2.38) yields the second microscopic virtual-power relation

$$\int_{\partial \mathrm{P}} \chi(\mathbf{n}_{\mathrm{R}})\tilde{e}^p \, dA_{\mathrm{R}} = \int_{\mathrm{P}} \left(p\tilde{e}^p + \boldsymbol{\xi} \cdot \nabla\tilde{e}^p\right) dV_{\mathrm{R}} \tag{2.60}$$

to be satisfied for all $\tilde{e}^p$ and all P. Equivalently, using the divergence theorem,

$$\int_{\partial \mathrm{P}} \left(\chi(\mathbf{n}_{\mathrm{R}}) - \boldsymbol{\xi} \cdot \mathbf{n}_{\mathrm{R}}\right)\tilde{e}^p \, dA_{\mathrm{R}} + \int_{\mathrm{P}} \left(\mathrm{Div}\boldsymbol{\xi} - p\right)\tilde{e}^p \, dV_{\mathrm{R}} = 0, \tag{2.61}$$

and a standard argument yields the microscopic traction condition

$$\boxed{\chi(\mathbf{n}_{\mathrm{R}}) = \boldsymbol{\xi} \cdot \mathbf{n}_{\mathrm{R}},} \tag{2.62}$$

and the second microscopic force balance

$$\boxed{\mathrm{Div}\boldsymbol{\xi} - p = 0.} \tag{2.63}$$

2.6 Balance law for the diffusion of hydrogen

Following Anand (2011), let C(**X**,t) denote the *total number of moles of hydrogen atoms per unit reference volume.* Hydrogen is absorbed into the metal into *normal interstitial lattice sites* (NILS), and into *trapping sites* associated with internal microstructural defects such as dislocation cores, grain boundaries, and interfaces of second-phase particles with the matrix material. Accordingly, we assume that $C(\mathbf{X},t)$ is additively decomposable as

$$C(\mathbf{X},t) = C_L(\mathbf{X},t) + \sum_{\alpha} C_{\alpha}(\mathbf{X},t) \tag{2.64}$$

where $C_L(\mathbf{X},t)$ denotes the number of moles of hydrogen atoms in normal interstitial lattice sites per unit reference volume, $C_{\alpha}(\mathbf{X},t)$ represents the number of moles of hydrogen atoms in trapping sites per unit reference volume, and α denotes the specific type of trap site in which the hydrogen resides. For brevity we henceforth refer to hydrogen residing in NILS as *lattice hydrogen* and to hydrogen residing in trapping sites as *trapped hydrogen.*

For convenience in mathematical modeling of the notion of trapping of a portion of hydrogen content in the material at microstructural trapping sites we consider C_L and C_{α} as *different species of solutes.* Changes in C_L and C_{α} in a part P are then brought about by diffusion of the species across its boundary ∂P and by the transformation between latticed and trapped hydrogen.

As is standard, the rate of change of lattice and trapped hydrogen in P is given by

$$\left.\begin{aligned} \dot{C}_L &= -\mathrm{Div}\mathbf{j}_L - \sum_{\alpha} h_{\mathrm{L}\to\alpha}, \\ \dot{C}_{\alpha} &= -\mathrm{Div}\mathbf{j}_{\alpha} + h_{\mathrm{L}\to\alpha}, \quad \forall\, \alpha, \end{aligned}\right\} \tag{2.65}$$

where $\mathbf{j}_L(\mathbf{X},t)$ and $\mathbf{j}_{\alpha}(\mathbf{X},t)$ are the *fluxes* of lattice and trapped hydrogen measured as the number of moles of solute atoms per unit area per unit time, and $h_{\mathrm{L}\to\alpha}$ is the transformation rate from lattice to trapped hydrogen measured as the number of moles of solute atoms per unit volume per unit time. At this point in the development of the theory it is convenient to allow for non-zero fluxes $\mathbf{j}_\alpha$ for the trapped hydrogen; later, we shall make specific assumptions which will result in $\mathbf{j}_\alpha = \mathbf{0}$.

2.7 Balance of energy. Entropy imbalance. Free-energy imbalance

Our discussion of thermodynamics follows Gurtin et al. (2010, Section 64), and involves the following fields

ε_{R}	the internal energy density per unit reference volume,
η_{R}	the entropy density per unit reference volume,
$\mathbf{q}_{\mathrm{R}}$	the heat flux per unit reference area,
q_{R}	the external heat supply per unit reference volume,
$\vartheta > 0$	the absolute temperature,
μ_L	the chemical potential for the lattice hydrogen,
μ_α	the chemical potential for the α-th trapped hydrogen species.

The balance law for energy, is

$$\dot{\overline{\int_{\mathrm{P}} \varepsilon_{\mathrm{R}}\, dV_{\mathrm{R}}}} = -\int_{\partial\mathrm{P}} \mathbf{q}_{\mathrm{R}}\cdot\mathbf{n}_{\mathrm{R}}\, dA_{\mathrm{R}} + \int_{\mathrm{P}} q_{\mathrm{R}}\, dV_{\mathrm{R}} + \mathcal{W}_{\mathrm{ext}}(\mathrm{P}) - \int_{\partial\mathrm{P}} \mu_L \mathbf{j}_L\cdot\mathbf{n}_{\mathrm{R}}\, dA_{\mathrm{R}} - \sum_\alpha \int_{\partial\mathrm{P}} \mu_\alpha \mathbf{j}_\alpha\cdot\mathbf{n}_{\mathrm{R}}\, dA_{\mathrm{R}}, \tag{2.66}$$

where the last two terms in (2.66) represents the energy contribution into P by the lattice and trapped hydrogen (Gurtin, 1996). Since $\mathcal{W}_{\mathrm{ext}}(\mathrm{P}) = \mathcal{W}_{\mathrm{int}}(\mathrm{P})$, using $(2.35)_2$, and applying the divergence theorem, we obtain

$$\begin{aligned}\int_{\mathrm{P}} \dot\varepsilon_{\mathrm{R}}\, dV_{\mathrm{R}} = \int_{\mathrm{P}} \Big(&\mathbf{S}^e : \dot{\mathbf{F}}^e + \pi\dot{\bar{e}}^p + p\dot{e}^p + \boldsymbol{\xi}\cdot\nabla\dot{e}^p - \mathrm{Div}\,\mathbf{q}_{\mathrm{R}} + q_{\mathrm{R}} \\ &- \mu_L \mathrm{Div}\mathbf{j}_L - \mathbf{j}_L\cdot\nabla\mu_L + \sum_\alpha \Big(- \mu_\alpha \mathrm{Div}\mathbf{j}_\alpha - \mathbf{j}_\alpha\cdot\nabla\mu_\alpha\Big)\Big)\, dV_{\mathrm{R}}.\end{aligned} \tag{2.67}$$

Use of the balance laws (2.65) and the fact that (2.67) must hold for all parts P, gives the local form of the energy balance as

$$\begin{aligned}\dot\varepsilon_{\mathrm{R}} &= \mathbf{S}^e : \dot{\mathbf{F}}^e + \pi\dot{\bar{e}}^p + p\dot{e}^p + \boldsymbol{\xi}\cdot\nabla\dot{e}^p - \mathrm{Div}\,\mathbf{q}_{\mathrm{R}} + q_{\mathrm{R}} \\ &\quad + \mu_L \dot{C}_L - \mathbf{j}_L\cdot\nabla\mu_L + \sum_\alpha \Big(\mu_\alpha \dot{C}_\alpha - \mathbf{j}_\alpha\cdot\nabla\mu_\alpha + (\mu_L - \mu_\alpha) h_{\mathrm{L}\to\alpha}\Big).\end{aligned} \tag{2.68}$$

Note that while the "elastic power" $\mathbf{S}^e : \dot{\mathbf{F}}^e$ itself is invariant, neither the stress $\mathbf{S}^e$ nor the elastic distortion rate $\dot{\mathbf{F}}^e$ are invariant under a change in frame. Accordingly, as is standard, we express this elastic power in terms of $\dot{\mathbf{C}}^e$ and a power-conjugate stress measure. Let

$$\mathbf{T}^e \overset{\mathrm{def}}{=} \mathbf{F}^{e-1}\mathbf{S}^e \tag{2.69}$$

then, since $\mathbf{S}^e\mathbf{F}^{e\top} = \mathbf{F}^e\mathbf{T}^e\mathbf{F}^{e\top}$, (2.45) yields

$$\mathbf{T}^e = \mathbf{T}^{e\top}. \tag{2.70}$$

Thus $\mathbf{S}^e : \dot{\mathbf{F}}^e = \mathbf{T}^e : \mathbf{F}^{e\top}\dot{\mathbf{F}}^e$, and in view of (2.12),

$$\mathbf{S}^e : \dot{\mathbf{F}}^e = \frac{1}{2}\mathbf{T}^e : \dot{\mathbf{C}}^e. \tag{2.71}$$

Finally, using this result the local energy energy balance (2.68) may be rewritten as

$$\begin{aligned} \dot{\varepsilon}_{\mathrm{R}} = {} & \frac{1}{2}\mathbf{T}^e : \dot{\mathbf{C}}^e + \pi\dot{\bar{\epsilon}}^p + p\dot{e}^p + \boldsymbol{\xi}\cdot\nabla\dot{e}^p - \mathrm{Div}\,\mathbf{q}_{\mathrm{R}} + q_{\mathrm{R}} \\ & + \mu_L\dot{C}_L - \mathbf{j}_L\cdot\nabla\mu_L + \sum_\alpha\Big(\mu_\alpha\dot{C}_\alpha - \mathbf{j}_\alpha\cdot\nabla\mu_\alpha + (\mu_L-\mu_\alpha)h_{\mathrm{L}\to\alpha}\Big). \end{aligned} \tag{2.72}$$

The second law takes the form of an entropy imbalance

$$\overline{\int_{\mathrm{P}} \eta_{\mathrm{R}}\, dV_{\mathrm{R}}}^{\boldsymbol{\cdot}} \ge -\int_{\partial\mathrm{P}} \frac{\mathbf{q}_{\mathrm{R}}\cdot\mathbf{n}_{\mathrm{R}}}{\vartheta}\, dA_{\mathrm{R}} + \int_{\mathrm{P}} \frac{q_{\mathrm{R}}}{\vartheta}\, dV_{\mathrm{R}} \tag{2.73}$$

and the local entropy imbalance has the form of

$$\dot{\eta}_{\mathrm{R}} \ge -\mathrm{Div}\left(\frac{\mathbf{q}_{\mathrm{R}}}{\vartheta}\right) + \frac{q_{\mathrm{R}}}{\vartheta} \tag{2.74}$$

Let

$$\psi_{\mathrm{R}} \overset{\mathrm{def}}{=} \varepsilon_{\mathrm{R}} - \vartheta\eta_{\mathrm{R}} \tag{2.75}$$

denote the (Hemholtz) free energy per unit volume of the reference body. Then use of (2.72), (2.74) and (2.75) yields the local free-energy imbalance

$$\begin{aligned} & \dot{\psi}_{\mathrm{R}} + \eta_{\mathrm{R}}\dot{\vartheta} - \frac{1}{2}\mathbf{T}^e : \dot{\mathbf{C}}^e - \pi\dot{\bar{\epsilon}}^p - p\dot{e}^p - \boldsymbol{\xi}\cdot\nabla\dot{e}^p + \frac{1}{\vartheta}\mathbf{q}_{\mathrm{R}}\cdot\nabla\vartheta \\ & - \mu_L\dot{C}_L + \mathbf{j}_L\cdot\nabla\mu_L + \sum_\alpha\Big(- \mu_\alpha\dot{C}_\alpha + \mathbf{j}_\alpha\cdot\nabla\mu_\alpha - (\mu_L-\mu_\alpha)h_{\mathrm{L}\to\alpha}\Big) \le 0. \end{aligned} \tag{2.76}$$

We use this inequality as a guide in developing a suitable constitutive theory.

For later use we define the dissipation density $\mathcal{D} \ge 0$ per unit volume per unit time by

$$\begin{aligned} \mathcal{D} = {} & \frac{1}{2}\mathbf{T}^e : \dot{\mathbf{C}}^e + \pi\dot{\bar{\epsilon}}^p + p\dot{e}^p + \boldsymbol{\xi}\cdot\nabla\dot{e}^p - \frac{1}{\vartheta}\mathbf{q}_{\mathrm{R}}\cdot\nabla\vartheta \\ & + \mu_L\dot{C}_L - \mathbf{j}_L\cdot\nabla\mu_L + \sum_\alpha\Big(\mu_\alpha\dot{C}_\alpha - \mathbf{j}_\alpha\cdot\nabla\mu_\alpha + (\mu_L-\mu_\alpha)h_{\mathrm{L}\to\alpha}\Big) - \dot{\psi}_{\mathrm{R}} - \eta_{\mathrm{R}}\dot{\vartheta} \ge 0. \end{aligned} \tag{2.77}$$

In the preceding discussion we have introduced four stress measures: $\mathbf{S}^e$, $\mathbf{T}_{\mathrm{R}}$, $\mathbf{M}^e$, and $\mathbf{T}^e$. Before closing this section we note that since the Piola stress $\mathbf{T}_{\mathrm{R}}$ is related to the symmetric Cauchy stress $\mathbf{T}$ in the deformed body by the standard relation

$$\mathbf{T}_{\mathrm{R}} = J\mathbf{T}\mathbf{F}^{-\top} \tag{2.78}$$

the definitions (2.47), (2.69), and (2.55) yield the following relations between the stress-measures $\mathbf{S}^e$, $\mathbf{T}^e$, $\mathbf{M}^e$, and the Cauchy stress $\mathbf{T}$:

$$\mathbf{S}^e = J\mathbf{T}\mathbf{F}^{e-\top}, \qquad \mathbf{T}^e = J\mathbf{F}^{e-1}\mathbf{T}\mathbf{F}^{e-\top}, \qquad \text{and} \qquad \mathbf{M}^e = J\mathbf{F}^{e\top}\mathbf{T}\mathbf{F}^{e-\top} = \mathbf{C}^e\mathbf{T}^e. \tag{2.79}$$

2.8 Constitutive theory

2.8.1 Basic constitutive equations

Guided by the free-energy imbalance (2.76), we first consider the following constitutive equations for the free energy ψ_R, the stress $\mathbf{T}^e$, the entropy η_R, the chemical potentials μ_L and μ_α, the scalar microscopic stress π, the scalar microscopic stress p, and the vector microscopic stress $\boldsymbol{\xi}$:

$$\left.\begin{aligned}
\psi_\mathrm{R} &= \hat{\psi}_\mathrm{R}(\Lambda),\\
\mathbf{T}^e &= \hat{\mathbf{T}}^e(\Lambda),\\
\eta_\mathrm{R} &= \hat{\eta}_\mathrm{R}(\Lambda),\\
\mu_L &= \hat{\mu}_L(\Lambda),\\
\mu_\alpha &= \hat{\mu}_\alpha(\Lambda),\\
\pi &= \hat{\pi}(\Lambda),\\
\mathsf{p} &= \hat{\mathsf{p}}(\Lambda),\\
\boldsymbol{\xi} &= \hat{\boldsymbol{\xi}}(\Lambda),
\end{aligned}\right\} \tag{2.80}$$

where Λ denotes the list

$$\Lambda = (\mathbf{C}^e, \bar{e}^p, e^p, \nabla e^p, \vartheta, C_L, C_\alpha). \tag{2.81}$$

Further, we assume that the scalar and vector microscopic stresses π, p, and $\boldsymbol{\xi}$ can be decomposed into energetic and dissipative parts

$$\left.\begin{aligned}
\pi &= \pi_\mathrm{en} + \pi_\mathrm{dis},\\
\mathsf{p} &= \mathsf{p}_\mathrm{en} + \mathsf{p}_\mathrm{dis},\\
\boldsymbol{\xi} &= \boldsymbol{\xi}_\mathrm{en} + \boldsymbol{\xi}_\mathrm{dis}.
\end{aligned}\right\} \tag{2.82}$$

2.8.2 Thermodynamic restrictions

Using $(2.80)_1$ the local free-energy imbalance (2.76) may be rewritten as

$$\begin{aligned}&\left(\frac{\partial\hat{\psi}_{\mathrm{R}}(\Lambda)}{\partial\vartheta}+\eta_{\mathrm{R}}\right)\dot{\vartheta}+\left(\frac{\partial\hat{\psi}_{\mathrm{R}}(\Lambda)}{\partial\mathbf{C}^e}-\frac{1}{2}\mathbf{T}^e\right):\dot{\mathbf{C}}^e+\left(\frac{\partial\hat{\psi}_{\mathrm{R}}(\Lambda)}{\partial\bar{\epsilon}^p}-\pi\right)\dot{\bar{\epsilon}}^p\\&+\left(\frac{\partial\hat{\psi}_{\mathrm{R}}(\Lambda)}{\partial e^p}-\mathsf{p}\right)\dot{e}^p+\left(\frac{\partial\hat{\psi}_{\mathrm{R}}(\Lambda)}{\partial\nabla e^p}-\boldsymbol{\xi}\right)\cdot\nabla\dot{e}^p+\left(\frac{\partial\hat{\psi}_{\mathrm{R}}(\Lambda)}{\partial C_L}-\mu_L\right)\dot{C}_L\\&+\sum_\alpha\left(\frac{\partial\hat{\psi}_{\mathrm{R}}(\Lambda)}{\partial C_\alpha}-\mu_\alpha\right)\dot{C}_\alpha+\mathbf{j}_L\cdot\nabla\mu_L+\sum_\alpha\Big(\mathbf{j}_\alpha\cdot\nabla\mu_\alpha-(\mu_L-\mu_\alpha)h_{\mathrm{L}\to\alpha}\Big)+\frac{1}{\vartheta}\mathbf{q}_{\mathrm{R}}\cdot\nabla\vartheta\leq 0.\end{aligned}\tag{2.83}$$

We identify the energetic components of π, p and $\boldsymbol{\xi}$ as

$$\left.\begin{aligned}\pi_{\mathrm{en}}&\overset{\mathrm{def}}{=}\frac{\partial\hat{\psi}_{\mathrm{R}}(\Lambda)}{\partial\bar{\epsilon}^p},\\\mathsf{p}_{\mathrm{en}}&\overset{\mathrm{def}}{=}\frac{\partial\hat{\psi}_{\mathrm{R}}(\Lambda)}{\partial e^p},\\\boldsymbol{\xi}_{\mathrm{en}}&\overset{\mathrm{def}}{=}\frac{\partial\hat{\psi}_{\mathrm{R}}(\Lambda)}{\partial\nabla e^p},\end{aligned}\right\}\tag{2.84}$$

such that using (2.82) and (2.84) in (2.83) the local free-energy imbalance may be written as

$$\begin{aligned}&\left(\frac{\partial\hat{\psi}_{\mathrm{R}}(\Lambda)}{\partial\vartheta}+\eta_{\mathrm{R}}\right)\dot{\vartheta}+\left(\frac{\partial\hat{\psi}_{\mathrm{R}}(\Lambda)}{\partial\mathbf{C}^e}-\frac{1}{2}\mathbf{T}^e\right):\dot{\mathbf{C}}^e+\left(\frac{\partial\hat{\psi}_{\mathrm{R}}(\Lambda)}{\partial C_L}-\mu_L\right)\dot{C}_L\\&+\sum_\alpha\left(\frac{\partial\hat{\psi}_{\mathrm{R}}(\Lambda)}{\partial C_\alpha}-\mu_\alpha\right)\dot{C}_\alpha-\pi_{\mathrm{dis}}\dot{\bar{\epsilon}}^p-\mathsf{p}_{\mathrm{dis}}\dot{e}^p-\boldsymbol{\xi}_{\mathrm{dis}}\cdot\nabla\dot{e}^p\\&+\mathbf{j}_L\cdot\nabla\mu_L+\sum_\alpha\Big(\mathbf{j}_\alpha\cdot\nabla\mu_\alpha-(\mu_L-\mu_\alpha)h_{\mathrm{L}\to\alpha}\Big)+\frac{1}{\vartheta}\mathbf{q}_{\mathrm{R}}\cdot\nabla\vartheta\leq 0.\end{aligned}\tag{2.85}$$

This inequality must hold for all values of Λ. Since $\dot{\vartheta}$, $\dot{\mathbf{C}}^e$, $\dot{C}_L$, and $\dot{C}_\alpha$ appear linearly, their "coefficients" must vanish, for otherwise $\dot{\vartheta}$, $\dot{\mathbf{C}}^e$, $\dot{C}_L$, and $\dot{C}_\alpha$ may be chosen to violate (2.85). We are therefore led to the thermodynamic restriction that the free energy determines the stress $\mathbf{T}^e$, the entropy $\eta_{\rm R}$, and the chemical potentials μ_L and μ_α through the "state relations"

$$\left.\begin{aligned} \mathbf{T}^e &= 2\frac{\partial\hat\psi_{\rm R}(\Lambda)}{\partial\mathbf{C}^e}, \\ \eta_{\rm R} &= -\frac{\partial\hat\psi_{\rm R}(\Lambda)}{\partial\vartheta}, \\ \mu_L &= \frac{\partial\hat\psi_{\rm R}(\Lambda)}{\partial C_L}, \\ \mu_\alpha &= \frac{\partial\hat\psi_{\rm R}(\Lambda)}{\partial C_\alpha}, \end{aligned}\right\} \tag{2.86}$$

and the dissipation density (2.77) reduces to

$$\mathcal{D} = \pi_{\rm dis}\dot{\bar\epsilon}^p + p_{\rm dis}\dot e^p + \boldsymbol{\xi}_{\rm dis}\cdot\nabla\dot e^p - \mathbf{j}_L\cdot\nabla\mu_L + \sum_\alpha\Big(-\mathbf{j}_\alpha\cdot\nabla\mu_\alpha + (\mu_L-\mu_\alpha)h_{\rm L\to\alpha}\Big) - \frac{1}{\vartheta}\mathbf{q}_{\rm R}\cdot\nabla\vartheta \geq 0. \tag{2.87}$$

2.8.3 Dissipative constitutive equations

Next, guided by the dissipation inequality (2.87), and experience with existing plasticity theories, we make the following constitutive assumptions:

(1) As is classical in finite deformation theories of isotropic plasticity (cf., Gurtin et al., 2010), we assume that the direction of the plastic flow coincides with the direction of the deviatoric Mandel stress, that is $\mathbf{D}^p$ is *codirectional* with $\mathbf{M}_0^e$. The plastic flow direction (2.19) is then given by

$$\mathbf{N}^p = \frac{\mathbf{D}^p}{|\mathbf{D}^p|} \equiv \frac{\mathbf{M}_0^e}{|\mathbf{M}_0^e|}. \tag{2.88}$$

Thus, the equivalent tensile stress $\bar\sigma = \sqrt{3/2}\,\mathbf{M}_0^e\!:\!\mathbf{N}^p$, defined in (2.56), is given by

$$\bar\sigma = \sqrt{3/2}|\mathbf{M}_0^e|. \tag{2.89}$$

Using (2.20), (2.88), and (2.89) the plastic stretching $\mathbf{D}^p$ may be written as

$$\mathbf{D}^p = \frac{3}{2}\dot{\bar\epsilon}^p\frac{\mathbf{M}_0^e}{\bar\sigma}. \tag{2.90}$$

(2) A constitutive equation for $\pi_{\rm dis}$ of the form

$$\pi_{\rm dis} = \hat Y_{\rm dis}(\hat\Lambda) \quad \text{with} \quad \hat\Lambda = (\bar\epsilon^p, e^p, \vartheta, C_L, C_\alpha), \tag{2.91}$$

which for simplicity is independent of $\dot{\bar\epsilon}^p$ and $\dot e^p$. Here

$$Y_{\rm dis} > 0, \tag{2.92}$$

a positive-valued scalar with dimensions of stress, represents the classical flow resistance of the material. The initial value at a reference temperature ϑ_0 and at reference concentrations

C_L^0 and C_α^0,

$$Y_0 \overset{\text{def}}{=} \hat{Y}_{\text{dis}}(0, 0, \vartheta_0, C_L^0, C_\alpha^0) > 0, \tag{2.93}$$

represents the inial yield strength. Let

$$\hat{Y}(\hat{\Lambda}) \overset{\text{def}}{=} \hat{Y}_{\text{dis}}(\hat{\Lambda}) + \hat{Y}_{\text{en}}(\hat{\Lambda}) \quad \text{with} \quad Y_{\text{en}} \overset{\text{def}}{=} \pi_{\text{en}} \tag{2.94}$$

represent the combined dissipative and energetic parts of the constitutive equation for π. Then the microscopic force balance (2.59) requires that

$$\bar{\sigma} = Y \quad \text{when} \quad \dot{\bar{\epsilon}}^p > 0. \tag{2.95}$$

(3) Based on (2.95) we introduce a yield function

$$f \overset{\text{def}}{=} \bar{\sigma} - \hat{Y}(\hat{\Lambda}) \leq 0, \tag{2.96}$$

which limits the admissible deviatoric stresses $\mathbf{M}_0^e$. Then, as is standard, a rate-independent theory is based on the Kuhn-Tucker conditions

$$\dot{\bar{\epsilon}}^p \geq 0, \quad f \leq 0, \quad \text{and} \quad \dot{\bar{\epsilon}}^p f = 0, \tag{2.97}$$

together with the consistency condition

$$\dot{\bar{\epsilon}}^p \dot{f} = 0 \quad \text{when} \quad f = 0. \tag{2.98}$$

(4) We assume further that the dissipative microscopic stresses p_{dis} and $\boldsymbol{\xi}_{\text{dis}}$ are given by constitutive equations

$$\begin{aligned} p_{\text{dis}} &= \hat{p}_{\text{dis}}(\bar{\epsilon}^p, \dot{\bar{\epsilon}}^p, e^p, \dot{e}^p, \nabla e^p, \nabla \dot{e}^p, \vartheta, C_L, C_\alpha), \\ \boldsymbol{\xi}_{\text{dis}} &= \hat{\boldsymbol{\xi}}_{\text{dis}}(\bar{\epsilon}^p, \dot{\bar{\epsilon}}^p, e^p, \dot{e}^p, \nabla e^p, \nabla \dot{e}^p, \vartheta, C_L, C_\alpha). \end{aligned} \tag{2.99}$$

5) We assume that the transformation rates $h_{\text{L}\to\alpha}$ depend on the equivalent tensile plastic strain $\bar{\epsilon}^p$, the temperature ϑ, and the concentrations C_L and C_α

$$h_{\text{L}\to\alpha} = \hat{h}_{\text{L}\to\alpha}(\bar{\epsilon}^p, \vartheta, C_L, C_\alpha), \quad \forall\, \alpha. \tag{2.100}$$

More generally, as discussed in Appendix A, the transformation rates $h_{\text{L}\to\alpha}$ may depend on the conjugate driving force $(\mu_L - \mu_\alpha)$; cf. eq. (2.87).

To the constitutive equations above we append a Fourier-type relation for the heat flux, and Fick-type relations for the flux of the diffusing hydrogen,[4]

$$\left.\begin{aligned} \mathbf{q}_{\mathrm{R}} &= -\hat{\mathbf{K}}(\tilde{\Lambda})\nabla\vartheta, \\ \mathbf{j}_L &= -\hat{\mathbf{M}}_L(\tilde{\Lambda})\nabla\mu_L, \\ \mathbf{j}_\alpha &= -\hat{\mathbf{M}}_\alpha(\tilde{\Lambda})\nabla\mu_\alpha, \end{aligned}\right\} \tag{2.101}$$

where $\mathbf{K}$ is a thermal conductivity tensor, $\mathbf{M}_L$ and $\mathbf{M}_\alpha$ are mobility tensors, and $\tilde{\Lambda}$ denotes the list

$$\tilde{\Lambda} = (\mathbf{C}^e, \bar{\epsilon}^p, \vartheta, C_L, C_\alpha). \tag{2.102}$$

Finally, the dissipation density (2.87) may be written as

$$\begin{aligned} \mathcal{D} = \pi_{\mathrm{dis}}\dot{\bar{\epsilon}}^p + p_{\mathrm{dis}}\dot{\mathsf{e}}^p + \boldsymbol{\xi}_{\mathrm{dis}} \cdot \nabla\dot{\mathsf{e}}^p + \frac{1}{\vartheta}\nabla\vartheta \cdot \mathbf{K}\nabla\vartheta \\ + \nabla\mu_L \cdot \mathbf{M}_L\nabla\mu_L + \sum_\alpha \Big(\nabla\mu_\alpha \cdot \mathbf{M}_\alpha\nabla\mu_\alpha + (\mu_L - \mu_\alpha)h_{\mathrm{L}\to\alpha}\Big) \geq 0. \end{aligned} \tag{2.103}$$

We also assume that the terms in (2.103) individually satisfy

$$\pi_{\mathrm{dis}}\dot{\bar{\epsilon}}^p > 0 \quad \text{for} \quad \dot{\bar{\epsilon}}^p > 0, \tag{2.104}$$

$$p_{\mathrm{dis}}\dot{\mathsf{e}}^p > 0 \quad \text{for} \quad \dot{\mathsf{e}}^p > 0, \tag{2.105}$$

$$\boldsymbol{\xi}_{\mathrm{dis}} \cdot \nabla\dot{\mathsf{e}}^p > 0 \quad \text{for} \quad \nabla\dot{\bar{\epsilon}}^p \neq \mathbf{0}, \tag{2.106}$$

and

$$\nabla\vartheta \cdot \mathbf{K}\nabla\vartheta \geq 0, \tag{2.107}$$

$$\nabla\mu_L \cdot \mathbf{M}_L\nabla\mu_L \geq 0, \tag{2.108}$$

$$(\mu_L - \mu_\alpha)h_{\mathrm{L}\to\alpha} \geq 0, \quad \forall\,\alpha, \tag{2.109}$$

$$\nabla\mu_\alpha \cdot \mathbf{M}_\alpha\nabla\mu_\alpha \geq 0, \quad \forall\,\alpha. \tag{2.110}$$

Thus, note that the thermal conductivity tensor $\mathbf{K}$ and the mobility tensors $\mathbf{M}_L$ and $\mathbf{M}_\alpha$ are positive-semidefinite.

2.8.4 Further consequences of thermodynamics

In view of $(2.80)_1$, (2.84), and (2.86) we have the first Gibbs relation,

$$\dot{\psi}_{\mathrm{R}} = \frac{1}{2}\mathbf{T}^e : \dot{\mathbf{C}}^e + \pi_{\mathrm{en}}\dot{\bar{\epsilon}}^p + p_{\mathrm{en}}\dot{\mathsf{e}}^p + \boldsymbol{\xi}_{\mathrm{en}} \cdot \nabla\dot{\mathsf{e}}^p - \eta\dot{\vartheta} + \mu_L\dot{C}_L + \sum_\alpha \mu_\alpha\dot{C}_\alpha, \tag{2.111}$$

---

[4] We neglect Soret-type coupling effects in which $\mathbf{j}_L$ or $\mathbf{j}_\alpha$ are affected by $\nabla\vartheta$, and $\mathbf{q}_{\mathrm{R}}$ by $\nabla\mu_L$ and $\nabla\mu_\alpha$.

which, with (2.75), yields the second Gibbs relation

$$\dot{\varepsilon}_{\mathrm{R}} = \vartheta\dot{\eta}_{\mathrm{R}} + \frac{1}{2}\mathbf{T}^e : \dot{\mathbf{C}}^e + \pi_{\mathrm{en}}\dot{\bar{\epsilon}}^p + \mathsf{p}_{\mathrm{en}}\,\dot{\mathsf{e}}^p + \boldsymbol{\xi}_{\mathrm{en}} \cdot \nabla\dot{\mathsf{e}}^p + \mu_L\dot{C}_L + \sum_{\alpha}\mu_\alpha\dot{C}_\alpha. \tag{2.112}$$

Using the balance of energy (2.72), the second Gibbs relation (2.112), the decomposition of the scalar and vector microscopic stresses (2.82), and equations (2.101), we arrive at the entropy balance

$$\begin{aligned}\vartheta\dot{\eta}_{\mathrm{R}} = {} & -\mathrm{Div}\,\mathbf{q}_{\mathrm{R}} + q_{\mathrm{R}} + \pi_{\mathrm{dis}}\dot{\bar{\epsilon}}^p + \mathsf{p}_{\mathrm{dis}}\,\dot{\mathsf{e}}^p + \boldsymbol{\xi}_{\mathrm{dis}} \cdot \nabla\dot{\mathsf{e}}^p \\ & + \nabla\mu_L \cdot \mathbf{M}_L\nabla\mu_L + \sum_{\alpha}\Big(\nabla\mu_\alpha \cdot \mathbf{M}_\alpha\nabla\mu_\alpha + (\mu_L - \mu_\alpha)h_{\mathrm{L}\to\alpha}\Big).\end{aligned} \tag{2.113}$$

Granted the thermodynamically-restricted constitutive relations (2.84) and (2.86), along with the decomposition (2.82), this balance is equivalent to the balance of energy.

Next, from (2.75), the internal energy density is given by

$$\hat{\varepsilon}_{\mathrm{R}}(\Lambda) = \hat{\psi}_{\mathrm{R}}(\Lambda) + \vartheta\hat{\eta}_{\mathrm{R}}(\Lambda) \tag{2.114}$$

and, as is standard, the specific heat is defined by

$$c \overset{\mathrm{def}}{=} \frac{\partial\hat{\varepsilon}_{\mathrm{R}}(\Lambda)}{\partial\vartheta}. \tag{2.115}$$

Hence, from (2.114)

$$c = \left(\frac{\partial\hat{\psi}_{\mathrm{R}}(\Lambda)}{\partial\vartheta} + \hat{\eta}_{\mathrm{R}}(\Lambda) + \vartheta\frac{\partial\hat{\eta}_{\mathrm{R}}(\Lambda)}{\partial\vartheta}\right), \tag{2.116}$$

and use of (2.86) gives

$$c = -\vartheta\frac{\partial^2\hat{\psi}_{\mathrm{R}}(\Lambda)}{\partial\vartheta^2}. \tag{2.117}$$

Next, using $(2.80)_3$ and (2.117)

$$\begin{aligned}\vartheta\dot{\eta}_{\mathrm{R}} = {} & -\vartheta\frac{\partial^2\hat{\psi}(\Lambda)}{\partial\vartheta\partial\mathbf{C}^e} : \dot{\mathbf{C}}^e - \vartheta\frac{\partial^2\hat{\psi}(\Lambda)}{\partial\vartheta\partial\bar{\epsilon}^p}\dot{\bar{\epsilon}}^p - \vartheta\frac{\partial^2\hat{\psi}(\Lambda)}{\partial\vartheta\partial\mathsf{e}^p}\dot{\mathsf{e}}^p - \vartheta\frac{\partial^2\hat{\psi}(\Lambda)}{\partial\vartheta\partial\nabla\mathsf{e}^p} \cdot \nabla\dot{\mathsf{e}}^p + c\dot{\vartheta} \\ & - \vartheta\frac{\partial^2\hat{\psi}(\Lambda)}{\partial\vartheta\partial C_L}\dot{C}_L - \sum_{\alpha}\vartheta\frac{\partial^2\hat{\psi}(\Lambda)}{\partial\vartheta\partial C_\alpha}\dot{C}_\alpha,\end{aligned} \tag{2.118}$$

which using (2.84) and (2.86) yields

$$\vartheta\dot{\eta}_{\mathrm{R}} = -\frac{1}{2}\vartheta\frac{\partial\mathbf{T}^e}{\partial\vartheta} : \dot{\mathbf{C}}^e - \vartheta\frac{\partial\pi_{\mathrm{en}}}{\partial\vartheta}\dot{\bar{\epsilon}}^p - \vartheta\frac{\partial\mathsf{p}_{\mathrm{en}}}{\partial\vartheta}\dot{\mathsf{e}}^p - \vartheta\frac{\partial\boldsymbol{\xi}_{\mathrm{en}}}{\partial\vartheta} \cdot \nabla\dot{\mathsf{e}}^p + c\dot{\vartheta} - \vartheta\frac{\partial\mu_L}{\partial\vartheta}\dot{C}_L - \sum_{\alpha}\vartheta\frac{\partial\mu_\alpha}{\partial\vartheta}\dot{C}_\alpha. \tag{2.119}$$

Then, using (2.119) in (2.113) gives the following partial differential equation for the temperature

$$\begin{aligned} c\dot{\vartheta} = & - \operatorname{Div} \mathbf{q}_{\mathrm{R}} + q_{\mathrm{R}} + \pi_{\mathrm{dis}} \dot{\bar{\epsilon}}^p + p_{\mathrm{dis}} \dot{e}^p + \boldsymbol{\xi}_{\mathrm{dis}} \cdot \nabla \dot{e}^p + \frac{1}{2} \vartheta \frac{\partial \mathbf{T}^e}{\partial \vartheta} : \dot{\mathbf{C}}^e + \vartheta \frac{\partial \pi_{\mathrm{en}}}{\partial \vartheta} \dot{\bar{\epsilon}}^p + \vartheta \frac{\partial p_{\mathrm{en}}}{\partial \vartheta} \dot{e}^p \\ & + \vartheta \frac{\partial \boldsymbol{\xi}_{\mathrm{en}}}{\partial \vartheta} \cdot \nabla \dot{e}^p + \vartheta \frac{\partial \mu_L}{\partial \vartheta} \dot{C}_L + \nabla \mu_L \cdot \mathbf{M}_L \nabla \mu_L \\ & + \sum_{\alpha} \Big(\vartheta \frac{\partial \mu_\alpha}{\partial \vartheta} \dot{C}_\alpha + \nabla \mu_\alpha \cdot \mathbf{M}_\alpha \nabla \mu_\alpha + (\mu_L - \mu_\alpha) h_{\mathrm{L} \to \alpha} \Big). \end{aligned} \tag{2.120}$$

2.9 Isotropy

The following definitions help to make precise our notion of an isotropic material (cf., Anand and Gurtin, 2003):

(i) Orth$^+$= the group of all rotations (the proper orthogonal group);

(ii) the *symmetry group* $\mathcal{G}_{\mathrm{R}}$, is the group of all rotations of the *reference* configuration that leaves the response of the material unaltered;

(iii) the *symmetry group* $\mathcal{G}_{\mathrm{I}}$ at each time t, is the group of all rotations of the *intermediate* space that leaves the response of the material unaltered.

We now discuss the manner in which the basic fields transform under such transformations, granted the physically natural requirement of invariance of the stress-power (2.71), or equivalently, the requirement that

$$\mathbf{S}^e : \dot{\mathbf{F}}^e \quad \text{and} \quad \mathbf{T}^e : \dot{\mathbf{C}}^e \quad \text{be invariant.} \tag{2.121}$$

2.9.1 Isotropy of the reference configuration

Let $\mathbf{Q}$ be a time-independent rotation of the reference configuration. Then $\mathbf{F} \to \mathbf{FQ}$, and hence

$$\mathbf{F}^p \to \mathbf{F}^p\mathbf{Q}, \quad \mathbf{F}^e \, \text{is invariant, and hence} \, \mathbf{C}^e \, \text{is invariant,} \tag{2.122}$$

so that

$$\dot{\mathbf{F}}^e \, \text{and} \, \dot{\mathbf{C}}^e \, \text{are invariant.} \tag{2.123}$$

We may therefor use (2.121) to conclude that

$$\mathbf{S}^e \, \text{and} \, \mathbf{T}^e \, \text{are invariant.} \tag{2.124}$$

Thus

- The constitutive equations (2.80) are unaffected by such rotations of the reference configuration.

Turning our attention next to the constitutive equation $(2.101)_1$ for the heat flux, a standard result from the theory of finite thermoelasticity is that under a symmetry transformation $\mathbf{Q}$ of the reference configuration, the temperature gradient $\nabla\vartheta$ and the heat flux $\mathbf{q}_{\mathrm{R}}$ transform as (cf., Gurtin et al., 2010, Section 57.8)

$$\nabla\vartheta \to \mathbf{Q}^{\scriptscriptstyle\top}\nabla\vartheta, \qquad \mathbf{q}_{\mathrm{R}} \to \mathbf{Q}^{\scriptscriptstyle\top}\mathbf{q}_{\mathrm{R}}. \tag{2.125}$$

Hence, from $(2.101)_1$ the thermal conductivity tensor $\mathbf{K}$ must obey

$$\hat{\mathbf{K}}(\tilde{\Lambda}) = \mathbf{Q}^{\scriptscriptstyle\top}\hat{\mathbf{K}}(\tilde{\Lambda})\mathbf{Q} \quad \text{for all rotations}\, \mathbf{Q} \in \mathcal{G}_{\mathrm{R}}. \tag{2.126}$$

By an analogous argument, the mobility tensors $\mathbf{M}_L$ and $\mathbf{M}_\alpha$ must obey

$$\hat{\mathbf{M}}_L(\tilde{\Lambda}) = \mathbf{Q}^{\scriptscriptstyle\top}\hat{\mathbf{M}}_L(\tilde{\Lambda})\mathbf{Q} \quad \text{and} \quad \hat{\mathbf{M}}_\alpha(\tilde{\Lambda}) = \mathbf{Q}^{\scriptscriptstyle\top}\hat{\mathbf{M}}_\alpha(\tilde{\Lambda})\mathbf{Q} \quad \text{for all rotations}\, \mathbf{Q} \in \mathcal{G}_{\mathrm{R}}. \tag{2.127}$$

We refer to the material as *initially isotropic* (and to the reference configuration as undistorted) if

$$\mathcal{G}_{\mathrm{R}} = \mathrm{Orth}^+ \tag{2.128}$$

so that the response of the material is invariant under arbitrary rotations of the reference space. Henceforth *we restrict attention to materials that are initially isotropic.*

In this case, the thermal conductivity and the mobility tensors have the representation

$$\hat{\mathbf{K}}(\tilde{\Lambda}) = \hat{\kappa}(\tilde{\Lambda})\mathbf{1}, \tag{2.129}$$

with $\kappa > 0$ a scalar thermal conductivity, and

$$\hat{\mathbf{M}}_L(\tilde{\Lambda}) = \hat{m}_L(\tilde{\Lambda})\mathbf{1} \quad \text{and} \quad \hat{\mathbf{M}}_\alpha(\tilde{\Lambda}) = \hat{m}_\alpha(\tilde{\Lambda})\mathbf{1}, \tag{2.130}$$

with $m_L > 0$ and $m_\alpha > 0$ scalar mobilities.

2.9.2 Isotropy of the intermediate structural space

Next, let $\mathbf{Q}$, a time-independent rotation of the intermediate space, be a symmetry transformation. Then $\mathbf{F}$ is unaltered by such a rotation, and hence

$$\mathbf{F}^e \to \mathbf{F}^e\mathbf{Q} \quad \text{and} \quad \mathbf{F}^p \to \mathbf{Q}^{\scriptscriptstyle\top}\mathbf{F}^p, \tag{2.131}$$

and also

$$\mathbf{C}^e \to \mathbf{Q}^{\scriptscriptstyle\top}\mathbf{C}^e\mathbf{Q}, \quad \dot{\mathbf{C}}^e \to \mathbf{Q}^{\scriptscriptstyle\top}\dot{\mathbf{C}}^e\mathbf{Q}, \quad \dot{\mathbf{F}}^e \to \mathbf{Q}^{\scriptscriptstyle\top}\dot{\mathbf{F}}^e\mathbf{Q} \tag{2.132}$$

then (2.132) and (2.121) yield the transformation laws

$$\mathbf{S}^e \to \mathbf{Q}^{\scriptscriptstyle\top}\mathbf{S}^e\mathbf{Q}, \quad \mathbf{T}^e \to \mathbf{Q}^{\scriptscriptstyle\top}\mathbf{T}^e\mathbf{Q}. \tag{2.133}$$

Thus, with reference to the constitutive equations (2.80) together with (2.129) and (2.130) we conclude that

$$\left.\begin{aligned}
\hat{\psi}_{\mathrm{R}}(\Lambda) &= \hat{\psi}(\mathbf{Q}^{\top}\Lambda\mathbf{Q}),\\
\mathbf{Q}^{\top}\hat{\mathbf{T}}^{e}(\Lambda)\mathbf{Q} &= \hat{\mathbf{T}}^{e}(\mathbf{Q}^{\top}\Lambda\mathbf{Q}),\\
\hat{\eta}_{\mathrm{R}}(\Lambda) &= \hat{\eta}_{\mathrm{R}}(\mathbf{Q}^{\top}\Lambda\mathbf{Q}),\\
\hat{\mu}_{L}(\Lambda) &= \hat{\mu}_{L}(\mathbf{Q}^{\top}\Lambda\mathbf{Q}),\\
\hat{\mu}_{\alpha}(\Lambda) &= \hat{\mu}_{\alpha}(\mathbf{Q}^{\top}\Lambda\mathbf{Q}),\\
\hat{\pi}(\Lambda) &= \hat{\pi}(\mathbf{Q}^{\top}\Lambda\mathbf{Q}),\\
\hat{p}(\Lambda) &= \hat{p}(\mathbf{Q}^{\top}\Lambda\mathbf{Q}),\\
\hat{\boldsymbol{\xi}}(\Lambda) &= \hat{\boldsymbol{\xi}}(\mathbf{Q}^{\top}\Lambda\mathbf{Q}),\\
\hat{\kappa}(\tilde{\Lambda}) &= \hat{\kappa}(\mathbf{Q}^{\top}\tilde{\Lambda}\mathbf{Q}),\\
\hat{m}_{L}(\tilde{\Lambda}) &= \hat{m}_{L}(\mathbf{Q}^{\top}\tilde{\Lambda}\mathbf{Q}),\\
\hat{m}_{\alpha}(\tilde{\Lambda}) &= \hat{m}_{\alpha}(\mathbf{Q}^{\top}\tilde{\Lambda}\mathbf{Q}),
\end{aligned}\right\} \tag{2.134}$$

with

$$\left.\begin{aligned}
\mathbf{Q}^{\top}\Lambda\mathbf{Q} &= (\mathbf{Q}^{\top}\mathbf{C}^{e}\mathbf{Q}, \bar{e}^{p}, e^{p}, \mathbf{Q}^{\top}\nabla e^{p}, \vartheta, C_L, C_\alpha),\\
\mathbf{Q}^{\top}\tilde{\Lambda}\mathbf{Q} &= (\mathbf{Q}^{\top}\mathbf{C}^{e}\mathbf{Q}, \bar{e}^{p}, \vartheta, C_L, C_\alpha),
\end{aligned}\right\} \tag{2.135}$$

which must hold for all rotations $\mathbf{Q}$ in the symmetry group $\mathcal{G}_{\mathrm{I}}$ at each time t.

We refer to the material as one which is *continually isotropic*, if in addition to the referential isotropy discussed in the previous subsection,

$$\mathcal{G}_{\mathrm{I}} = \mathrm{Orth}^{+} \tag{2.136}$$

so that the response of the material is also invariant under arbitrary rotations of the intermediate space at each time t. Henceforth *we restrict attention to materials that are not only initially, but also continually, isotropic.*

In this case, the response functions $\hat{\psi}_{\mathrm{R}}$, $\hat{\mathbf{T}}^{e}$, $\hat{\eta}_{\mathrm{R}}$, $\hat{\mu}_{L}$, $\hat{\mu}_{\alpha}$, $\hat{\pi}$, $\hat{p}$, $\hat{\boldsymbol{\xi}}$, $\hat{\kappa}$, $\hat{m}_{L}$, and $\hat{m}_{\alpha}$ must also each be *isotropic*.

2.9.3 Isotropic free energy

An immediate consequence of the isotropy of the free energy is that the free energy function has the representation

$$\hat{\psi}_{\mathrm{R}}(\mathbf{C}^{e}, \bar{e}^{p}, e^{p}, \nabla e^{p}, \vartheta, C_L, C_\alpha) = \tilde{\psi}_{\mathrm{R}}(\mathcal{I}_{\mathbf{C}^{e}}, \bar{e}^{p}, e^{p}, |\nabla e^{p}|, \vartheta, C_L, C_\alpha) \tag{2.137}$$

where

$$\mathcal{I}_{\mathbf{C}^{e}} = (I_1(\mathbf{C}^{e}), I_2(\mathbf{C}^{e}), I_3(\mathbf{C}^{e})) \tag{2.138}$$

is the list of principal invariants of $\mathbf{C}^e$. Thus, from $(2.86)_1$, it follows that

$$\mathbf{T}^e = 2\frac{\partial\tilde{\psi}_{\mathrm{R}}(\mathcal{I}_{\mathbf{C}^e}, \vec{\epsilon}^p, \mathsf{e}^p, |\nabla \mathsf{e}^p|, \vartheta, C_L, C_\alpha)}{\partial\mathbf{C}^e} \tag{2.139}$$

and that $\mathbf{T}^e$ is an *isotropic function* of $\mathbf{C}^e$. Then since the Mandel stress can be expressed by (cf. (2.79))

$$\mathbf{M}^e = \mathbf{C}^e\mathbf{T}^e \tag{2.140}$$

we find that $\mathbf{T}^e$ and $\mathbf{C}^e$ commute,

$$\mathbf{C}^e\mathbf{T}^e = \mathbf{T}^e\mathbf{C}^e \tag{2.141}$$

and hence the Mandel stress $\mathbf{M}^e$ is *symmetric.*

Next the spectral representation of $\mathbf{C}^e$ is

$$\mathbf{C}^e = \sum_{i=1}^{3}(\lambda_i^e)^2\mathbf{r}_i^e \otimes \mathbf{r}_i^e \tag{2.142}$$

where $(\mathbf{r}_1^e, \mathbf{r}_2^e, \mathbf{r}_3^e)$ are the orthonormal eigenvectors of $\mathbf{C}^e$ and $\mathbf{U}^e$, and $(\lambda_1^e, \lambda_2^e, \lambda_3^e)$ are the eigenvalues of $\mathbf{U}^e$. Instead of using the invariants $\mathcal{I}_{\mathbf{C}^e}$, the free energy $\tilde{\psi}_{\mathrm{R}}$ for isotropic materials may be alternatively expressed in terms of the principal stretches as

$$\psi_{\mathrm{R}} = \breve{\psi}_{\mathrm{R}}(\lambda_1^e, \lambda_2^e, \lambda_3^e, \vec{\epsilon}^p, \mathsf{e}^p, |\nabla \mathsf{e}^p|, \vartheta, C_L, C_\alpha). \tag{2.143}$$

Then, by the chain-rule and $(2.86)_1$, the stress $\mathbf{T}^e$ is given by

$$\begin{aligned}
\mathbf{T}^e &= 2\frac{\partial\breve{\psi}_{\mathrm{R}}(\lambda_1^e, \lambda_2^e, \lambda_3^e, \vec{\epsilon}^p, \mathsf{e}^p, |\nabla \mathsf{e}^p|, \vartheta, C_L, C_\alpha)}{\partial\mathbf{C}^e} \\
&= 2\sum_{i=1}^{3}\frac{\partial\breve{\psi}_{\mathrm{R}}(\lambda_1^e, \lambda_2^e, \lambda_3^e, \vec{\epsilon}^p, \mathsf{e}^p, |\nabla \mathsf{e}^p|, \vartheta, C_L, C_\alpha)}{\partial\lambda_i^e}\frac{\partial\lambda_i^e}{\partial\mathbf{C}^e} \\
&= \sum_{i=1}^{3}\frac{1}{\lambda_i^e}\frac{\partial\breve{\psi}_{\mathrm{R}}(\lambda_1^e, \lambda_2^e, \lambda_3^e, \vec{\epsilon}^p, \mathsf{e}^p, |\nabla \mathsf{e}^p|, \vartheta, C_L, C_\alpha)}{\partial\lambda_i^e}\frac{\partial(\lambda_i^e)^2}{\partial\mathbf{C}^e}.
\end{aligned} \tag{2.144}$$

Assume that the squared principal stretches $(\lambda_i^e)^2$ are distinct, so that the $(\lambda_i^e)^2$ and the principal directions $\mathbf{r}_i^e$ may be considered as functions of $\mathbf{C}^e$; then

$$\frac{\partial(\lambda_i^e)^2}{\partial\mathbf{C}^e} = \mathbf{r}_i^e \otimes \mathbf{r}_i^e \tag{2.145}$$

and, granted this, (2.145) and (2.144) imply that

$$\mathbf{T}^e = \sum_{i=1}^{e}\frac{1}{\lambda_i^e}\frac{\partial\breve{\psi}_{\mathrm{R}}(\lambda_1^e, \lambda_2^e, \lambda_3^e, \vec{\epsilon}^p, \mathsf{e}^p, |\nabla \mathsf{e}^p|, \vartheta, C_L, C_\alpha)}{\partial\lambda_i^e}\mathbf{r}_i^e \otimes \mathbf{r}_i^e. \tag{2.146}$$

Next, since $\mathbf{M}^e = \mathbf{C}^e\mathbf{T}^e$, use of (2.142) and (2.146) gives the Mandel stress as

$$\mathbf{M}^e = \sum_{i=1}^{3} \lambda_i^e \frac{\partial \breve{\psi}_{\mathrm{R}}(\lambda_1^e, \lambda_2^e, \lambda_3^e, \bar{\epsilon}^p, \mathrm{e}^p, |\nabla \mathrm{e}^p|, \vartheta, C_L, C_\alpha)}{\partial \lambda_i^e} \mathbf{r}_i^e \otimes \mathbf{r}_i^e. \tag{2.147}$$

Let

$$\mathbf{E}^e \overset{\text{def}}{=} \sum_{i=1}^{3} E_i^e \mathbf{r}_i^e \otimes \mathbf{r}_i^e, \tag{2.148}$$

denote the logarithmic elastic strain with principal values

$$E_i^e \overset{\text{def}}{=} \ln \lambda_i^e, \tag{2.149}$$

and consider a free energy of the form

$$\breve{\psi}_{\mathrm{R}}(\lambda_1^e, \lambda_2^e, \lambda_3^e, \bar{\epsilon}^p, \mathrm{e}^p, |\nabla \mathrm{e}^p|, \vartheta, C_L, C_\alpha) = \breve{\psi}_{\mathrm{R}}(E_1^e, E_2^e, E_3^e, \bar{\epsilon}^p, \mathrm{e}^p, |\nabla \mathrm{e}^p|, \vartheta, C_L, C_\alpha) \tag{2.150}$$

so that, using (2.147),

$$\mathbf{M}^e = \sum_{i=1}^{3} \frac{\breve{\psi}_{\mathrm{R}}(E_1^e, E_2^e, E_3^e, \bar{\epsilon}^p, \mathrm{e}^p, |\nabla \mathrm{e}^p|, \vartheta, C_L, C_\alpha)}{\partial E_i^e} \mathbf{r}_i^e \otimes \mathbf{r}_i^e \tag{2.151}$$

With the logarithmic elastic strain defined by (2.148), and bearing (2.150) and (2.151), for isotropic elastic materials we henceforth consider a free energy of the form

$$\psi_{\mathrm{R}} = \bar{\psi}(\mathcal{I}_{\mathbf{E}^e}, \bar{\epsilon}^p, \mathrm{e}^p, |\nabla \mathrm{e}^p|, \vartheta, C_L, C_\alpha) \tag{2.152}$$

with $\mathcal{I}_{\mathbf{E}^e}$ a list of principal invariants of $\mathbf{E}^e$, or equivalently a list of principal values of $\mathbf{E}^e$. The Mandel stress is finally given by

$$\mathbf{M}^e = \frac{\partial \bar{\psi}_{\mathrm{R}}(\mathcal{I}_{\mathbf{E}^e}, \bar{\epsilon}^p, \mathrm{e}^p, |\nabla \mathrm{e}^p|, \vartheta, C_L, C_\alpha)}{\partial \mathbf{E}^e}. \tag{2.153}$$

Further, using (2.146) in (2.79),

$$\begin{aligned}
\mathbf{T} &= J^{-1}\mathbf{F}^e\mathbf{T}^e\mathbf{F}^{e\top} \\
&= J^{-1}\mathbf{R}^e\mathbf{U}^e\mathbf{T}^e\mathbf{U}^e\mathbf{R}^{e\top} \\
&= J^{-1}\mathbf{R}^e \left(\sum_{i=1}^{e} \lambda_i^e \frac{\partial \breve{\psi}_{\mathrm{R}}(\lambda_1^e, \lambda_2^e, \lambda_3^e, \bar{\epsilon}^p, \mathrm{e}^p, |\nabla \mathrm{e}^p|, \vartheta, C_L, C_\alpha)}{\partial \lambda_i^e} \mathbf{r}_i^e \otimes \mathbf{r}_i^e \right) \mathbf{R}^{e\top}
\end{aligned} \tag{2.154}$$

and using (2.147) the Cauchy stress is given by

$$\mathbf{T} = J^{-1}\mathbf{R}^e\mathbf{M}^e\mathbf{R}^{e\top}. \tag{2.155}$$

2.10 Summary

In this section we summarize our isotropic chemo-thermo-mechanically coupled gradient theory. The theory relates the following basic fields:

$\mathbf{x} = \boldsymbol{\chi}(\mathbf{X}, t)$	motion
$\mathbf{F} = \nabla\boldsymbol{\chi}, \quad J = \det\mathbf{F} > 0$	deformation gradient
$\mathbf{F} = \mathbf{F}^e\mathbf{F}^p$	multiplicative decomposition of $\mathbf{F}$
$\mathbf{F}^e, \quad J^e = \det\mathbf{F}^e > 0$	elastic distortion
$\mathbf{F}^p, \quad J^p = 1$	plastic distortion
$\mathbf{F}^e = \mathbf{R}^e\mathbf{U}^e$	polar decomposition of $\mathbf{F}^e$
$\mathbf{C}^e = \mathbf{F}^{e\top}\mathbf{F}^e = (\mathbf{U}^e)^2$	elastic right Cauchy-Green tensor
$\mathbf{U}^e = \sum_{i=1}^{3} \lambda_i^e\, \mathbf{r}_i^e \otimes \mathbf{r}_i^e$	spectral decomposition of $\mathbf{U}^e$
$\mathbf{E}^e = \sum_{i=1}^{e} (\ln \lambda_i^e)\, \mathbf{r}_i^e \otimes \mathbf{r}_i^e$	logarithmic elastic strain
$\mathbf{T} = \mathbf{T}^\top$	Cauchy stress
$\mathbf{T}^e = J\mathbf{F}^{e-1}\mathbf{T}\mathbf{F}^{e-\top}$	elastic second Piola stress
$\mathbf{M}^e = \mathbf{C}^e\mathbf{T}^e$	Mandel stress
$\mathbf{T}_\mathrm{R} = J\mathbf{T}\mathbf{F}^{-\top}$	Piola stress
π	microscopic stress
ψ_R	free energy density per unit reference volume
η_R	entropy density per unit reference volume
$\vartheta > 0$	absolute temperature
$\nabla\vartheta$	referential temperature gradient
$\mathbf{q}_\mathrm{R}$	referential heat flux vector
C_L	number of moles of lattice hydrogen per unit reference volume
C_α	number of moles of trapped hydrogen per unit reference volume
$h_{\mathrm{L}\to\alpha}$	transformation rate between lattice and trapped hydrogen atoms
μ_L	lattice hydrogen chemical potential
μ_α	trapped hydrogen chemical potential
$\nabla\mu_L$	referential gradient of the lattice hydrogen chemical potential
$\nabla\mu_\alpha$	referential gradient of the trapped hydrogen chemical potential
$\mathbf{j}_L$	referential lattice hydrogen flux vector
$\mathbf{j}_\alpha$	referential trapped hydrogen flux vector
e^p	scalar internal microvariable
∇e^p	referential gradient of the scalar internal microvariable
p	scalar microscopic stress
$\boldsymbol{\xi}$	vector microscopic stress

2.10.1 Constitutive equations

1. **Free energy**

$$\psi_{\mathrm{R}} = \bar{\psi}_{\mathrm{R}}(\mathcal{I}_{\mathbf{E}^e}, \bar{e}^p, e^p, |\nabla e^p|, \vartheta, C_L, C_\alpha) \tag{2.156}$$

where $\mathcal{I}_{\mathbf{E}^e}$ represents a list of the principal invariants of the logarithmic elastic strain $\mathbf{E}^e$.

2. **Cauchy stress. Mandel stress**

The Cauchy stress is given by

$$\mathbf{T} = J^{-1}\mathbf{R}^e\mathbf{M}^e\mathbf{R}^{e\top} \tag{2.157}$$

where

$$\mathbf{M}^e = \frac{\partial\bar{\psi}_{\mathrm{R}}(\mathcal{I}_{\mathbf{E}^e}, \bar{e}^p, e^p, |\nabla e^p|, \vartheta, C_L, C_\alpha)}{\partial\mathbf{E}^e} \tag{2.158}$$

is the Mandel stress, which, on account of the isotropy of $\bar{\psi}_{\mathrm{R}}$ is symmetric. The Piola stress is given by

$$\mathbf{T}_{\mathrm{R}} = J\mathbf{T}\mathbf{F}^{-\top}. \tag{2.159}$$

3. **Microscopic stresses π, p, and $\boldsymbol{\xi}$**

The microscopic stresses π, p, and $\boldsymbol{\xi}$ are additively decomposed into energetic and dissipative parts

$$\left.\begin{aligned} \pi &= \pi_{\mathrm{en}} + \pi_{\mathrm{dis}} \\ p &= p_{\mathrm{en}} + p_{\mathrm{dis}} \quad \text{with} \\ \boldsymbol{\xi} &= \boldsymbol{\xi}_{\mathrm{en}} + \boldsymbol{\xi}_{\mathrm{dis}} \end{aligned} \quad \begin{aligned} \pi_{\mathrm{en}} &= \frac{\partial\bar{\psi}_{\mathrm{R}}(\mathcal{I}_{\mathbf{E}^e}, \bar{e}^p, e^p, |\nabla e^p|, \vartheta, C_L, C_\alpha)}{\partial\bar{e}^p} \\ p_{\mathrm{en}} &= \frac{\partial\bar{\psi}_{\mathrm{R}}(\mathcal{I}_{\mathbf{E}^e}, \bar{e}^p, e^p, |\nabla e^p|, \vartheta, C_L, C_\alpha)}{\partial e^p} \\ \boldsymbol{\xi}_{\mathrm{en}} &= \frac{\partial\bar{\psi}_{\mathrm{R}}(\mathcal{I}_{\mathbf{E}^e}, \bar{e}^p, e^p, |\nabla e^p|, \vartheta, C_L, C_\alpha)}{\partial\nabla e^p} \end{aligned}\right\} \tag{2.160}$$

and with the dissipative parts of p and $\boldsymbol{\xi}$ given by constitutive equations

$$\left.\begin{aligned} p_{\mathrm{dis}} &= \bar{p}_{\mathrm{dis}}(\bar{e}^p, \dot{\bar{e}}^p, e^p, \dot{e}^p, \nabla e^p, \nabla\dot{e}^p, \vartheta, C_L, C_\alpha), \\ \boldsymbol{\xi}_{\mathrm{dis}} &= \bar{\boldsymbol{\xi}}_{\mathrm{dis}}(\bar{e}^p, \dot{\bar{e}}^p, e^p, \dot{e}^p, \nabla e^p, \nabla\dot{e}^p, \vartheta, C_L, C_\alpha), \end{aligned}\right\} \tag{2.161}$$

and the dissipative part of π given next.

4. **Evolution equation for $\mathbf{F}^p$. Equation for the dissipative microscopic stress π_{dis}**

The evolution equation for $\mathbf{F}^p$ is

$$\dot{\mathbf{F}}^p = \mathbf{D}^p\mathbf{F}^p, \tag{2.162}$$

where $\mathbf{D}^p$ is given by

$$\mathbf{D}^p = \frac{3}{2}\dot{\bar{e}}^p\frac{\mathbf{M}_0^e}{\bar{\sigma}} \tag{2.163}$$

and according to the microscopic force balance (2.59) and the decomposition (2.160)

$$\bar{\sigma} = \pi_{\mathrm{en}} + \pi_{\mathrm{dis}}. \tag{2.164}$$

The dissipative part of the microscopic stress π_{dis} is given by a rate-independent constitutive equation

$$\pi_{\text{dis}} = \bar{Y}_{\text{dis}}(\bar{\epsilon}^p, e^p, \vartheta, C_L, C_\alpha) > 0 \tag{2.165}$$

where $\bar{Y}_{\text{dis}}(\bar{\epsilon}^p, e^p, \vartheta, C_L, C_\alpha)$ is a positive-valued scalar with dimensions of stress representing the rate-independent flow resistance of the material. The initial value

$$Y_0 \overset{\text{def}}{=} \bar{Y}_{\text{dis}}(0, 0, \vartheta_0, C_L^0, C_\alpha^0) > 0, \tag{2.166}$$

represents the initial yield strength of the material. Furthermore, let

$$\bar{Y}(\bar{\epsilon}^p, e^p, \vartheta, C_L, C_\alpha) = \bar{Y}_{\text{dis}}(\bar{\epsilon}^p, e^p, \vartheta, C_L, C_\alpha) + \bar{Y}_{\text{en}}(\bar{\epsilon}^p, e^p, \vartheta, C_L, C_\alpha), \tag{2.167}$$

with $Y_{\text{en}} = \pi_{\text{en}}$, represents the combined dissipative and energetic parts of the constitutive equation for π. Then the microscopic force balance (2.59) requires that

$$\bar{\sigma} = \bar{Y}(\bar{\epsilon}^p, e^p, \vartheta, C_L, C_\alpha) \quad \text{when} \quad \dot{\bar{\epsilon}}^p > 0. \tag{2.168}$$

5. **Yield function. Kuhn-Tucker and consistency condition**

We introduce a yield function

$$f \overset{\text{def}}{=} \bar{\sigma} - Y(\bar{\epsilon}^p, e^p, \vartheta, C_L, C_\alpha) \leq 0. \tag{2.169}$$

Then, as is standard, a rate-independent theory is based on the Kuhn-Tucker conditions

$$\dot{\bar{\epsilon}}^p \geq 0, \quad f \leq 0, \quad \text{and} \quad \dot{\bar{\epsilon}}^p f = 0, \tag{2.170}$$

together with the consistency condition

$$\dot{\bar{\epsilon}}^p \dot{f} = 0 \quad \text{when} \quad f = 0. \tag{2.171}$$

6. **Entropy. Chemical potentials**

The partial derivatives of the free energy

$$\left.\begin{aligned}
\eta_{\text{R}} &= -\frac{\partial \bar{\psi}_{\text{R}}(\mathcal{I}_{\mathbf{E}^e}, \bar{\epsilon}^p, e^p, |\nabla e^p|, \vartheta, C_L, C_\alpha)}{\partial \vartheta} \\
\mu_L &= \frac{\partial \bar{\psi}_{\text{R}}(\mathcal{I}_{\mathbf{E}^e}, \bar{\epsilon}^p, e^p, |\nabla e^p|, \vartheta, C_L, C_\alpha)}{\partial C_L} \\
\mu_\alpha &= \frac{\partial \bar{\psi}_{\text{R}}(\mathcal{I}_{\mathbf{E}^e}, \bar{\epsilon}^p, e^p, |\nabla e^p|, \vartheta, C_L, C_\alpha)}{\partial C_\alpha}
\end{aligned}\right\} \tag{2.172}$$

respectively, represent the entropy, the chemical potential of the lattice hydrogen, and the chemical potentials of the trapped hydrogen.

7. **Rate of transformation between C_L and C_α**

   The transformation rates $h_{\mathrm{L}\to\alpha}$ are assumed to obey constitutive relations of the form

$$h_{\mathrm{L}\to\alpha} = \bar{h}_{\mathrm{L}\to\alpha}(\bar{\epsilon}^p, \vartheta, C_L, C_\alpha), \quad \forall\, \alpha, \tag{2.173}$$

   with $(\mu_L - \mu_\alpha)h_{\mathrm{L}\to\alpha} \geq 0$ for all α.

8. **Fourier's law**

   The heat flux $\mathbf{q}_{\mathrm{R}}$ is presumed to obey Fourier's law,

$$\mathbf{q}_{\mathrm{R}} = -\kappa \nabla \vartheta \tag{2.174}$$

   with $\bar{\kappa}(\mathcal{I}_{\mathbf{E}^e}, \bar{\epsilon}^p, \vartheta, C_L, C_\alpha) > 0$ the thermal conductivity.

9. **Fick's law**

   The hydrogen fluxes $\mathbf{j}_L$ and $\mathbf{j}_\alpha$ are presumed to obey Fick's law

$$\left.\begin{aligned} \mathbf{j}_L &= -m_L \nabla \mu_L \\ \mathbf{j}_\alpha &= -m_\alpha \nabla \mu_\alpha \end{aligned}\right\} \tag{2.175}$$

   with $\bar{m}_L(\mathcal{I}_{\mathbf{E}^e}, \bar{\epsilon}^p, \vartheta, C_L, C_\alpha) \geq 0$ and $\bar{m}_\alpha(\mathcal{I}_{\mathbf{E}^e}, \bar{\epsilon}^p, \vartheta, C_L, C_\alpha) \geq 0$ the lattice and trapped hydrogen mobilities.

2.10.2 Governing partial differential equations

The governing partial differential equations consist of:

1. The local macroscopic force balance (2.51), viz.

$$\operatorname{Div} \mathbf{T}_{\mathrm{R}} + \mathbf{b}_{0\mathrm{R}} = \mathbf{0}, \tag{2.176}$$

   with $\mathbf{T}_{\mathrm{R}}$ given by (2.159) and $\mathbf{b}_{0\mathrm{R}}$ the body force.

2. The local balance equations for the hydrogen concentration (2.65), which together with (2.175), give

$$\left.\begin{aligned} \dot{C}_L &= \operatorname{Div}(m_L \nabla \mu_L) - \sum_\alpha h_{\mathrm{L}\to\alpha}, \\ \dot{C}_\alpha &= \operatorname{Div}(m_\alpha \nabla \mu_\alpha) + h_{\mathrm{L}\to\alpha}, \quad \forall\, \alpha. \end{aligned}\right\} \tag{2.177}$$

3. The local balance of energy (2.120), which, together with (2.174) and (2.175), gives the following partial differential equation for the temperature

$$
\begin{aligned}
c\dot{\vartheta} =& \mathrm{Div}\,(\kappa\nabla\vartheta) + q_{\mathrm{R}} + \pi_{\mathrm{dis}}\dot{\epsilon}^p + \mathsf{p}_{\mathrm{dis}}\dot{\mathsf{e}}^p + \boldsymbol{\xi}_{\mathrm{dis}}\cdot\nabla\dot{\mathsf{e}}^p + \frac{1}{2}\vartheta\frac{\partial\mathbf{T}^e}{\partial\vartheta}:\dot{\mathbf{C}}^e + \vartheta\frac{\partial\pi_{\mathrm{en}}}{\partial\vartheta}\dot{\epsilon}^p \\
&+ \vartheta\frac{\partial\mathsf{p}_{\mathrm{en}}}{\partial\vartheta}\dot{\mathsf{e}}^p + \vartheta\frac{\partial\boldsymbol{\xi}_{\mathrm{en}}}{\partial\vartheta}\cdot\nabla\dot{\mathsf{e}}^p + \vartheta\frac{\partial\mu_L}{\partial\vartheta}\dot{C}_L + m_L|\nabla\mu_L|^2 \\
&+ \sum_{\alpha}\Big(\vartheta\frac{\partial\mu_\alpha}{\partial\vartheta}\dot{C}_\alpha + m_\alpha|\nabla\mu_\alpha|^2 + (\mu_L-\mu_\alpha)h_{\mathrm{L}\to\alpha}\Big).
\end{aligned}
\tag{2.178}
$$

in which

$$c = -\vartheta\frac{\partial^2\psi_{\mathrm{R}}}{\partial\vartheta^2} \tag{2.179}$$

is the specific heat.

4. The local microscopic force balance (2.63), viz.

$$\mathrm{Div}\,\boldsymbol{\xi} - \mathsf{p} = 0. \tag{2.180}$$

2.11 Specialization of the constitutive equations

The theory presented thus far is quite general. We now introduce special constitutive equations appropriate for situations in which the elastic strains are small, the temperature is closed to a fixed reference temperature ϑ_0, and the lattice hydrogen concentration C_L is close to a reference concentration C_L^0.

Furthermore, we now restrict our attention to one kind of trap site, that is $\alpha = T$ (although we restrict ourselves to one kind of trapping site, the theoretical framework laid forth in the previous sections is general enough to account for multiple trapping sites of different kinds).

We begin with some definitions:

(i) **Number of moles of lattice sites per unit reference volume, N_L:** This property of the host metal is given by

$$N_L \overset{\text{def}}{=} \varphi \frac{\rho_M}{\mathcal{M}_M} \cdot \quad (\text{mol/m}^3) \tag{2.181}$$

with φ the number of interstitial lattice sites per metal atom[5], ρ_M the mass density of the host metal (kg/m^3), and $\mathcal{M}_M$ the molar mass of the host metal (kg/mol).

(ii) **Number of moles of trap sites per unit reference volume, N_T:** Experimental measurements indicate that the trap density is a function of the history of the prior plastic deformation,[6]

$$N_T = \bar{N}_T(\bar{\epsilon}^p) \quad (\text{mol/m}^3). \tag{2.182}$$

(iii) **Occupancy fraction θ_L and θ_T:** Let

$$\theta_L \overset{\text{def}}{=} \frac{C_L}{N_L}, \quad 0 \leq \theta_L \leq 1, \tag{2.183}$$

denote the occupancy fraction of the lattice sites, and

$$\theta_T \overset{\text{def}}{=} \frac{C_T}{N_T}, \quad 0 \leq \theta_T \leq 1, \tag{2.184}$$

denote the occupancy fraction of the trap sites.

2.11.1 Free energy

We consider a separable free energy of the form

$$\psi_{\mathrm{R}}(\mathcal{I}_{\mathbf{E}^e}, \bar{\epsilon}^p, e^p, |\nabla e^p|, \vartheta, C_L, C_T) = \bar{\psi}^e(\mathcal{I}_{\mathbf{E}^e}, \vartheta, C_L, C_T) + \bar{\psi}^{\text{mix}}(\vartheta, C_L, C_T) + \bar{\psi}^{\text{grad}}(\bar{\epsilon}^p, e^p, |\nabla e^p|) \tag{2.185}$$

Here:

---

[5] For example, for a BCC lattice and assuming tetrahedral occupancy of hydrogen the number of interstitial lattice sites per metal atom $\varphi = 6$, see Krom and Bakker (2000).

[6] It is possible that N_T also depends on temperature, but for simplicity we neglect any such temperature dependence here.

(i) ψ^e is a thermo-chemo-elastic energy given by

$$\begin{aligned}\bar{\psi}^e(\mathcal{I}_{\mathbf{E}^e}, \vartheta, C_L, C_T) = {} & G|\mathbf{E}^e|^2 + \frac{1}{2}\left(K - \frac{2}{3}G\right)(\operatorname{tr}\mathbf{E}^e)^2 \\ & - (3K\alpha)(\vartheta - \vartheta_0)(\operatorname{tr}\mathbf{E}^e) + c(\vartheta - \vartheta_0) - c\vartheta \ln\left(\frac{\vartheta}{\vartheta_0}\right) \\ & - (3K\beta)(C_L - C_L^0)(\operatorname{tr}\mathbf{E}^e) - (3K\beta)(C_T - C_T^0)(\operatorname{tr}\mathbf{E}^e),\end{aligned} \tag{2.186}$$

which is a simple generalization of the classical strain energy function of infinitesimal isotropic elasticity combined with a thermal entropic contribution, and contributions due to the presence of lattice and trapped hydrogen in the material. Here G is the shear modulus, K the bulk modulus, α the coefficient of thermal expansion, c the specific heat, β the coefficient of chemical expansion, ϑ_0 is a reference temperature, and C_L^0 and C_T^0 are reference lattice and trapped hydrogen concentrations.

(ii) ψ^{mix} is a chemical free energy related to the mixing of hydrogen in the host metal, given by

$$\bar{\psi}^{\text{mix}}(\vartheta, C_L, C_T) = \bar{\psi}^{\text{mix,latt}}(\vartheta, C_L) + \bar{\psi}^{\text{mix,trap}}(\vartheta, C_T), \tag{2.187}$$

with

(a) $\psi^{\text{mix,latt}}$ a chemical free energy related to the mixing of lattice hydrogen in the host metal, given by

$$\bar{\psi}^{\text{mix,latt}}(\vartheta, C_L) = \mu_L^0 C_L + R\vartheta N_L(\theta_L \ln\theta_L + (1 - \theta_L)\ln(1 - \theta_L)), \tag{2.188}$$

and

(b) $\psi^{\text{mix,trap}}$ a chemical free energy related to the mixing of trapped hydrogen in the host metal, given by

$$\bar{\psi}^{\text{mix,trap}}(\vartheta, C_T) = \mu_T^0 C_T + R\vartheta N_T(\theta_T \ln\theta_T + (1 - \theta_T)\ln(1 - \theta_T)). \tag{2.189}$$

Here μ_L^0 and μ_T^0 are reference chemical potentials, and R is the gas constant.

(iii) ψ^{grad} introduces an energetic coupling between $\bar{e}^p$ and its microscopic counterpart e^p and accounts for nonlocal effects, it is given by

$$\bar{\psi}^{\text{grad}} = \frac{1}{2}B(\bar{e}^p - e^p)^2 + \frac{1}{2}\gamma|\nabla e^p|^2, \tag{2.190}$$

where $B > 0$ and $\gamma > 0$ are constants.

Thus, combining (2.186) through (2.190), the free energy is given by

$$\begin{aligned}\psi_{\mathrm{R}} = {} & G|\mathbf{E}^e|^2 + \frac{1}{2}\left(K - \frac{2}{3}G\right)(\operatorname{tr}\mathbf{E}^e)^2 - (3K\alpha)(\vartheta - \vartheta_0)(\operatorname{tr}\mathbf{E}^e) + c(\vartheta - \vartheta_0) - c\vartheta \ln\left(\frac{\vartheta}{\vartheta_0}\right)\\ & - (3K\beta)(C_L - C_L^0)(\operatorname{tr}\mathbf{E}^e) - (3K\beta)(C_T - C_T^0)(\operatorname{tr}\mathbf{E}^e)\\ & + \mu_L^0 C_L + R\vartheta N_L\left(\theta_L \ln\theta_L + (1-\theta_L)\ln(1-\theta_L)\right)\\ & + \mu_T^0 C_T + R\vartheta N_T\left(\theta_T \ln\theta_T + (1-\theta_T)\ln(1-\theta_T)\right) + \frac{1}{2}B(\bar{e}^p - e^p)^2 + \frac{1}{2}\gamma|\nabla e^p|^2.\end{aligned} \tag{2.191}$$

Then, by (2.158) and (2.172), the Mandel stress, the entropy, and the chemical potentials are given by

$$\begin{aligned}\mathbf{M}^e &= 2G\mathbf{E}_0^e + K(\operatorname{tr}\mathbf{E}^e)\mathbf{1} - 3K\alpha(\vartheta - \vartheta_0)\mathbf{1} - 3K\beta(C - C^0)\mathbf{1},\\ \eta_{\mathrm{R}} &= c\ln\left(\frac{\vartheta}{\vartheta_0}\right) + 3K\alpha(\operatorname{tr}\mathbf{E}^e) - RN_L\left(\theta_L\ln\theta_L + (1-\theta_L)\ln(1-\theta_L)\right)\\ &\quad - RN_T\left(\theta_T\ln\theta_T + (1-\theta_T)\ln(1-\theta_T)\right),\\ \mu_L &= \mu_L^0 + R\vartheta\ln\left(\frac{\theta_L}{1-\theta_L}\right) - 3K\beta(\operatorname{tr}\mathbf{E}^e),\\ \mu_T &= \mu_T^0 + R\vartheta\ln\left(\frac{\theta_T}{1-\theta_T}\right) - 3K\beta(\operatorname{tr}\mathbf{E}^e),\end{aligned} \tag{2.192}$$

where in writing the Mandel stress $\mathbf{M}^e$ we have defined

$$C \overset{\text{def}}{=} C_L + C_T \quad \text{and} \quad C^0 \overset{\text{def}}{=} C_L^0 + C_T^0. \tag{2.193}$$

Next, taking the trace of the stress relation $(2.192)_1$ and solving for $\operatorname{tr}\mathbf{E}^e$ yields

$$\operatorname{tr}\mathbf{E}^e = \frac{1}{3K}(\operatorname{tr}\mathbf{M}^e) + 3\alpha(\vartheta - \vartheta_0) + 3\beta(C - C^0). \tag{2.194}$$

The last term in (2.194) justifies our terminology for β as a *coefficient of chemical expansion.* It is related to the *partial molar volume of hydrogen in solid solution*, $\bar{V}_H$, through

$$\beta = \frac{1}{3}\bar{V}_H. \tag{2.195}$$

2.11.2 Hydrogen trapping

We now make the assumption that trap sites are isolated, that is they do no form an extended network, and thus assume that the mobility of trapped hydrogen is zero

$$m_T = 0, \quad \text{and hence the flux of trapped hydrogen vanishes,} \quad \mathbf{j}_T = \mathbf{0}. \tag{2.196}$$

The local balance for the hydrogen concentrations (2.177) collapse into a single local balance equation

$$\dot{C}_L + \dot{C}_T = \operatorname{Div}(m_L \nabla \mu_L), \tag{2.197}$$

where the time rate of change of trapped hydrogen is now identically equal to the transformation rate

$$\dot{C}_T = h_{\mathrm{L}\to\mathrm{T}}. \tag{2.198}$$

From the dissipation inequality (2.103), and equations (2.109) and (2.198) we have that

$$(\mu_L - \mu_T)\dot{C}_T \geq 0 \quad \text{for} \quad \dot{C}_T \neq 0. \tag{2.199}$$

The term

$$\mathcal{F} \stackrel{\text{def}}{=} (\mu_L - \mu_T), \tag{2.200}$$

represents a thermodynamic force conjugate to the time rate of change of hydrogen trapping, and governs when hydrogen is captured or released from a trapping site. From $(2.192)_{3,4}$ the thermodynamic force $\mathcal{F}$ is given by

$$\mathcal{F} = \mu_L^0 + R\vartheta \ln\left(\frac{\theta_L}{1-\theta_L}\right) - \mu_T^0 - R\vartheta \ln\left(\frac{\theta_T}{1-\theta_T}\right). \tag{2.201}$$

Equilibrium between lattice and trapped hydrogen

We assume that the chemical potentials of the lattice and trapped hydrogen species satisfy

$$\mu_L = \mu_T \quad \longrightarrow \quad \mathcal{F} = 0, \tag{2.202}$$

so that they are always in **equilibrium**. Accordingly, (2.201) gives

$$\mu_L^0 + R\vartheta \ln\left(\frac{\theta_L}{1-\theta_L}\right) = \mu_T^0 + R\vartheta \ln\left(\frac{\theta_T}{1-\theta_T}\right) \tag{2.203}$$

which can be simplified to read

$$\frac{\theta_T}{1-\theta_T} = \frac{\theta_L}{1-\theta_L} K_T \tag{2.204}$$

where K_T is an equilibrium factor given by

$$K_T = \exp\left(\frac{W_B}{R\vartheta}\right) \quad \text{with} \quad W_B = \mu_L^0 - \mu_T^0 \tag{2.205}$$

the trap binding energy. **This makes precise the classical and widely-used notion of balance between lattice and trapped hydrogen of Oriani (1970).**

The time rate of change of trapped hydrogen can now be determined through the equilibrium equation (2.204). In what follows we essentially summarize the arguments of Sofronis and McMeeking (1989) and Krom et al. (1999), except that we do not restrict ourselves to isothermal conditions. Using (2.204), one finds that for low C_L, that is $\theta_L \ll 1$, the trapped hydrogen concentration C_T

may be expressed as

$$C_T = \frac{N_T}{1 + \dfrac{N_L}{K_T C_L}}. \tag{2.206}$$

The evolution of C_T is then given by

$$\dot{C}_T = \frac{\partial C_T}{\partial C_L}\dot{C}_L + \frac{\partial C_T}{\partial \bar{\epsilon}^p}\dot{\bar{\epsilon}}^p + \frac{\partial C_T}{\partial \vartheta}\dot{\vartheta}. \tag{2.207}$$

Next from (2.204)

$$\frac{\partial C_T}{\partial C_L} = \frac{C_T(1-\theta_T)}{C_L}, \tag{2.208}$$

since $\bar{\epsilon}^p$ enters C_T only through N_T, using (2.182) yields

$$\frac{\partial C_T}{\partial \bar{\epsilon}^p} = \frac{\partial C_T}{\partial N_T}\frac{dN_T}{d\bar{\epsilon}^p} = \theta_T \frac{dN_T}{d\bar{\epsilon}^p}, \tag{2.209}$$

and since ϑ enters C_T only through K_T, using (2.204) and (2.205) yields

$$\frac{\partial C_T}{\partial \vartheta} = \frac{\partial C_T}{\partial K_T}\frac{dK_T}{d\vartheta} = -\frac{C_T(1-\theta_T)W_B}{R\vartheta^2}. \tag{2.210}$$

Then, use of (2.208), (2.209), and (2.210) in (2.207) gives the following important estimate for the time rate of change of C_T:

$$\dot{C}_T = \frac{C_T(1-\theta_T)}{C_L}\dot{C}_L + \theta_T\frac{dN_T}{d\bar{\epsilon}^p}\dot{\bar{\epsilon}}^p - \frac{C_T(1-\theta_T)W_B}{R\vartheta}\frac{\dot{\vartheta}}{\vartheta}. \tag{2.211}$$

As stated above, in writing (2.206) we assume that $\theta_L \ll 1$, the same assumption will be used to modify the lattice themical potential $(2.192)_3$ to

$$\mu_L = \mu_L^0 + R\vartheta \ln\left(\frac{C_L}{N_L}\right) - 3K\beta(\mathrm{tr}\,\mathbf{E}^e). \tag{2.212}$$

Note that it is not always necessary to model hydrogen trapping through the assumption of equilibrium between lattice and trapped hydrogen (2.202). In Appendix A we illustrate how our thermodynamic framework can be used to model non-equilibrium trapping of hydrogen.

2.11.3 Microscopic stresses. Microforce balance

The use of (2.191) in (2.160) yields the energetic portion of the microscopic stresses p and $\boldsymbol{\xi}$ as

$$\begin{aligned} p_{\mathrm{en}} &= -B(\bar{\epsilon}^p - e^p), \\ \boldsymbol{\xi}_{\mathrm{en}} &= \gamma \nabla e^p. \end{aligned} \tag{2.213}$$

We assume further that

$$p_{\mathrm{dis}} = 0 \quad \text{and} \quad \boldsymbol{\xi}_{\mathrm{dis}} = \mathbf{0}, \tag{2.214}$$

such that

$$\begin{aligned} p &= p_{\text{en}} + p_{\text{dis}} = -B(\bar{\epsilon}^p - e^p), \\ \boldsymbol{\xi} &= \boldsymbol{\xi}_{\text{en}} + \boldsymbol{\xi}_{\text{dis}} = \gamma \nabla e^p. \end{aligned} \tag{2.215}$$

Finally, using the divergence of $(2.215)_2$,

$$\operatorname{Div}\boldsymbol{\xi} = \gamma \Delta e^p, \tag{2.216}$$

these constitutive relations and the local microscopic force balance (2.180) yield

$$\gamma \Delta e^p + B(\bar{\epsilon}^p - e^p) = 0, \tag{2.217}$$

or equivalently that

$$e^p - l^2 \Delta e^p = \bar{\epsilon}^p \tag{2.218}$$

which involves an energetic length parameter

$$l \overset{\text{def}}{=} \sqrt{\frac{\gamma}{B}}. \tag{2.219}$$

As noted in Anand et al. (2012) in simulations of plastic softening which result in shear band formation, the shear band widths are controlled not only by the energetic length parameter l but also by the specific value of B as well as other parameters that govern the plastic softening of the material.

2.11.4 Plastic flow resistance

The use of (2.191) in (2.160) yields the energetic portion of the microscopic stress π as

$$\pi_{\text{en}} = B(\bar{\epsilon}^p - e^p) + \frac{\partial \psi_{\text{R}}}{\partial N_T} \frac{dN_T}{d\bar{\epsilon}^p}. \tag{2.220}$$

Recall from (2.168) that

$$\bar{\sigma} = Y \quad \text{when} \quad \dot{\bar{\epsilon}}^p > 0, \tag{2.221}$$

where

$$Y \overset{\text{def}}{=} Y_{\text{dis}} + Y_{\text{en}} \quad \text{and} \quad Y_{\text{en}} \overset{\text{def}}{=} \pi_{\text{en}}. \tag{2.222}$$

As a simple specific form of the flow resistance Y_{dis} we consider

$$\bar{Y}_{\text{dis}}(\bar{\epsilon}^p, e^p, \vartheta, C_L, C_T) = \bar{Y}_{\text{conv}}(\bar{\epsilon}^p, \vartheta, C_L, C_T) + Z(\bar{\epsilon}^p - e^p) \tag{2.223}$$

such that using (2.220), we may rewrite (2.222) as

$$\bar{Y}(\bar{\epsilon}^p, e^p, \vartheta, C_L, C_T) = \bar{Y}_{\text{conv}}(\bar{\epsilon}^p, \vartheta, C_L, C_T) + Z(\bar{\epsilon}^p - e^p) + B(\bar{\epsilon}^p - e^p) + \frac{\partial \psi_{\text{R}}}{\partial N_T} \frac{dN_T}{d\bar{\epsilon}^p}. \tag{2.224}$$

At this point in time the contribution to the free energy ψ_{R} due to the number of available trapping sites N_T is not well understood. Accordingly, in our theoretical development we do not wish to consider the effect of the last term in (2.224) on the flow resistance of the material and thus neglect it. The flow resistance of the material is then given by

$$\bar{Y}(\bar{\epsilon}^p, e^p, \vartheta, C_L, C_T) = \bar{Y}_{\text{conv}}(\bar{\epsilon}^p, \vartheta, C_L, C_T) + Z(\bar{\epsilon}^p - e^p) + B(\bar{\epsilon}^p - e^p) \tag{2.225}$$

Here $\bar{Y}_{\text{conv}}(\bar{\epsilon}^p, \vartheta, C_L, C_T)$ represents a classical flow resistance which may depend on the equivalent tensile plastic strain $\bar{\epsilon}^p$, the temperature ϑ and the hydrogen concentrations C_L and C_T. The term $Z(\bar{\epsilon}^p - e^p)$ represents a dissipative nonlocal contribution to the flow resistance, with Z a stress-dimensioned material parameter. The form of $\bar{Y}_{\text{conv}}(\bar{\epsilon}^p, \vartheta, C_L, C_T)$ will be specified in later Chapters.

> **Remark:** On physical grounds we require that the stress-dimensioned material parameter $Z > 0$ be much larger than the stress-dimensioned material parameter $B > 0$, so that the dissipative term $Z(\bar{\epsilon}^p - e^p)$ in (2.225) is much greater in magnitude than the energetic term $B(\bar{\epsilon}^p - e^p)$. Although these two terms are mathematically identical, only the dissipative portion will contribute to thermal dissipation due to plastic working through equation (2.178).

2.11.5 Heat flux

From (2.174), we have that the heat flux is given by

$$\mathbf{q}_{\mathrm{R}} = -\kappa \nabla \vartheta, \quad \text{with} \quad \bar{\kappa}(\mathcal{I}_{\mathbf{E}^e}, \bar{\epsilon}^p, \vartheta, C_L, C_T) > 0 \tag{2.226}$$

the thermal conductivity. At this point in time the dependance of the thermal conductivity on the variables $(\mathcal{I}_{\mathbf{E}^e}, \bar{\epsilon}^p, C_L, C_T)$ is not well understood; if one ignores such dependance then $\bar{\kappa}(\vartheta) > 0$ is a temperature-dependent thermal conductivity which is tabulated for many metals.

2.11.6 Lattice hydrogen flux

From (2.175) we have that the lattice hydrogen flux $\mathbf{j}_L$ is given by

$$\mathbf{j}_L = -m_L \nabla \mu_L, \quad \text{with} \quad \bar{m}_L(\mathcal{I}_{\mathbf{E}^e}, \bar{\epsilon}^p, \vartheta, C_L, C_T) > 0 \tag{2.227}$$

the species mobility. Thus, with the chemical potential μ_L given by (2.212),

$$\nabla \mu_L = \frac{R\vartheta}{C_L} \nabla C_L - (3K\beta) \nabla (\operatorname{tr} \mathbf{E}^e) + R \ln \left(\frac{C_L}{N_L} \right) \nabla \vartheta, \tag{2.228}$$

the lattice hydrogen flux is given by

$$\mathbf{j}_L = -m_L \frac{R\vartheta}{C_L} \left(\nabla C_L - \frac{C_L}{R\vartheta} (3K\beta) \nabla (\operatorname{tr} \mathbf{E}^e) + \frac{C_L}{\vartheta} \ln \left(\frac{C_L}{N_L} \right) \nabla \vartheta \right). \tag{2.229}$$

Defining a lattice hydrogen diffusivity D_L by

$$D_L \overset{\text{def}}{=} m_L \frac{R\vartheta}{C_L}, \tag{2.230}$$

the flux (2.229) may then be written as

$$\mathbf{j}_L = -D_L \nabla C_L + \frac{D_L C_L}{R\vartheta}(3K\beta)\nabla(\operatorname{tr}\mathbf{E}^e) - \frac{D_L C_L}{\vartheta}\ln\left(\frac{C_L}{N_L}\right)\nabla\vartheta. \tag{2.231}$$

Similar to the thermal conductivity, the dependance of the mobility m_L on the variables $(\mathcal{I}_{\mathbf{E}^e}, \bar{\epsilon}^p, C_L, C_T)$ is not well understood. In what follows, we adopt the classical approximation that the diffusivity only depends on the temperature through

$$D_L = D_{L0}\exp\left(\frac{-Q}{R\vartheta}\right), \tag{2.232}$$

where D_{L0} is the pre-exponential factor of the diffusivity and Q an activation energy.

2.11.7 Balance of lattice chemical potential μ_L

We may write the local balance equation for the concentration of hydrogen as a local balance equation for the lattice chemical potential. First, the local balance equation for the concentration of hydrogen atoms, reiterated from (2.197), is

$$\dot{C}_L + \dot{C}_T = \operatorname{Div}(m_L \nabla \mu_L) \tag{2.233}$$

Further with $\dot{C}_T$ estimated in (2.211), we obtain the following partial differential equation for $\dot{C}_L$

$$\left(\frac{C_L + C_T(1-\theta_T)}{C_L}\right)\dot{C}_L = \operatorname{Div}(m_L \nabla \mu_L) - \theta_T \frac{dN_T}{d\bar{\epsilon}^p}\dot{\bar{\epsilon}}^p + \frac{C_T(1-\theta_T)W_B}{R\vartheta}\frac{\dot{\vartheta}}{\vartheta}. \tag{2.234}$$

Taking the time rate of change of the constitutive equation for the lattice chemical potential (2.212) yields

$$\dot{\mu}_L = \frac{R\vartheta}{C_L}\dot{C}_L + R\dot{\vartheta}\ln\left(\frac{C_L}{N_L}\right) - 3K\beta\operatorname{tr}\dot{\mathbf{E}}^e. \tag{2.235}$$

Finally, eliminating $\dot{C}_L$ by combining (2.234) and (2.235) yields the following local balance for the lattice hydrogen chemical potential

$$\begin{aligned} D^*\frac{C_L}{R\vartheta}\dot{\mu}_L = {} & \operatorname{Div}(m_L \nabla \mu_L) - D^*\frac{C_L}{R\vartheta}(3K\beta)\operatorname{tr}\dot{\mathbf{E}}^e - \theta_T\frac{dN_T}{d\bar{\epsilon}^p}\dot{\bar{\epsilon}}^p \\ & + \left(D^* C_L \ln\frac{C_L}{N_L} + \frac{C_T(1-\theta_T)W_B}{R\vartheta}\right)\frac{\dot{\vartheta}}{\vartheta} \end{aligned} \tag{2.236}$$

with

$$D^* = 1 + \frac{C_T(1-\theta_T)}{C_L} \quad \text{and} \quad m_L = \frac{D_L C_L}{R\vartheta}. \tag{2.237}$$

Remark: Alternatively, combining (2.234) with (2.228) yields the following local balance equation for the lattice hydrogen concentration

$$\begin{aligned}\left(\frac{C_L + C_T(1-\theta_T)}{C_L}\right)\dot{C}_L &= \mathrm{Div}\,(D_L \nabla C_L) \\ &\quad - \mathrm{Div}\left(\frac{D_L C_L}{R\vartheta}(3K\beta)\nabla(\mathrm{tr}\,\mathbf{E}^e) + \frac{D_L C_L}{\vartheta}\ln\left(\frac{C_L}{N_L}\right)\nabla\vartheta\right) \\ &\quad - \theta_T\frac{dN_T}{d\bar{\epsilon}^p}\dot{\bar{\epsilon}}^p + \frac{C_T(1-\theta_T)W_B}{R\vartheta}\frac{\dot{\vartheta}}{\vartheta}.\end{aligned} \tag{2.238}$$

In application it is advantageous to use the balance equation (2.236) for the lattice chemical potential μ_L rather than the balance equation (2.238) for the lattice hydrogen concentration C_L, since it allows one to prescribe a chemical potential boundary condition. This is discussed in detail in Chapter 3.

2.12 Governing partial differential equations for the specialized constitutive equations. Boundary conditions

The governing partial differential equations consist of:

1. The macroscopic force balance (2.176), viz.

$$\mathrm{Div}\,\mathbf{T}_{\mathrm{R}} + \mathbf{b}_{0\mathrm{R}} = \mathbf{0}, \tag{2.239}$$

   where $\mathbf{T}_{\mathrm{R}} = J\mathbf{T}\mathbf{F}^{-\top}$ is the Piola stress, $\mathbf{T} = J^{-1}\mathbf{R}^e\mathbf{M}^e\mathbf{R}^{e\top}$ is the Cauchy stress, $\mathbf{M}^e$ is the Mandel stress given by $(2.192)_1$, and $\mathbf{b}_{0\mathrm{R}}$ is the body force.

2. The local balance equation for the lattice chemical potential (2.236), viz.

$$\begin{aligned}D^*\frac{C_L}{R\vartheta}\dot{\mu}_L &= \mathrm{Div}\,(m_L\nabla\mu_L) - D^*\frac{C_L}{R\vartheta}(3K\beta)\mathrm{tr}\,\dot{\mathbf{E}}^e - \theta_T\frac{dN_T}{d\bar{\epsilon}^p}\dot{\bar{\epsilon}}^p \\ &\quad + \left(D^*C_L\ln\frac{C_L}{N_L} + \frac{C_T(1-\theta_T)W_B}{R\vartheta}\right)\frac{\dot{\vartheta}}{\vartheta}\end{aligned} \tag{2.240}$$

   with

$$D^* = 1 + \frac{C_T(1-\theta_T)}{C_L} \quad \text{and} \quad m_L = \frac{D_L C_L}{R\vartheta}. \tag{2.241}$$

3. The local balance of energy (2.178), together with equations $(2.192)_4$, (2.196), (2.212), (2.220), and (2.223), yields the following partial differential equation for the temperature

$$\begin{aligned}c\dot{\vartheta} &= \mathrm{Div}\,(\kappa\nabla\vartheta) + q_{\mathrm{R}} + (Y_{\mathrm{conv}} + Z(\bar{\epsilon}^p - e^p))\dot{\bar{\epsilon}}^p + \frac{1}{2}\vartheta\frac{\partial\mathbf{T}^e}{\partial\vartheta} : \dot{\mathbf{C}}^e \\ &\quad + R\vartheta\ln\left(\frac{C_L}{N_L}\right)\dot{C}_L + m_L|\nabla\mu_L|^2 + R\vartheta\ln\left(\frac{\theta_T}{1-\theta_T}\right)\dot{C}_T.\end{aligned} \tag{2.242}$$

4. The microscopic force balance (2.180) together with the constitutive equations (2.215) yields the following partial differential equation for the microscopic variable

$$e^p - l^2 \Delta e^p = \bar{\epsilon}^p, \quad \text{with} \quad l \overset{\text{def}}{=} \sqrt{\gamma / B}, \tag{2.243}$$

where quantity l represents an energetic length parameter in the theory.

We also need initial and boundary conditions to complete the theory. The following are *complementary subsurfaces* of the boundary $\partial \mathrm{B}$ of the body B

$$\begin{array}{lllllll}
\mathcal{S}_1 & \text{and} & \mathcal{S}_2 & \text{with} & \partial \mathrm{B} = \mathcal{S}_1 \cup \mathcal{S}_2 & \text{and} & \mathcal{S}_1 \cap \mathcal{S}_2 = \emptyset, \\
\mathcal{S}_{\mu_L} & \text{and} & \mathcal{S}_{\mathbf{j}_L} & \text{with} & \partial \mathrm{B} = \mathcal{S}_{\mu_L} \cup \mathcal{S}_{\mathbf{j}_L} & \text{and} & \mathcal{S}_{\mu_L} \cap \mathcal{S}_{\mathbf{j}_L} = \emptyset, \\
\mathcal{S}_{\vartheta} & \text{and} & \mathcal{S}_{\mathbf{q}_\mathrm{R}} & \text{with} & \partial \mathrm{B} = \mathcal{S}_{\vartheta} \cup \mathcal{S}_{\mathbf{q}_\mathrm{R}} & \text{and} & \mathcal{S}_{\vartheta} \cap \mathcal{S}_{\mathbf{q}_\mathrm{R}} = \emptyset, \\
\mathcal{S}_{e^p} & \text{and} & \mathcal{S}_{\chi} & \text{with} & \partial \mathrm{B} = \mathcal{S}_{e^p} \cup \mathcal{S}_{\chi} & \text{and} & \mathcal{S}_{e^p} \cap \mathcal{S}_{\chi} = \emptyset.
\end{array}$$

Then for a time interval $t \in [0, T]$ we consider a pair of simple boundary conditions in which the motion is specified on $\mathcal{S}_1$ and the macroscopic surface traction on $\mathcal{S}_2$:

$$\left.\begin{array}{rll}
\boldsymbol{\chi} = \breve{\boldsymbol{\chi}} & \text{on} & \mathcal{S}_1 \times [0, T], \\
\mathbf{T}_\mathrm{R} \mathbf{n}_\mathrm{R} = \breve{\mathbf{t}}_\mathrm{R} & \text{on} & \mathcal{S}_2 \times [0, T];
\end{array}\right\} \tag{2.244}$$

a pair of boundary conditions in which the lattice chemical potential is specified on $\mathcal{S}_{\mu_L}$ and the lattice hydrogen flux on $\mathcal{S}_{\mathbf{j}_L}$

$$\left.\begin{array}{rll}
\mu_L = \breve{\mu}_L & \text{on} & \mathcal{S}_{\mu_L} \times [0, T], \\
-m_L (\nabla \mu_L) \cdot \mathbf{n}_\mathrm{R} = \breve{j}_L & \text{on} & \mathcal{S}_{\mathbf{j}_L} \times [0, T];
\end{array}\right\} \tag{2.245}$$

a pair of boundary conditions in which temperature is specified on $\mathcal{S}_{\vartheta}$ and the heat flux on $\mathcal{S}_{\mathbf{q}_\mathrm{R}}$

$$\left.\begin{array}{rll}
\vartheta = \breve{\vartheta} & \text{on} & \mathcal{S}_{\vartheta} \times [0, T], \\
-\kappa (\nabla \vartheta) \cdot \mathbf{n}_\mathrm{R} = \breve{q}_\mathrm{R} & \text{on} & \mathcal{S}_{\mathbf{q}_\mathrm{R}} \times [0, T];
\end{array}\right\} \tag{2.246}$$

and a final pair of boundary conditions in which the microvariable is specified on $\mathcal{S}_{e^p}$ and the vector microscopic stress on $\mathcal{S}_{\boldsymbol{\xi}}$

$$\left.\begin{array}{rll}
e^p = \breve{e}^p & \text{on} & \mathcal{S}_{e^p} \times [0, T], \\
\gamma (\nabla e^p) \cdot \mathbf{n}_\mathrm{R} = \breve{\chi} & \text{on} & \mathcal{S}_{\chi} \times [0, T];
\end{array}\right\} \tag{2.247}$$

with $\breve{\boldsymbol{\chi}}$, $\breve{\mathbf{t}}_\mathrm{R}$, $\breve{\mu}_L$, $\breve{j}_L$, $\breve{\vartheta}$, $\breve{q}_\mathrm{R}$, $\breve{e}^p$, and $\breve{\chi}$, prescribed functions of $\mathbf{X}$ and t. To these boundary conditions we append the initial conditions

$$\left.\begin{array}{r}
\boldsymbol{\chi}(\mathbf{X}, 0) = \boldsymbol{\chi}_0(\mathbf{X}), \\
\mu_L(\mathbf{X}, 0) = \mu_{L0}(\mathbf{X}), \\
\vartheta(\mathbf{X}, 0) = \vartheta_0(\mathbf{X}), \\
e^p(\mathbf{X}, 0) = e^p_0(\mathbf{X}),
\end{array}\right\} \quad \text{in} \quad \mathrm{B}. \tag{2.248}$$

The coupled set of equations (2.239), (2.240), (2.242), and (2.243), together with equations (2.244) through (2.248), yield an initial boundary-valued problem for the motion $\boldsymbol{\chi}(\mathbf{X},t)$, the lattice chemical potential $\mu_L(\mathbf{X},t)$, the temperature $\vartheta(\mathbf{X},t)$, and the microvariable $e^p(\mathbf{X},t)$.

Remark: Alternatively if one wishes to use the local balance of lattice hydrogen concentration (2.238) instead of the local balance of lattice chemical potential (2.240) to formulate the boundary-valued problem, we define the following *complementary subsurfaces*

$$\mathcal{S}_{C_L} \quad \text{and} \quad \mathcal{S}_{\mathbf{j}_L} \quad \text{with} \quad \partial\mathrm{B} = \mathcal{S}_{C_L} \cup \mathcal{S}_{\mathbf{j}_L} \quad \text{and} \quad \mathcal{S}_{C_L} \cap \mathcal{S}_{\mathbf{j}_L} = \emptyset,$$

and the boundary conditions (2.245) are replaced by a pair of boundary conditions in which the lattice hydrogen concentration is specified on $\mathcal{S}_{C_L}$ and the lattice hydrogen flux on $\mathcal{S}_{\mathbf{j}_L}$

$$\left.\begin{aligned} C_L &= \breve{C}_L \quad \text{on} \quad \mathcal{S}_{C_L} \times [0,T], \\ \mathbf{j}_L \cdot \mathbf{n}_\mathrm{R} &= \breve{j}_L \quad \text{on} \quad \mathcal{S}_{\mathbf{j}_L} \times [0,T]; \end{aligned}\right\} \tag{2.249}$$

with $\breve{C}_L$, and $\breve{j}_L$ prescribed functions of $\mathbf{X}$ and t, and initial condition

$$C_L(\mathbf{X},0) = C_{L0}(\mathbf{X}) \quad \text{in} \quad \mathrm{B}. \tag{2.250}$$

2.13 Numerical implementation

We have implemented our theory in the commercial finite element software ABAQUS/Standard (2011) through a user element subroutine (UEL) by writing four-noded isoparameteric quadrilateral plane-strain (UPE4) and axisymmetric (UAX4) user-elements which couple mechanical deformation, hydrogen diffusion, heat conduction, and strain-gradient regularization. Details of the numerical implementation are provided in Appendix B. In our numerical implementation we neglect body forces and an external heat supply.

For the implementation of hydrogen diffusion **we have chosen the lattice chemical potential as our solution variable** and equation (2.240) as our balance equation for lattice chemical potential. This choice is made for two reasons. First, it is easier to compute the balance equation for the lattice chemical potential (2.240) since it does not require computing gradients of the trace of the strain tensor ($\nabla \mathrm{tr}\,\mathbf{E}^e$) or gradients of the temperature ($\nabla\vartheta$) which are required by the balance equation for the lattice hydrogen concentration (2.238). Secondly, it has important consequences in the manner in which boundary conditions are prescribed, this will be discussed in detail in Chapter 3.

Although in this Chapter we have developed a thermodynamically-consistent theory which is not restricted to isothermal conditions, in the numerical simulations performed in this work we have **restricted ourselves to isothermal conditions**. We will consider non-isothermal simulations in future work.

2.14 Concluding remarks

In this Chapter we have developed a reasonably general thermodynamically-consistent theoretical framework for modeling the coupled problem of diffusion of hydrogen, trapping of hydrogen, diffusion of heat, and large elastic-plastic deformation of metals. We have specialized our theory with a set of constitutive equations which should be useful in application. We have placed the widely-used notion of an "equilibrium" between hydrogen residing in normal interstitial lattice sites and hydrogen trapped at microstructural effects of Oriani (1970), within a concise thermodynamic framework. Furthermore, our theory is not derived based on Oriani's hypothesis, rather through thermodynamically-consistent constitutive choices, we recover his argument as a special case of our theory. Our theory is thus not restricted to modeling hydrogen trapping through the use of Oriani's hypothesis.

Chapter 3

Hydrogen transport near a blunting crack tip

3.1 Introduction

In this chapter we numerically study the problem of hydrogen transport near a blunting crack tip. Our purpose here is to compare results from our numerical simulations with the classical results of Sofronis and McMeeking (1989) and Krom et al. (1999), and illustrate the effect of using a lattice *chemical potential* boundary condition as opposed to the lattice *hydrogen concentration* boundary condition used by these authors.

3.2 Chemical potential boundary condition

In order to model the experimentally relevant boundary condition of a host metal exposed to a hydrogen atmosphere at a given partial pressure p_{H_2} and temperature ϑ, we must consider the equilibrium between the atomic hydrogen in the metal and hydrogen molecules in the gas (cf. e.g. San Marchi et al., 2007 and Krom et al., 1997). At equilibrium, the chemical potential of dissolved hydrogen in the solid must equal the chemical potential of the gas, that is

$$\mu_{\underline{\mathrm{H}}} = \frac{1}{2}\mu_{\mathrm{H}_2}, \tag{3.1}$$

where $\underline{\mathrm{H}}$ denotes the atomic hydrogen dissolved in the solid. The chemical potential of the hydrogen molecules in the gas may be expressed as

$$\mu_{\mathrm{H}_2} = \mu^0_{\mathrm{H}_2} + R\vartheta \ln\left(\frac{f_{\mathrm{H}_2}}{p^0}\right), \tag{3.2}$$

where f_{H_2} is the *fugacity* of the hydrogen molecules in the gas mixture, and p^0 is a reference pressure.

Accordingly, we assume that on the boundary of interest the lattice chemical potential must be equal to the chemical potential of dissolved hydrogen in the solid, then using (3.1) and (3.2)

$$\breve{\mu}_L = \frac{1}{2}\mu_{H_2} = \frac{1}{2}\left(\mu^0_{H_2} + R\vartheta \ln\left(\frac{f_{H_2}}{p^0}\right)\right), \tag{3.3}$$

where $\breve{\mu}_L$ denotes the prescribed lattice chemical potential on the boundary.

The *reference state* of the element hydrogen (at 298 K and 1 bar) is the a gas of H_2 molecules, and the chemical potential of an element in its reference state is zero (cf. Arkins and de Paula (2010), pp. 119,159):

$$\mu^0_{H_2} = 0 \quad \text{at} \quad p_{H_2} = 0.101\,\text{MPa}, \quad \text{and} \quad \vartheta = 298\,\text{K}. \tag{3.4}$$

Using (3.4) in (3.3), the prescribed lattice chemical potential may be further simplified to

$$\breve{\mu}_L = R\vartheta \ln\left(\sqrt{\frac{f_{H_2}}{p^0}}\right). \tag{3.5}$$

Equating the constitutive equation for the lattice chemical potential (2.212), for an unstrained lattice ($\operatorname{tr}\mathbf{E}^e = 0$), with (3.5) yields

$$\mu^0_L + R\vartheta \ln\left(\frac{C_L}{N_L}\right) = R\vartheta \ln\left(\sqrt{\frac{f_{H_2}}{p^0}}\right). \tag{3.6}$$

This may be simplified to [1]

$$C_L = K\sqrt{f_{H_2}}, \tag{3.7}$$

with the *solubility* K given by

$$K = K_0 \exp\left(\frac{-\Delta H}{R\vartheta}\right), \tag{3.8}$$

where

$$K_0 = \frac{N_L}{\sqrt{p^0}}, \quad \text{and} \quad \Delta H = \mu^0_L, \tag{3.9}$$

are experimentally measurable constants.

The solubility K in (3.7) is typically obtained from *experiments* under conditions in which the lattice is unstrained ($\operatorname{tr}\mathbf{E}^e = 0$). The experimental data is fit to an Arrhenius relation of the form shown in (3.8), from where the pre-exponential coefficient K_0 and the energetic term ΔH are experimentally determined (cf. San Marchi et al., 2007).

---

[1] For an ideal gas, $f_{H_2} = p_{H_2}$ and (3.6) reduces to

$$C_L = K\sqrt{p_{H_2}}$$

which is Sieverts' law.

With K_0 and ΔH determined experimentally, and N_L known for a given crystal lattice, the prescribed lattice chemical potential is given by (cf., eq. (3.5))

$$\breve{\mu}_L = R\vartheta \ln\left(\sqrt{\frac{f_{\mathrm{H}_2}}{p^0}}\right), \quad \text{with} \quad p^0 = \left(\frac{N_L}{K_0}\right)^2, \tag{3.10}$$

and the reference lattice chemical potential is given by

$$\mu_L^0 = \Delta H. \tag{3.11}$$

The fugacity f_{H_2} of the hydrogen molecules in the gas depends on the equation of state of hydrogen. If this equation of state is taken in the simple Able-Noble form (cf. e.g., San Marchi et al., 2007), then

$$f_{\mathrm{H}_2} = p_{\mathrm{H}_2} \exp\left(\frac{p_{\mathrm{H}_2} b}{R\vartheta}\right), \tag{3.12}$$

where b is an experimentally measurable constant. Finally, using (3.12) in (3.10) the prescribed lattice chemical potential is given by

$$\breve{\mu}_L = R\vartheta \ln\left(\sqrt{\frac{p_{\mathrm{H}_2}}{p^0} \exp\left(\frac{p_{\mathrm{H}_2} b}{R\vartheta}\right)}\right) \quad \text{with} \quad p^0 = \left(\frac{N_L}{K_0}\right)^2. \tag{3.13}$$

Remark: If the chemical potential of the gas is constant (that is the hydrogen atmosphere in contact with the boundary of interest does not change), the equilibrium relation (3.1) together with $\breve{\mu}_L = \mu_{\underline{\mathrm{H}}}$ and the constitutive equation for lattice chemical potential (2.212) yields

$$\mu_L^0 + R\vartheta \ln\left(\frac{C_L}{N_L}\right) - (3K\beta)\mathrm{tr}\,\mathbf{E}^e = \frac{1}{2}\mu_{\mathrm{H}_2} = \mathbf{constant}. \tag{3.14}$$

Since the volumetric elastic strains $\mathrm{tr}\,\mathbf{E}^e$ in (3.14) may change during the deformation of the host metal, **the lattice hydrogen concentration C_L on the specimen surface is not constant**. Thus, in order to model the important boundary of a host metal exposed to a hydrogen atmosphere at a constant partial pressure p_{H_2} and constant temperature ϑ we must prescribe a **constant lattice chemical potential**, as in (3.13), and not a constant lattice hydrogen concentration $\breve{C}_L$, as in (2.249), and as has been done previously in Sofronis and McMeeking (1989) and Krom et al. (1999).

3.3 Effect of the chemical potential boundary condition on hydrogen transport near a blunting crack tip

In order to illustrate the effects of using the lattice chemical potential as a solution variable and applying a lattice chemical potential boundary condition, we consider the problem of hydrogen transport near a blunting crack tip and compare our results to the classical results of Krom et al. (1999) and Sofronis and McMeeking (1989).

The mesh used is approximately the same as that of Krom et al. (1999), a schematic of which is shown in Figure 3-1. It consists of 3028 four-noded plane-strain elements. The initial crack tip opening displacement b_0 is 10 μm. The radius of the semi-circular domain is $15,000\,b_0$.

In order to compare our simulation results to those published in the literature, in this section we use the plastic flow resistance employed by Krom et al. (1999), where

$$Y = Y_0\left(\frac{\bar{\epsilon}^p}{\epsilon_0}+1\right)^n \quad \text{and} \quad \epsilon_0 = \frac{Y_0}{E}. \tag{3.15}$$

The Young's modulus E is 207 GPa, the Poisson's ratio ν is 0.3, the yield stress Y_0 is 250 MPa, and the hardening exponent n is 0.2. Also, in these simulations we do not include strain gradient effects and thus set

$$Z = 0, \quad \text{and} \quad B = 0.$$

The lattice diffusion coefficient D_L is taken to be constant and equal to $1.27 \times 10^{-8}\,\mathrm{m^2/s}$. The temperature of the system is held constant at 300 K. Further, in accordance with Krom et al. (1999), the number of lattice sites N_L is $8.47 \times 10^5\,\mathrm{mol/m^3}$, and the number of trap sites N_T is assumed to increase with an increase in the equivalent plastic strain $\bar{\epsilon}^p$ according to

$$\log N_T = 23.26 - 2.33\exp(-5.5\bar{\epsilon}^p). \tag{3.16}$$

On the symmetry axis we prescribe zero lattice hydrogen flux, and zero displacements in the y-direction. On the crack face and the circular boundary we either prescribe a constant lattice chemical potential $\breve{\mu}_L$ or a zero lattice hydrogen flux. The initial lattice chemical potential is μ_{L0}. Both $\breve{\mu}_L$ and μ_{L0} are computed using (3.13) with $p_{\mathrm{H}_2} = 0.101\,\mathrm{MPa}$, $\vartheta = 300\,\mathrm{K}$, $b = 0$,[2] $K_0 = 1040\,\mathrm{mol/(m^3\sqrt{MPa})}$, and $N_L = 8.46 \times 10^5\,\mathrm{mol/m^3}$, and are equal to

$$\breve{\mu}_L = \mu_{L0} = -19.576\,\mathrm{kJ/mol}. \tag{3.17}$$

The corresponding initial lattice hydrogen concentration may be computed from Sieverts' law, (3.7) with $f_{\mathrm{H}_2} = p_{\mathrm{H}_2}$, and is equal to $C_{L0} = 3.46 \times 10^{-3}\,\mathrm{mol/m^3}$ which is the same initial concentration used in Krom et al. (1999).

The displacements along the circular boundary are prescribed according to the mode-I elastic solution and an imposed value of K_I. A stress intensity factor of $K_\mathrm{I} = 89.2\,\mathrm{MPa}\sqrt{\mathrm{m}}$ is applied at a constant rate $\dot{K}_\mathrm{I} = K_\mathrm{I}/t_f$ where t_f is the time to load, which is varied between simulations. After loading ($t > t_f$) the load is kept constant.

Note that the quantities shown in all Figures in this Chapter are computed and plotted in the undeformed configuration as was done in Sofronis and McMeeking (1989) and Krom et al. (1999).

---

[2] In Sofronis and McMeeking (1989) the authors do not consider deviations from ideal gas behavior, thus $b = 0$.

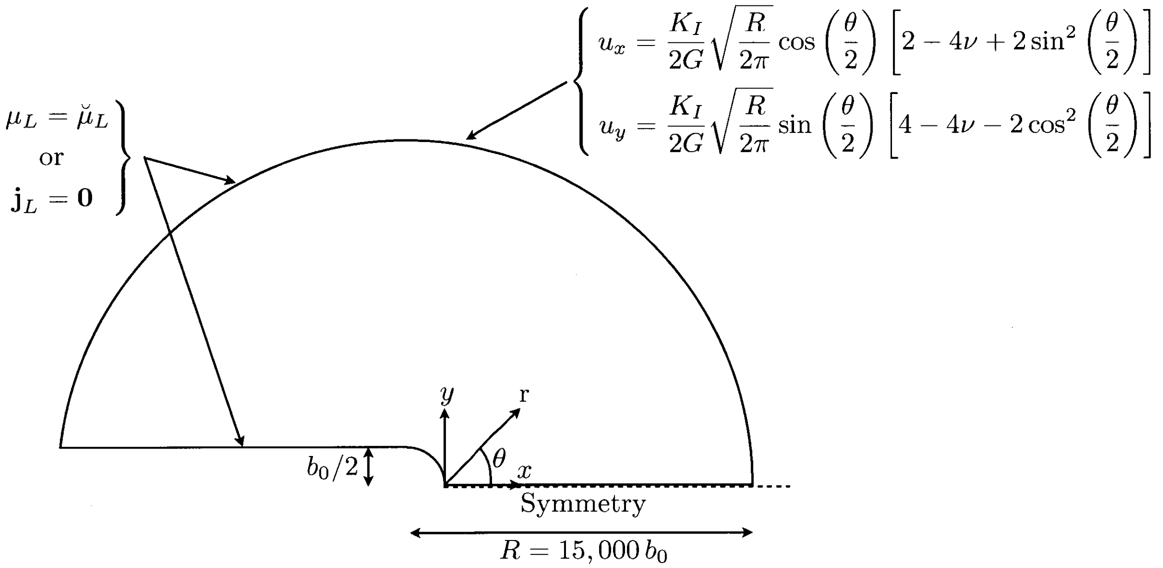

Figure 3-1: Schematic of the blunt-crack geometry and boundary conditions. On the outer surface and the crack face we either prescribe a constant lattice chemical potential $\breve{\mu}_L$ or a zero lattice hydrogen flux $\mathbf{j}_L = \mathbf{0}$. b_0 is the initial crack opening displacement.

3.3.1 Results using a constant chemical potential boundary condition

In the following simulations we impose a constant lattice chemical potential $\breve{\mu}_L$ at the crack face and on the circular boundary. Fig. 3-2(a) shows the hydrostatic stress $\sigma_h = (1/3)\mathrm{tr}\,\mathbf{T}$ normalized by the yield strength Y_0, ahead of the crack tip ($\theta = 0°$) at the end of loading for a load time of $t_f = 130\,\mathrm{s}$, the results of this study (solid line) are compared to those of Krom et al. (1999) Fig. 2 (▲ symbols). For later use Fig. 3-2(a) also shows the volumetric elastic strain $\mathrm{tr}\,\mathbf{E}^e$ normalized by the yield strain ϵ_0, ahead of the crack tip at the end of loading for a load time of $t_f = 130\,\mathrm{s}$ (dashed line).

Fig. 3-2(b) shows the equivalent tensile plastic strain $\bar{\epsilon}^p$, ahead of the crack tip at the end of loading for a load time of $t_f = 130\,\mathrm{s}$, the results of this study (solid line) are compared to those of Sofronis and McMeeking (1989) Fig. 4 (▲ symbols). The results of Fig. 3-2 are essentially identical to those of Krom et al. (1999) and Sofronis and McMeeking (1989), and this validates our finite-element implementation.

Fig. 3-3 shows the lattice hydrogen concentration C_L normalized by the initial lattice hydrogen concentration C_{L0}, ahead of the crack tip at $t = 130\,\mathrm{s}$ and $t = 1419\,\mathrm{h}$, for a load time of $t_f = 130\,\mathrm{s}$. The results of this study (solid lines) are compared to the results of Krom et al. (1999) Fig. 6 (dashed lines). As noted by Sofronis and McMeeking (1989), integrating equation (2.229) along a path ahead of the crack tip ($\theta = 0°$) for $\mathbf{j}_L = \mathbf{0}$, and under isothermal conditions, we obtain the normalized steady state lattice hydrogen concentration concentration, along the same path, in a stressed lattice as

$$\frac{C_{L,\mathrm{SS}}}{C_{L0}} = \exp\left(\frac{3K\beta}{R\vartheta}\mathrm{tr}\,\mathbf{E}^e\right), \tag{3.18}$$

where C_{L0} is the initial lattice hydrogen concentration. This normalized steady state concentration is computed using the data shown in Fig. 3-2(a) and is plotted in Fig. 3-3 (▲ symbols).

As is clear from Fig. 3-3, *the results obtained with a constant lattice chemical potential boundary condition differ significantly from those obtained by Krom et al. (1999) using a constant lattice hydrogen concentration boundary condition.* Due to the hydrostatic stresses at the notch tip there is an increase in C_L at the notch tip, in our simulations which use a lattice chemical potential boundary condition. Furthermore, our lattice hydrogen distribution (solid lines) matches well with the steady-state concentration predicted by equation (3.18) (▲ symbols), whereas previous simulations which use a prescribed lattice hydrogen concentration are unable to do so (dashed lines).

In our implementation using the lattice chemical potential as our solution variable, steady-state equilibrium is achieved when the chemical potential within the body is in equilibrium with the chemical potential of the hydrogen gas surrounding the body. Fig. 3-4 shows the lattice chemical potential ahead of the crack tip at different times for a load time of $t_f = 130\,\mathrm{s}$, equilibrium is reached within 500 hours after the load is applied.

Fig. 3-5 shows the normalized lattice hydrogen distribution ahead of the crack tip at the end of loading ($t = t_f$) for different loading times. The results of this study (solid lines) are compared to those of Krom et al. (1999) Fig. 6 (dashed lines) for the same loading times. As can be seen in Fig. 3-5, due to the constant chemical potential boundary condition there is a *higher demand* for lattice hydrogen at the notch tip in our simulations (solid lines) when compared to those of Krom et al. (1999) (dashed lines). At higher loading rates, hydrogen is depleted from lattice sites due to trapping, and diffusion of lattice hydrogen does not have enough time to resupply the regions near the notch tip where trapping is highest due to plasticity. Fig. 3-5 shows that the depletion of lattice hydrogen near the notch is greater in our simulations (solid lines) than in those of Krom et al. (1999) (dashed lines) due to the enhanced demand for lattice hydrogen at the tip from the presence of the hydrostatic stresses and the use of a constant chemical potential boundary condition.

The trapped hydrogen concentration C_T normalized by the initial trapped hydrogen concentration C_{T0}, ahead of the crack tip at the end of loading ($t = t_f$) for different loading times is shown in Fig. 3-6(a), the results of this study (solid lines) are compared to those of Krom et al. (1999) Fig. 7 (dashed lines). The trapped hydrogen distribution is not affected by the loading rate except at the fastest load time of $t_f = 1.3\,\mathrm{s}$. At this load time the lattice hydrogen is completely depleted and is still not sufficient to saturate all trapping sites. As discussed before, there is *enhanced hydrogen depletion* in our simulations, and thus the region over which the hydrogen traps are unsaturated is larger in our simulations (solid lines) when compared to those of Krom et al. (1999) (dashed lines).

The unsaturation of hydrogen traps, due lattice hydrogen depletion at faster loading rates, is better visualized by plotting the site fraction of trapped hydrogen θ_T as shown in Fig. 3-6(b). From Fig. 3-6(b) we see that at a load time of $t_f = 3.25\,\mathrm{s}$ there is also insufficient lattice hydrogen to fully supply and saturate all available traps.

We have illustrated in this section the manner in which the use of a constant lattice chemical potential boundary condition can affect the hydrogen distribution near a blunt-crack. This in turn will affect any theory which seeks to couple the material response of a system with the hydrogen distribution within it.

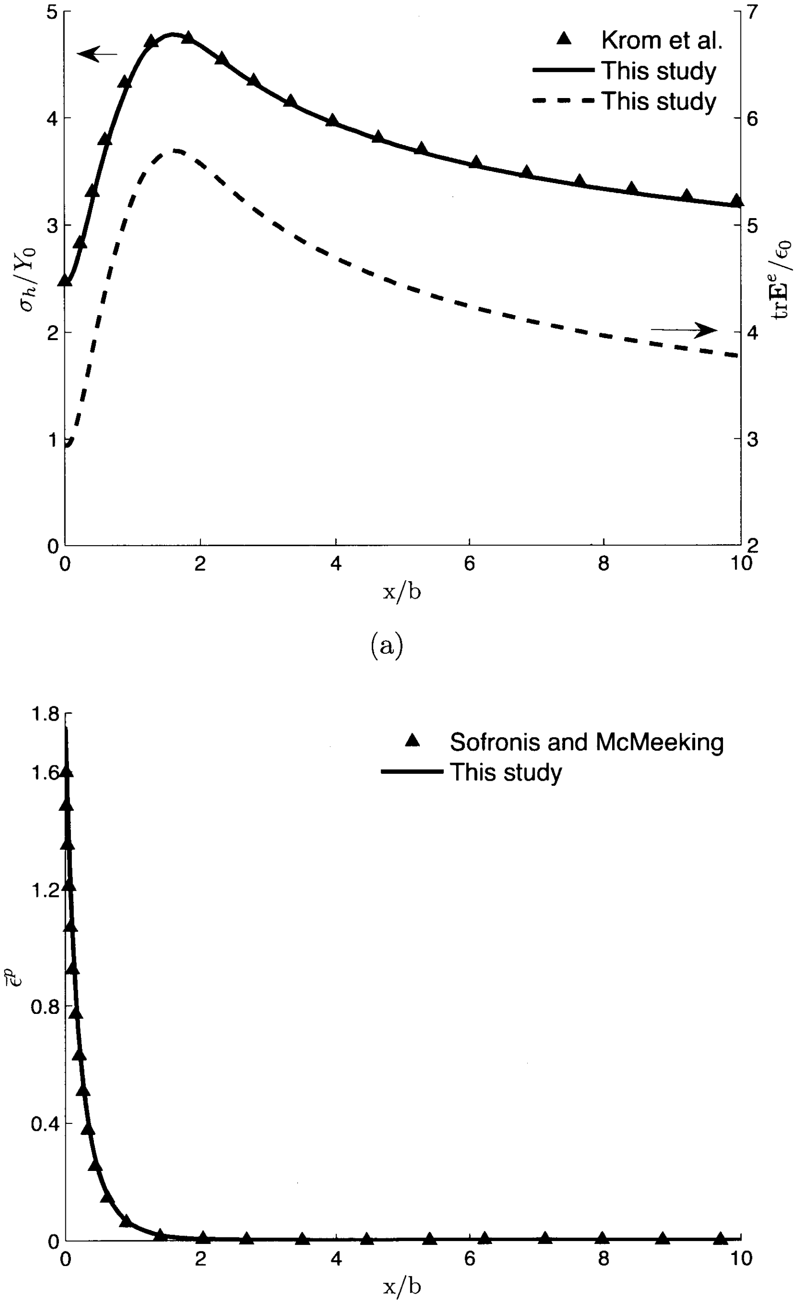

(a)

(b)

Figure 3-2: (a) Normalized hydrostatic stress σ_h/Y_0 (left scale) and normalized volumetric elastic strain $\mathrm{tr}\mathbf{E}^e/\epsilon_0$ (right scale), ahead of the crack tip ($\theta = 0°$) at $t = t_f = 130\,\mathrm{s}$ compared to the result of Krom et al. (1999) Fig. 2. (b) Equivalent tensile plastic strain $\bar{\epsilon}^p$ ahead of the crack tip ($\theta = 0°$) at $t = t_f = 130\,\mathrm{s}$ compared with the result of Sofronis and McMeeking (1989) Fig 4. Y_0 is the yield stress, ϵ_0 is the yield strain, and $b = 4.7b_0$ is the deformed crack tip opening displacement.

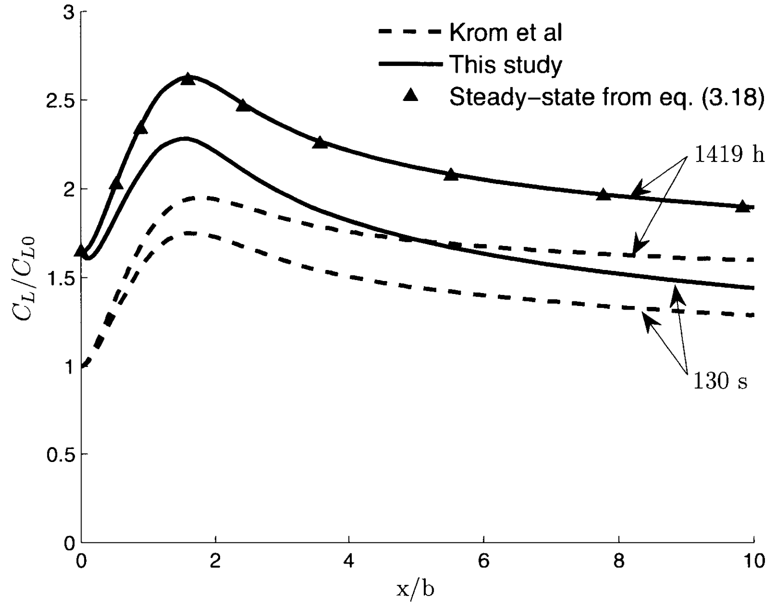

Figure 3-3: Normalized lattice hydrogen concentration C_L/C_{L0} ahead of the crack tip ($\theta = 0°$) at $t = 130\,\mathrm{s}$ and $t = 1419\,\mathrm{h}$ for a load time of $t_f = 130\,\mathrm{s}$ compared to the results of Krom et al. (1999) Fig. 3 and to eq. (3.18). C_{L0} is the initial lattice hydrogen concentration and $b = 4.7b_0$ is the deformed crack tip opening displacement.

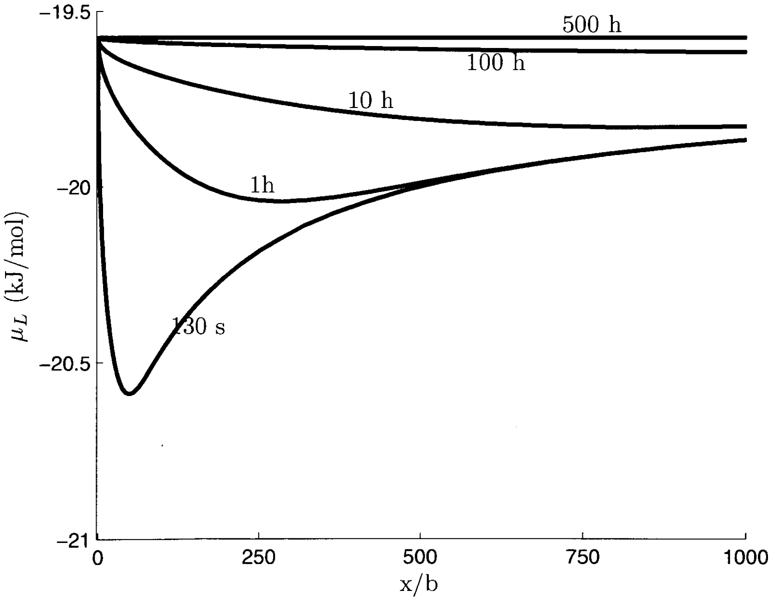

Figure 3-4: Lattice chemical potential μ_L ahead of the crack tip ($\theta = 0°$) at different times for a load time of $t_f = 130\,\mathrm{s}$. $b = 4.7b_0$ is the deformed crack tip opening displacement.

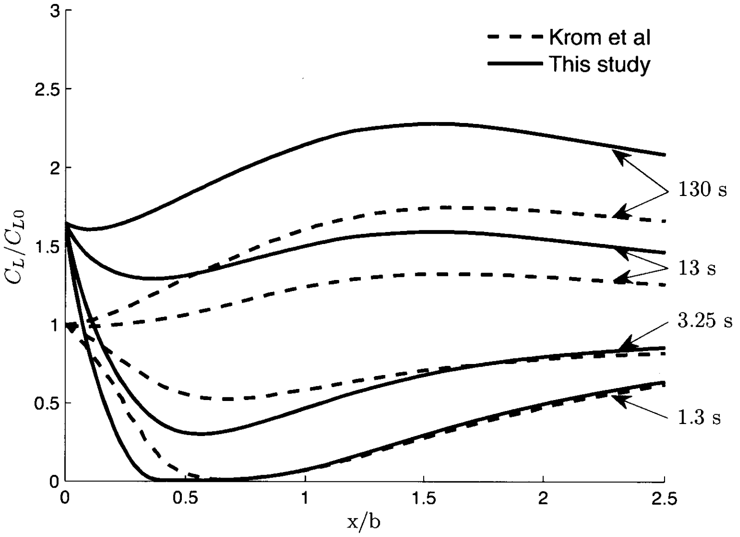

Figure 3-5: Normalized lattice hydrogen concentration C_L/C_{L0} ahead of the crack tip ($\theta = 0°$) at the end of loading ($t = t_f$) for different load times compared to the results of Krom et al. (1999) Fig. 6 for the same load times. C_{L0} is the initial lattice hydrogen concentration and $b = 4.7b_0$ is the deformed crack tip opening displacement.

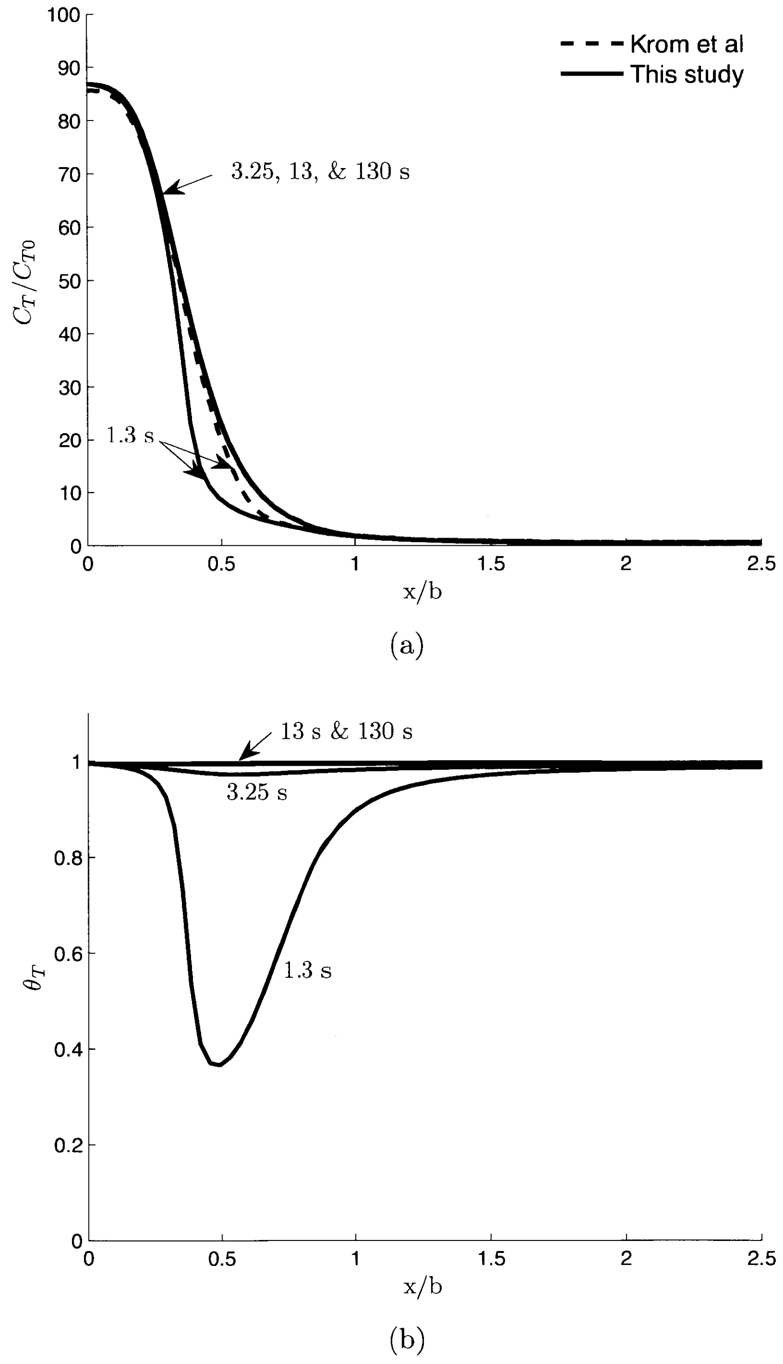

(a)

(b)

Figure 3-6: (a) Normalized trapped hydrogen concentration C_T/C_{T0} ahead of the crack tip ($\theta = 0°$) at the end of loading ($t = t_f$) for different load times compared to the results of Krom et al. (1999) Fig. 7 for the same load times. (b) Site fraction of trapped hydrogen θ_T ahead of the crack tip ($\theta = 0°$) after loading for different load times. C_{T0} is the initial trapped hydrogen concentration and $b = 4.7b_0$ is the deformed crack tip opening displacement.

3.3.2 Results using a zero flux boundary condition

In the following simulations we impose a zero lattice hydrogen flux $\mathbf{j}_L = \mathbf{0}$ at the crack face and on the circular boundary. This boundary condition is equivalent to the one used in Krom et al. (1999). Fig. 3-7 shows the normalized lattice hydrogen distribution ahead of the crack tip ($\theta = 0°$) at the end of loading for different loading times, and at $t = 1419\,\mathrm{h}$ for a load time of $t_f = 130\,\mathrm{s}$. The results of this study (solid lines) are compared to those of Krom et al. (1999) Fig. 8 (dashed lines) and are *essentially identical.*

As shown in Fig. 3-8, steady-state is achieved within 500 hours after loading when the lattice chemical potential within the body equilibrates. The evolution of the lattice chemical potential from the end of loading to 500 hours of hold time is quite different in the case of a prescribed lattice chemical potential boundary condition, Fig. 3-4, and the case of a zero lattice hydrogen flux boundary condition, Fig. 3-8. In the case of a prescribed constant lattice chemical potential boundary condition, equilibrium occurs when the lattice chemical potential of the host metal equilibrates with the prescribed lattice chemical potential. In the case of a prescribed zero hydrogen flux boundary condition, equilibrium occurs when the lattice chemical potential within the body equilibrates to a new value. Due to the use of the lattice chemical potential as a solution variable in our finite-element implementation we can accurately predict when the hydrogen concentration has achieved steady-state.

Fig. 3-9(a) shows the normalized trapped hydrogen distribution ahead of the crack tip at the end of loading ($t = t_f$) for different load times. The results of this study (solid lines) are compared to those of Krom et al. (1999) Fig. 9 (dashed lines). There is a small discrepancy in the normalized trapped hydrogen concentration at the crack tip for the simulation with a loading time of $t_f = 1.3\,\mathrm{s}$, this is attributed to small difference in the equivalent tensile plastic strain at the tip caused by differences in meshing. As shown in Fig. 3-9(b), at higher loading rates there is insufficient lattice hydrogen available to saturate all the available traps. As expected, the area over which the trapping sites are unsaturated is larger with the use of the zero flux boundary condition than with the use of a constant lattice chemical potential boundary condition.

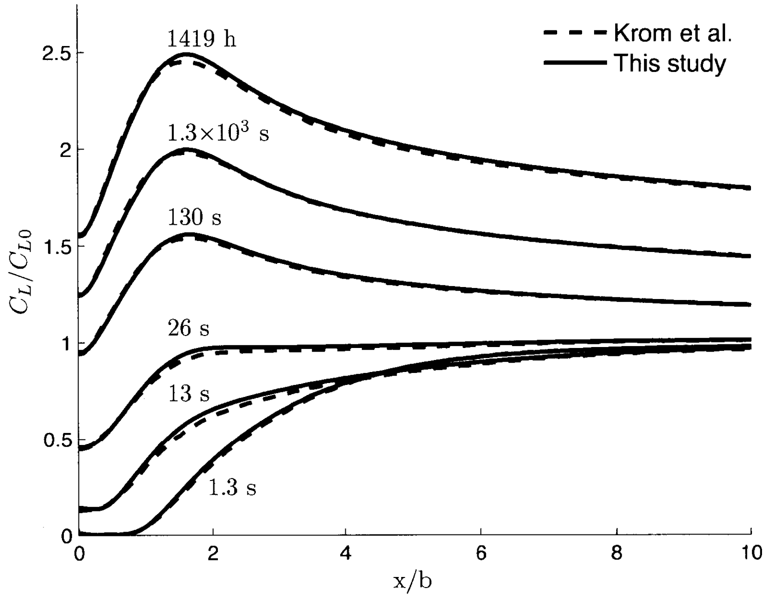

Figure 3-7: Normalized lattice hydrogen concentration C_L/C_{L0} ahead of the crack tip ($\theta = 0°$) after loading ($t = t_f$) for different load times and at $t = 1419\,\text{h}$ for a load time of $t_f = 130\,\text{s}$, compared to the results of Krom et al. (1999) Fig. 8 for the same load times. C_{L0} is the initial lattice hydrogen concentration and $b = 4.7b_0$ is the deformed crack tip opening displacement.

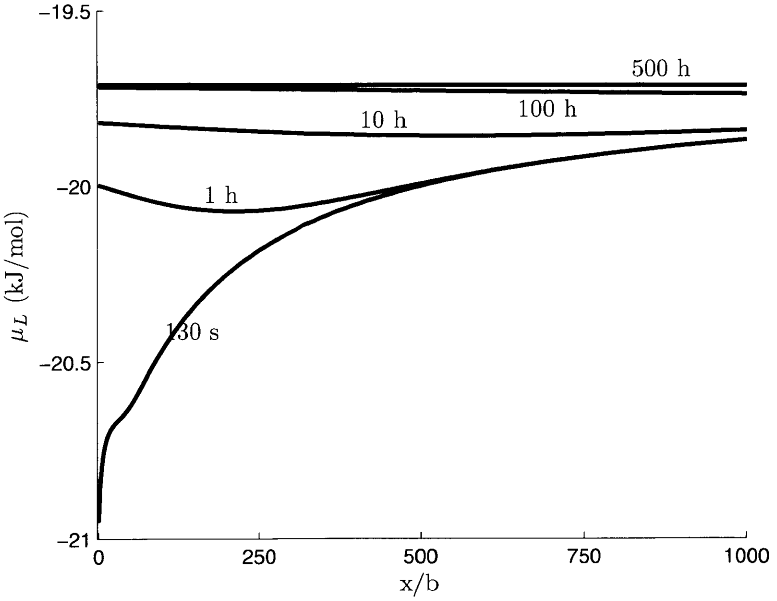

Figure 3-8: Lattice chemical potential μ_L ahead of the crack tip ($\theta = 0°$) at different times for a load time of $t_f = 130\,\text{s}$. $b = 4.7b_0$ is the deformed crack tip opening displacement.

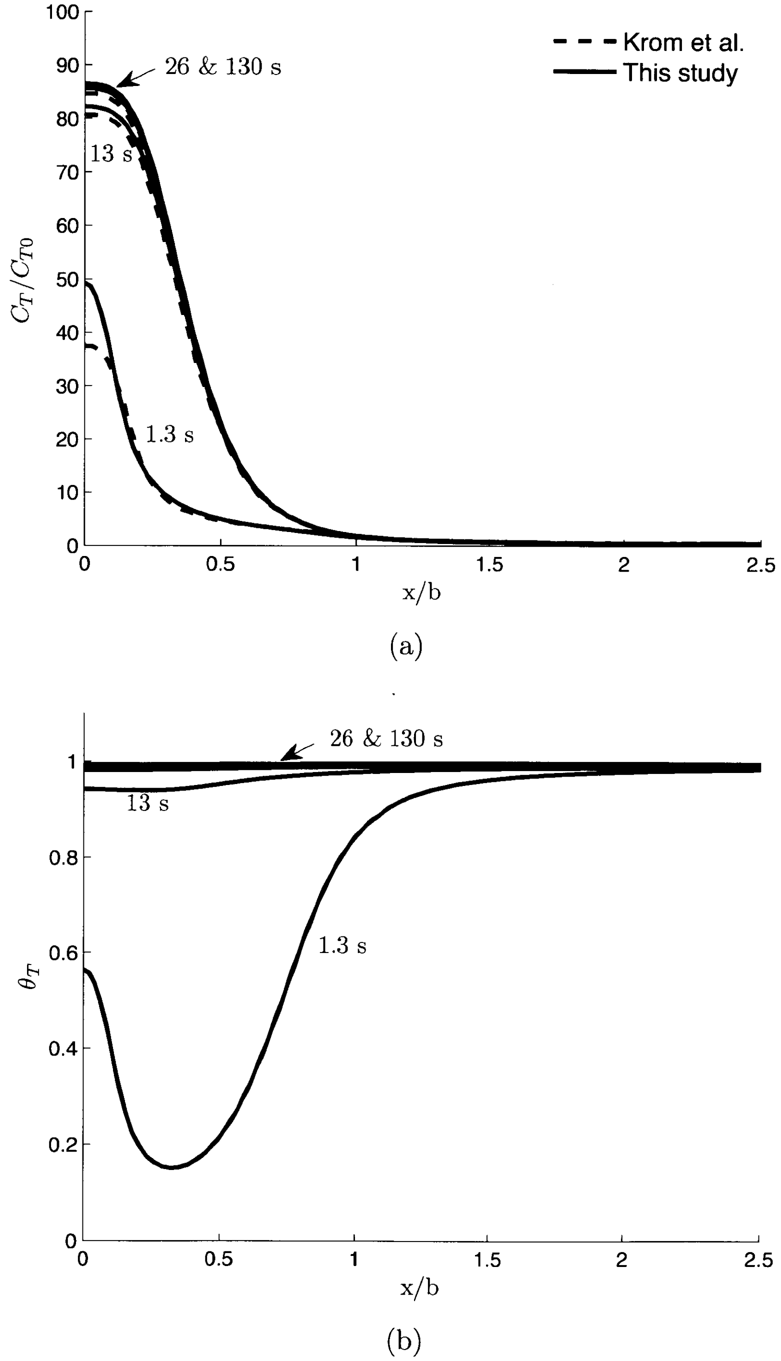

(a)

(b)

Figure 3-9: (a) Normalized trapped hydrogen concentration C_T/C_{T0} ahead of the crack tip ($\theta = 0°$) at the end of loading ($t = t_f$) for different load times, compared to the results of Krom et al. (1999) Fig. 9 for the same load times. (b) Site fraction of trapped hydrogen θ_T ahead of the crack tip at the end of loading for different load times. C_{T0} is the initial trapped hydrogen concentration and $b = 4.7b_0$ is the deformed crack tip opening displacement.

3.4 Concluding remarks

In this Chapter we have numerically studied the problem of hydrogen transport near a blunting crack tip. We have shown that our numerical simulations predict the same deformation response as the simulations of Sofronis and McMeeking (1989) and Krom et al. (1999). For the case in which we prescribe a zero flux boundary condition at the crack face and on the circular boundary of our domain, our simulations also predict essentially the same distribution of lattice and trapped hydrogen concentrations ahead of the crack tip as the simulations of Krom et al. (1999). This serves as partial validation that our numerical implementation is correct.

More importantly we have shown the effect of using a constant lattice chemical potential, as oppose to a constant lattice hydrogen concentration, as a boundary condition. Our simulations, using the lattice chemical potential boundary condition, predict higher lattice hydrogen concentrations at the blunt crack tip due to the effect of the tensile volumetric strains at the same location. Our steady-state lattice hydrogen concentration values agree well with the analytical prediction (3.18), whereas the simulations of Sofronis and McMeeking (1989) and Krom et al. (1999) do not agree due to the enforcement of a constant lattice hydrogen concentration at the boundary. Finally, at high loading rates, our simulations predict larger regions in which the lattice hydrogen is entirely depleted to satisfy the available trapping sites.

All of the aforementioned differences between our simulations and those of Sofronis and McMeeking (1989) and Krom et al. (1999) are crucial if one is to construct a theory, and corresponding numerical capability, to model the manner in which the mechanical behavior of a system is affected by the hydrogen concentration within it.

Chapter 4

Effects of hydrogen on the plastic deformation of metals

4.1 Introduction

In this chapter we numerically study the effect of hydrogen on the *isothermal* plastic deformation of metals. We first consider the effect of hydrogen on the plane-strain tensile deformation of a metal specimen, and then we consider the effect of hydrogen on three-point bending of a U-notched metal specimen. The results from the three-point bending simulations are qualitatively compared to the results of Lee et al. (1979) in which the authors studied the same phenomenon experimentally.

Recall from equation (2.225) that the plastic flow resistance is given by

$$\bar{Y}(\bar{\epsilon}^p, \mathrm{e}^p, \vartheta, C_L, C_T) = \bar{Y}_{\mathrm{conv}}(\bar{\epsilon}^p, \vartheta, C_L, C_T) + Z(\bar{\epsilon}^p - \mathrm{e}^p) + B(\bar{\epsilon}^p - \mathrm{e}^p). \tag{4.1}$$

In keeping with the isothermal nature of our simulations, in this Chapter we consider a conventional flow resistance $\bar{Y}_{\mathrm{conv}}(\bar{\epsilon}^p, C_L, C_T)$ which does not depend on the temperature ϑ and which obeys an evolution equation of the form

$$\dot{Y}_{\mathrm{conv}} = \begin{cases} H_{\mathrm{hard}}\left(1 - \dfrac{Y_{\mathrm{conv}}}{Y_{\mathrm{sat}}}\right)\dot{\bar{\epsilon}}^p & \text{if} \quad C < C_c, \\[2ex] H_{\mathrm{hard}}\left(1 - \dfrac{Y_{\mathrm{conv}}}{Y_{\mathrm{sat}}}\right)\dot{\bar{\epsilon}}^p - H_{\mathrm{soft}}\dot{\bar{\epsilon}}^p & \text{if} \quad C \geq C_c, \end{cases} \tag{4.2}$$

where

$$C \overset{\mathrm{def}}{=} C_L + C_T, \tag{4.3}$$

and subject to the initial condition

$$\bar{Y}_{\mathrm{conv}}(0, C_{L0}, C_{T0}) = Y_0. \tag{4.4}$$

Here, Y_0 is the initial flow resistance, C_{L0} and C_{T0} are the initial lattice and trapped hydrogen concentrations, H_{hard} is a reference strain-hardening rate, Y_{sat} is a saturation value for the plastic hardening. Also, H_{soft} is a hydrogen triggered strain-softening rate, and C_c is the critical total hydrogen concentration at which the material begins to soften. In summary, with the form of Y_{conv} chosen the material will harden if the total hydrogen concentration C is below the critical concentration C_c and will soften if the total hydrogen concentration C is above the critical concentration C_c. We view this as a continuum-level description of the decrease in flow resistance due to an increase in the hydrogen concentration and is meant to account for the hydrogen-enhanced localized plasticity micromechanism.

We also introduce a positive-valued material parameter

$$Y_{\text{min}} > 0, \tag{4.5}$$

and in our numerical simulations we restrict the values of the flow resistance such that $\bar{Y}(\bar{\epsilon}^p, e^p, C_L, C) \geq Y_{\text{min}}$.

4.2 Effects of hydrogen in plane strain tension

In this section we study the effect of hydrogen on the plane-strain tensile deformation of a BCC Iron system. With reference to Fig. 4-1, we consider a metal specimen with a gauge length of initial width $w_0 = 5\,\text{mm}$ and initial length $l_0 = 7.5\,\text{mm}$. We make use of the symmetry of the problem and mesh only a quarter of the geometry with 1347 four-noded plane-strain elements.

The material parameters are given in Table 4.2. For the gradient regularization parameters we chose

$$Z = 5\,\text{GPa}, \quad B = 1\,\text{Pa}, \quad \text{and} \quad l = 0.05\,\text{mm} \tag{4.6}$$

which are chosen based on the work by Anand et al. (2012).

Throughout the simulation the nodes along the symmetry edge AB are prescribed to have displacement component $u_2 = 0$ and zero hydrogen flux, while the nodes along the symmetry edge BC are prescribed to have displacement component $u_1 = 0$ and zero hydrogen flux. The simulation is isothermal with all nodes held at a constant temperature $\vartheta_0 = 473\,\text{K}$; this high temperature of 200 °C is chosen so that the lattice hydrogen diffusivity D_L is increased and the effect of hydrogen on the deformation is increased.

This simulation has two steps:

Step 1. Hydrogen charging: in this step we introduce hydrogen into the specimen. The step begins with all nodes having an initial lattice chemical potential $\mu_{L,i}$. The lattice chemical potential on the surface AD is increased linearly from $\mu_{L,i}$ to $\mu_{L,f}$ in 100 seconds, and is then held constant for 1 hour. All other surfaces have a zero hydrogen flux boundary condition. At the end of the step the specimen is charged to a relatively uniform hydrogen concentration C_0.

Step 2. Mechanical loading: in this step we deform the specimen in tension. The nodes along the edge CD are prescribed to have displacement component $u_1 = 0$ and a constant velocity in the e_2-direction corresponding to $v_0 = 0.001\,\text{mm/sec}$, while the edge AD is traction free. The lattice chemical potential on the surface AD is held constant at $\mu_{L,f}$.

Step 1 of this numerical experiment simulates hydrogen-charging the metal specimen by increasing the partial pressure p_{H_2} to which the specimen is exposed from an initial value $p_{\text{H}_2,i}$ to a final value $p_{\text{H}_2,f}$. We perform three different simulations; first we consider a simulation in which hydrogen is not charged into the specimen prior to mechanical deformation, that is $p_{\mathrm{H}_2,f} = p_{\mathrm{H}_2,i}$ and $\mu_{L,f} = \mu_{L,i}$, and the hydrogen concentration remains at its initial value. Then we consider two simulations in which hydrogen gas pressure is increased to $p_{\mathrm{H}_2,f}$, resulting in a hydrogen concentration C_0 prior to deformation. The specific values of $\mu_{L,i}$ and $\mu_{L,f}$ are given in Table 4.1 and are computed using (3.13) according to the hydrogen gas pressures p_{H_2} also given in the Table 4.1.[1]

Table 4.1: Prescribed chemical potential μ_L and corresponding lattice, trapped, and total hydrogen concentrations.

$p_{\mathrm{H}_2,i}$ (kPa)	$\mu_{L,i}$ (kJ/mol)	$C_{L,i}$ (mol/m^3)	$C_{T,i}$ (mol/m^3)	C_i (mol/m^3)
1×10^{-3}	-54.457	5.695×10^{-4}	4.007×10^{-6}	5.735×10^{-4}

$p_{\mathrm{H}_2,f}$ (kPa)	$\mu_{L,f}$ (kJ/mol)	C_{L0} (mol/m^3)	C_{T0} (mol/m^3)	C_0 (mol/m^3)
1×10^{-3}	-54.457	5.695×10^{-4}	4.007×10^{-6}	5.735×10^{-4}
35	-33.882	0.106	4.908×10^{-4}	0.107
50	-33.181	0.127	5.494×10^{-4}	0.128

Fig. 4-2 show contours of total hydrogen concentration C prior to mechanical loading for (a) the uncharged simulation, (b) the simulation charged to $C_0 = 0.107\,\mathrm{mol/m^3}$ and (c) the simulation charged to $C_0 = 0.128\,\mathrm{mol/m^3}$. Note from the contours that the charged simulations have an essentially homogeneous hydrogen concentration prior to deformation.

Fig. 4-3 shows contours of (a) total hydrogen concentration C, (b) lattice hydrogen concentration C_L, and (c) trapped hydrogen concentration C_T at nominal end displacements of (1) $u = 0.6\,\mathrm{mm}$ and (2) $u = 0.8\,\mathrm{mm}$, for the simulation charged to $C_0 = 0.107\,\mathrm{mol/m^3}$. At a nominal end displacement of $u = 0.6\,\mathrm{mm}$, the total hydrogen concentration C is largest near the surface of the specimen, see Fig. 4-3 (a.1), while at a nominal end displacement of $u = 0.8\,\mathrm{mm}$ it is largest near the center of the specimen, see Fig. 4-3 (a.2). It is important to understand what governs this change in the behavior of the total hydrogen concentration as we deform the specimen.

Early in the deformation process the total hydrogen concentration C is governed by the lattice hydrogen concentration C_L while the trapped hydrogen concentration C_T is insufficiently large to significantly alter the total hydrogen concentration behavior, see Figs. 4-3 (a.1), (b.1), and (c.1). As the deformation progresses, and the number of available trap sites increases due to plastic deformation, hydrogen diffuses from the exterior of the specimen to fill those available trap sites and the trapped hydrogen concentration C_T increases, compare Figs. 4-3 (c.1) and (c.2) and note the change in scale. Eventually the total hydrogen concentration C is governed by the trapped hydrogen concentration C_T, see Figs. 4-3 (a.2), (b.2), and (c.2).

It is important to note that as we deform the specimen plastically the total hydrogen concentration C increases from its original charged value C_0, due to (i) the effect of the volumetric elastic strains on the lattice chemical potential, see eq. (2.212), which causes an increase in the lattice hydrogen concentration C_L and (ii) the increase in the number of available trap sites (with increas-

---

[1] The corresponding lattice hydrogen concentrations are computed from the hydrogen gas pressures p_{H_2} using (3.7) and with the fugacity given in (3.12). The trapped hydrogen concentrations are computed from the lattice hydrogen concentration using (2.206). All other material properties necessary for computing these boundary conditions are listed in Table 4.2.

ing plastic deformation) which causes hydrogen to diffuse from the specimen surface to satisfy the available trap sites and thus increases the trapped hydrogen concentration C_T. We have illustrated in Fig. 4-3 the manner in which the interplay between these two behaviors can affect the total hydrogen concentration in a specimen subject to plane-strain tension.

As the specimen is deformed, the total hydrogen concentration C increases and eventually reaches the critical concentration C_c, at which time the specimen begins to soften. Fig 4-4 shows contours of equivalent tensile plastic strain $\bar{\epsilon}^p$ at a nominal end displacement of $u = 1.2\,\mathrm{mm}$ for (a) the uncharged simulation, (b) the simulation charged to $C_0 = 0.107\,\mathrm{mol/m^3}$, and (c) the simulation charged to $C_0 = 0.128\,\mathrm{mol/m^3}$.

As the hydrogen concentration prior to mechanical loading C_0 is increased, the onset of shear band formation is accelerated since the critical concentration C_c at which hydrogen induced softening occurs is reached earlier in the deformation process. In the case of the simulation charged to $C_0 = 0.107\,\mathrm{mol/m^3}$, softening occurs when the maximum total hydrogen concentration is largest at the center of the specimen and thus shear bands form at the center of the specimen, see Fig. 4-4 (b). For the simulation charged to $C_0 = 0.128\,\mathrm{mol/m^3}$, softening occurs when the maximum total hydrogen concentration is largest on the specimen surface and thus shear bands form at the specimen surface, see Fig. 4-4 (c). As expected, in the uncharged simulation no shear bands form since the critical concentration C_c is not reached.

With the model developed here, hydrogen charging causes the plastic deformation to localize into shear bands. The location of the shear bands, as well as the time during the deformation process when plastic localization occurs, is governed by the amount of hydrogen charged prior to deformation. The time at which plastic localization occurs is further illustrated in the corresponding engineering stress-strain curves shown in Fig. 4-5.

4.2.1 Mesh insensitivity

In order to illustrate that the above simulations are mesh-insensitive due to the strain gradient effects included in our theory, we consider two additional meshes containing 401 and 3237 four-noded plane-strain elements, see Fig. 4-6. The geometry and the boundary conditions are all identically to the simulations performed above. For comparison to the above results here we simulate the case were the specimens are charged to $C_0 = 0.107\,\mathrm{mol/m^3}$ prior to deformation.

Fig. 4-7 (a) shows contours of equivalent tensile plastic strain at a nominal end displacement of $u = 1.2\,\mathrm{mm}$, and Fig. 4-7 (b) at a nominal end displacement of $u = 1.4\,\mathrm{mm}$. In all simulations shown in Fig. 4-7 the width of the shear bands is finite and independent of the element size. Fig. 4-8 shows that the corresponding engineering stress-strain curves are converging to an essentially identical result and are thus independent of the spatial discretization used. Our purpose in the use of a strain-gradient theory is simply for numerical regularization and ease of computation, for a more detailed study of the use of this form of gradient theory and its effect on shear band regularization see Anand et al. (2012).

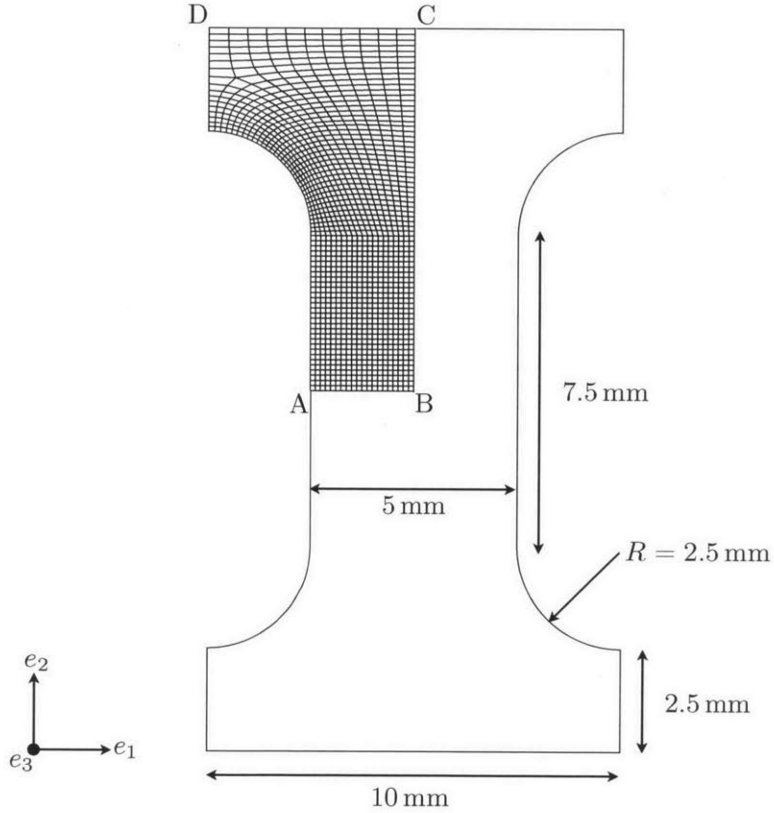

Figure 4-1: Schematic of the geometry and finite element mesh used for plane-strain tension simulations.

Table 4.2: Representative material properties for a BCC Iron system.

	Variable	Units	Value	Source	Note
Elastic Parameters	G	GPa	80		
	K	GPa	175		
Thermal Properties	α	1/K	11.8×10^{-6}	Gale and Totemeier (2004)	(a)
	c	J/(kg K)	449	Gale and Totemeier (2004)	(a)
	κ	W/(m K)	80.4	Gale and Totemeier (2004)	(a)
	R	J/(mol K)	8.3145		
Plastic Parameters	Y_0	MPa	300		
	Y_{sat}	MPa	500		
	H_{hard}	GPa	25		
	H_{soft}	GPa	22.5		
	C_c	mol/m^3	0.15		
	Y_{min}	MPa	1		
Solubility Parameters	K_0	mol/(m$^3\sqrt{\text{MPa}}$)	820	Krom et al. (1997)	(a)
	ΔH	kJ/mol	28.6	Krom et al. (1997)	(a)
	b	m^3/mol	15.84×10^{-6}	San Marchi et al. (2007)	
Diffusion Parameters	μ_L^0	kJ/mol	28.6		(b)
	D_{L0}	m^2/sec	2.76×10^{-7}	Krom et al. (1997)	
	Q	kJ/mol	12.9	Krom et al. (1997)	
	β	m^3/mol	0.667×10^{-6}	Hirth (1980)	
	φ		6	Krom and Bakker (2000)	(c)
	N_L	mol/m^3	8.4624×10^5	Gale and Totemeier (2004)	(d)
Trapping Parameters	W_B	kJ/mol	-60	Krom et al. (1999)	
	N_T	mol/m^3	Note (e)	Krom et al. (1999)	

(a) These values are for pure Iron.

(b) Recall from (3.11) that $\mu_L^0 = \Delta H$. The value of μ_T^0, although unnecessary in our numerical implementation, can be computed from (2.205) and the value of W_B.

(c) We assume tetrahedral occupancy of hydrogen on a BCC lattice, for which $\varphi = 6$.

(d) N_L is computed from (2.181) with $\rho_{\text{M}} = 7870$ kg/m^3, $\mathcal{M}_{\text{M}} = 55.8 \times 10^{-3}$ kg/mol, and $\varphi = 6$.

(e) The evolution of trapping sites is taken from Krom et al. (1999) to be given by:

$$\log N_T = 23.26 - 2.33 \exp(-5.5\bar{\epsilon}^p).$$

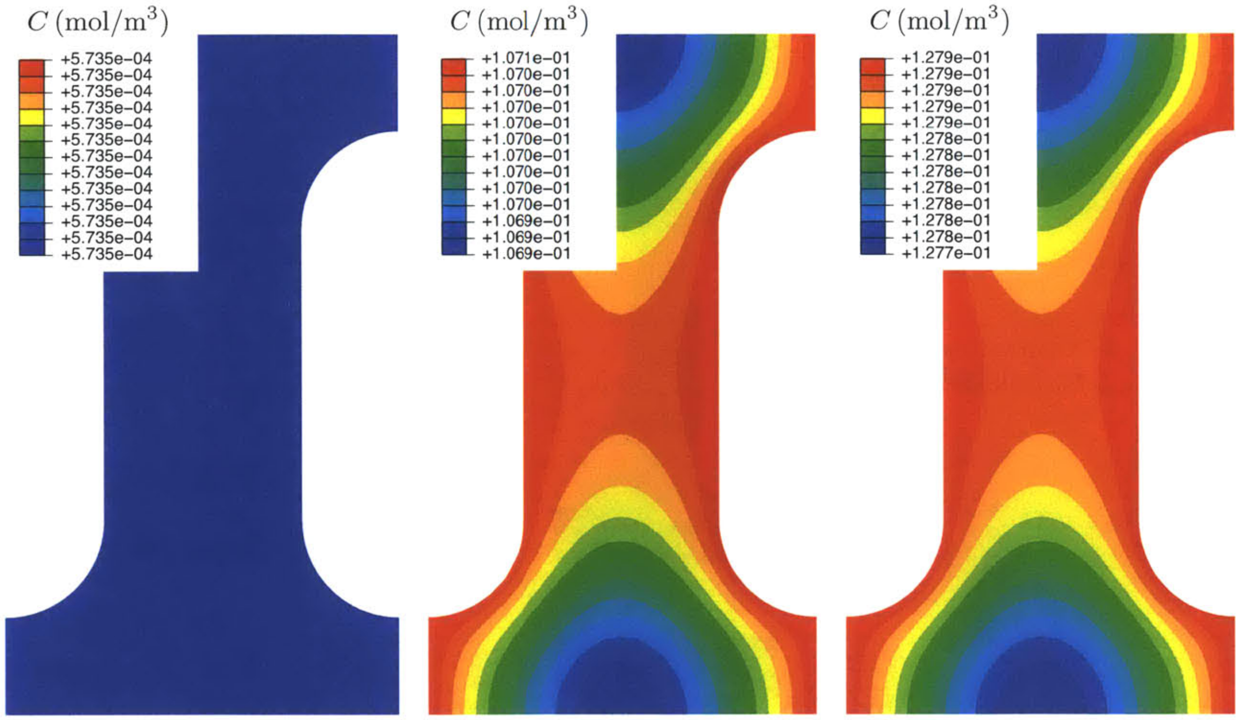

(a) (b) (c)

Figure 4-2: Contours of total hydrogen concentration C prior to mechanical loading for (a) the uncharged simulation, (b) the simulation charged to $C_0 = 0.107\,(\mathrm{mol/m^3})$, and (c) the simulation charged to $C_0 = 0.128\,(\mathrm{mol/m^3})$.

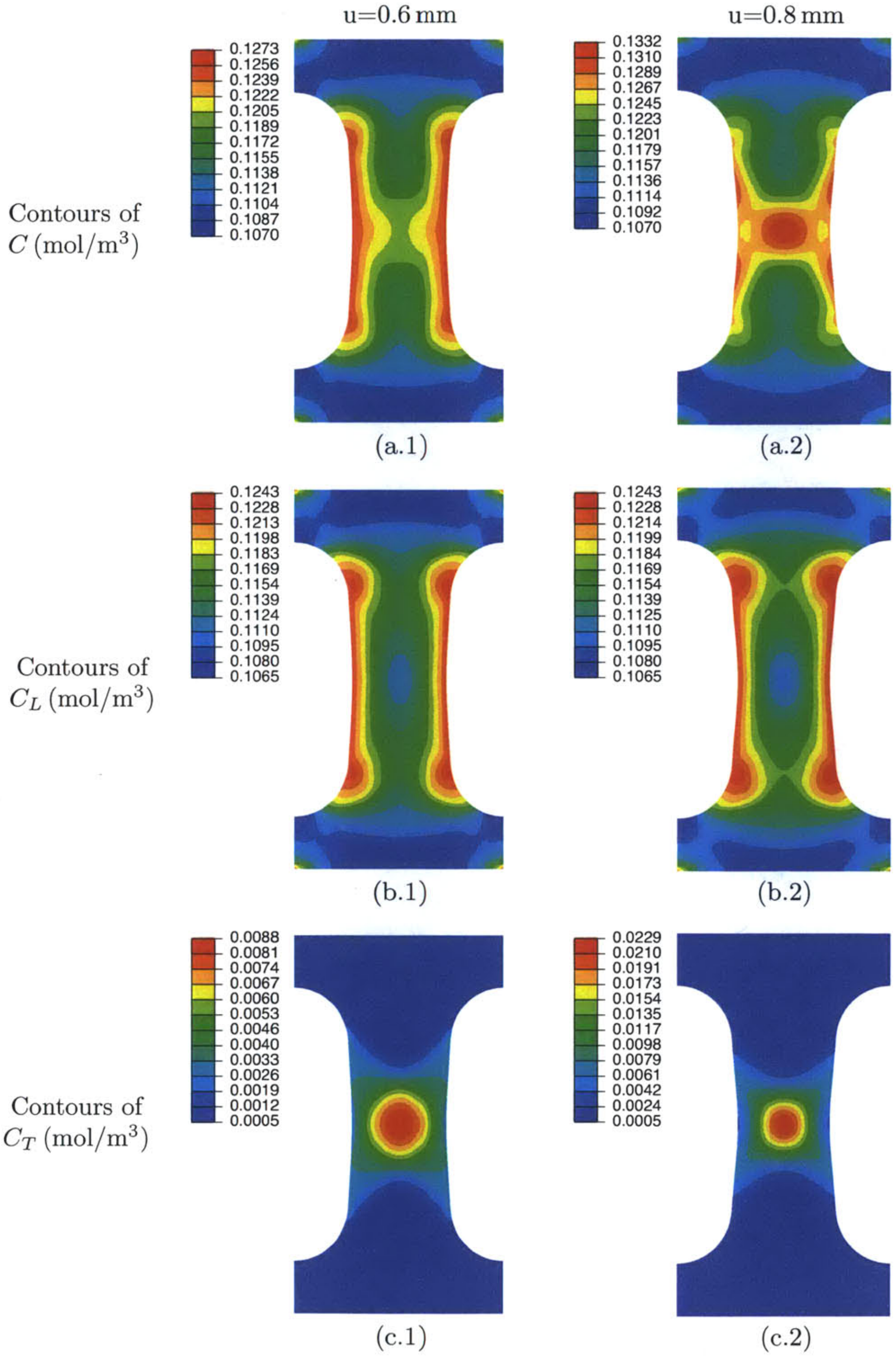

(a.1) (a.2)

(b.1) (b.2)

(c.1) (c.2)

Figure 4-3: Contours of (a) total hydrogen concentration C, (b) lattice hydrogen concentration C_L, and (c) trapped hydrogen concentration C_T at a nominal end displacement of (1) $u = 0.6\,\text{mm}$ and (2) $u = 0.8\,\text{mm}$, for the simulation charged to $C_0 = 0.107\,\text{mol/m}^3$ prior to deformation.

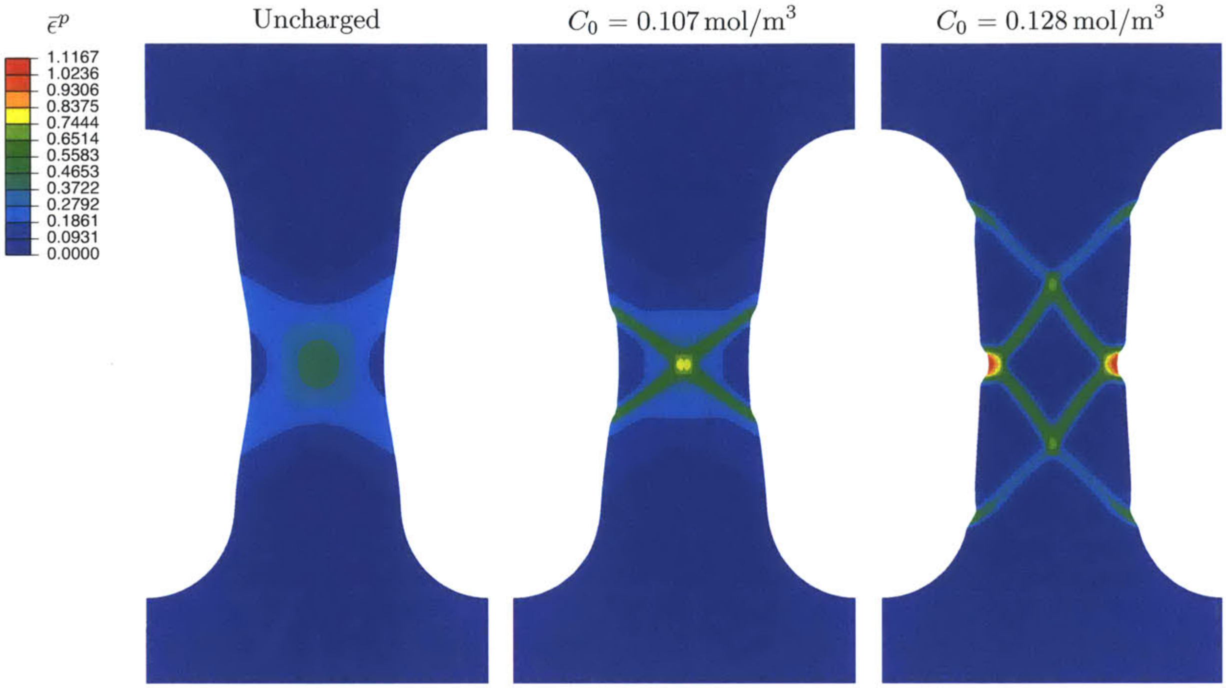

(a) (b) (c)

Figure 4-4: Contours of equivalent tensile plastic strain $\bar{\epsilon}^p$ at a nominal end displacement of $u = 1.2\,\text{mm}$ for (a) the uncharged simulation, (b) the simulation charged to $C_0 = 0.107\,\text{mol/m}^3$, and (c) the simulation charged to $C_0 = 0.128\,\text{mol/m}^3$.

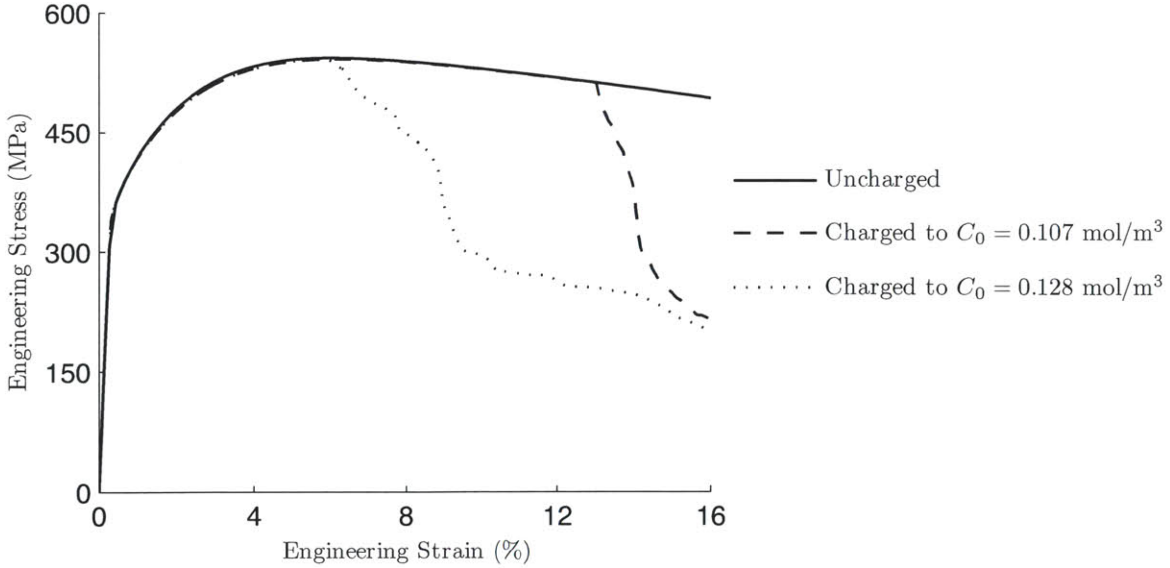

Figure 4-5: Engineering stress versus strain curves for uncharged and charged plane-strain tension simulations.

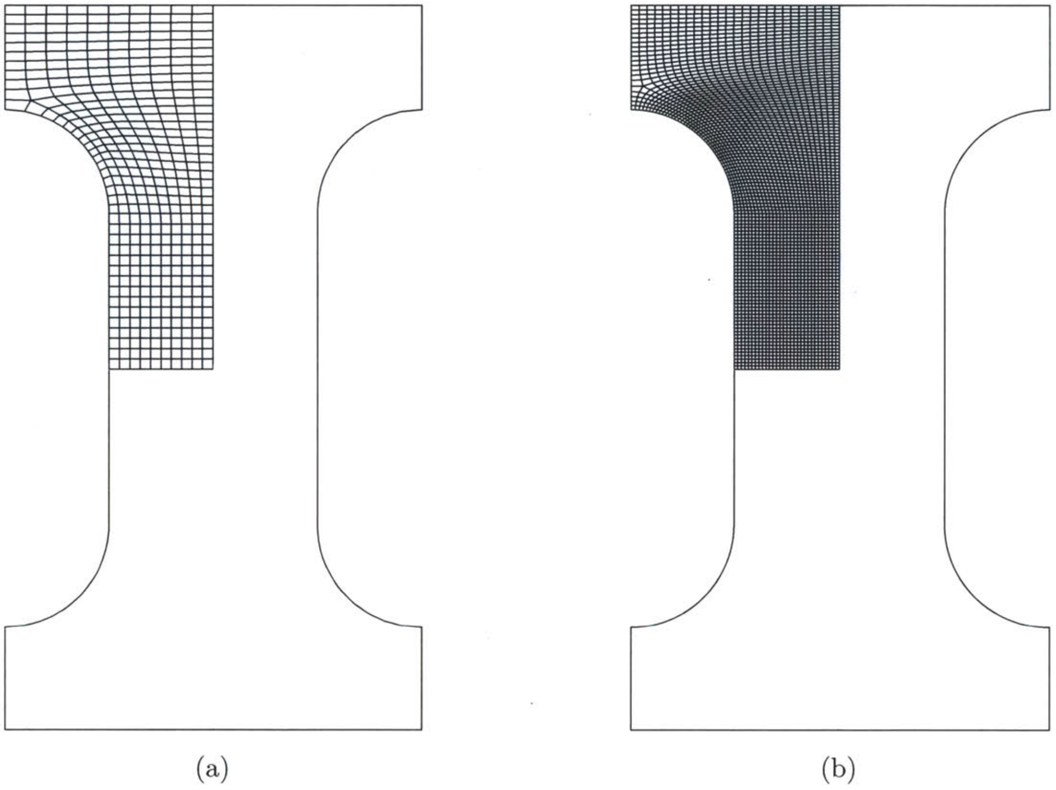
(a) (b)

Figure 4-6: Finite element meshes used for studying mesh sensitivity having (a) 401 elements and (b) 3237 elements.

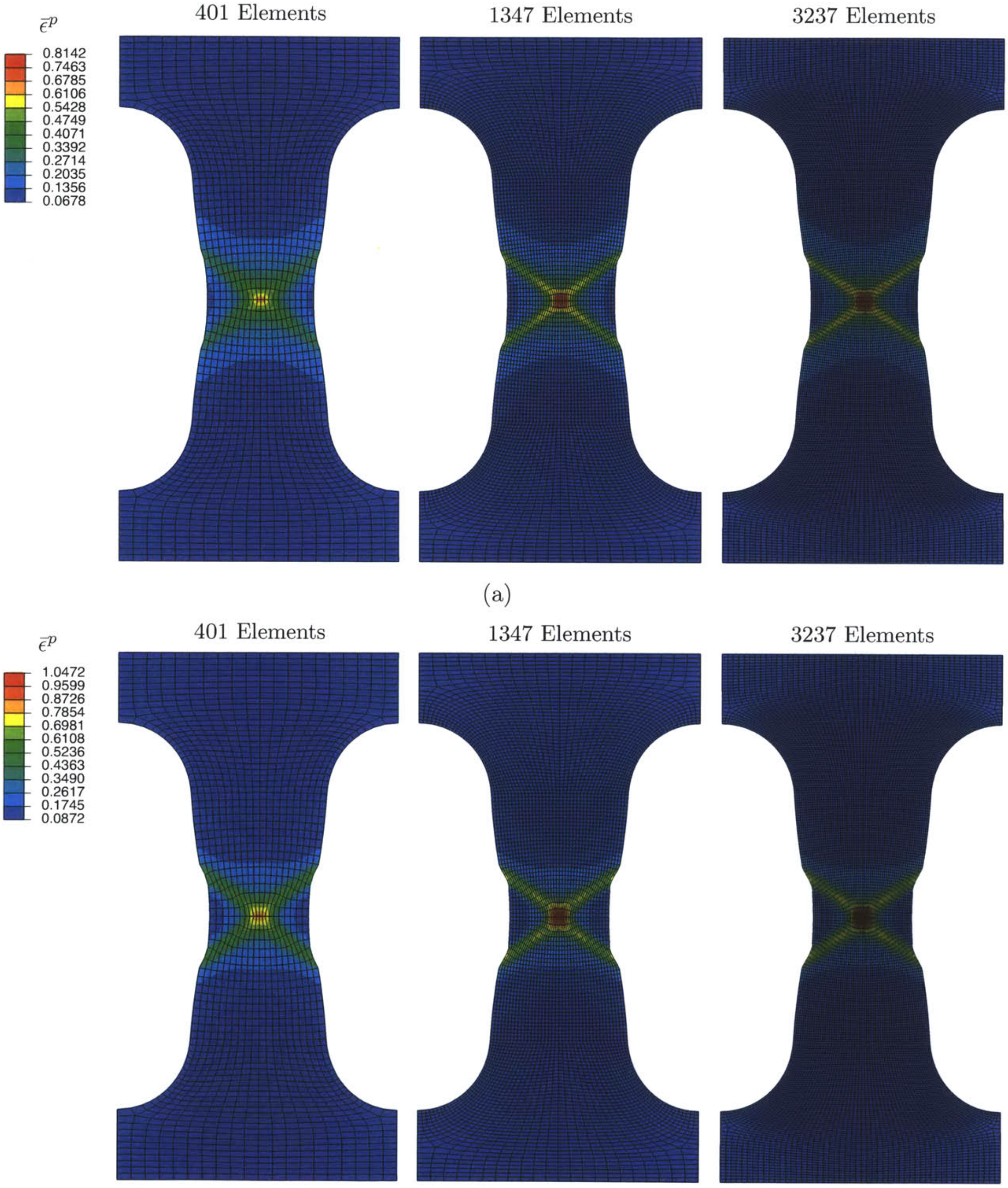

Figure 4-7: Contours of equivalent tensile plastic strain $\bar{\epsilon}^p$ for plane-strain tension simulations with three different meshes at a nominal end displacement of (a) 1.2 mm and (b) 1.4 mm.

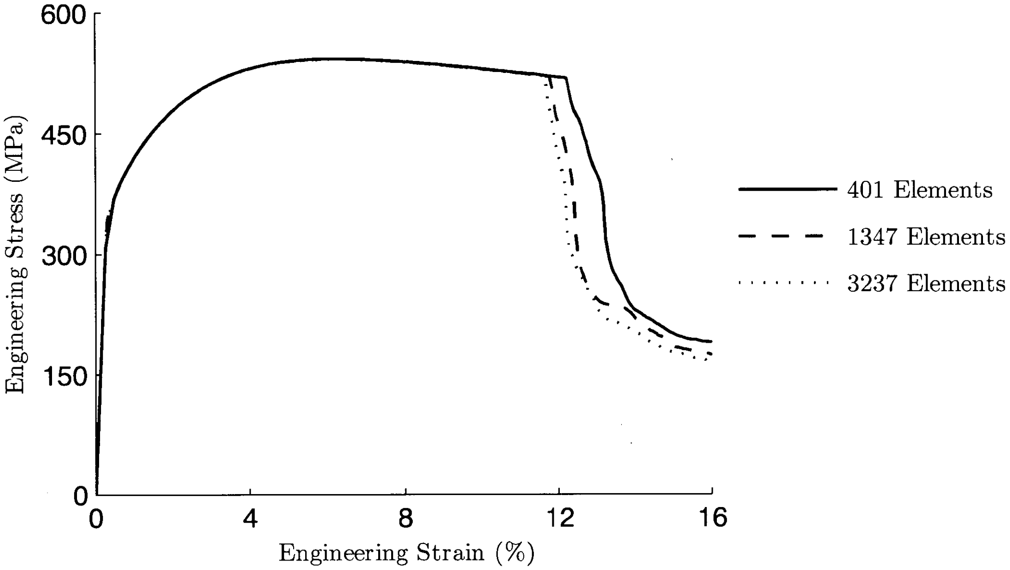

Figure 4-8: Engineering stress versus strain curves for three plane-strain tension simulations with different meshes.

4.3 Effects of hydrogen on three-point bending of a U-notched specimen

In this section we study the effect of hydrogen on a U-notched metal specimen deformed in three-point bending and provide a qualitative comparrison against the experimental results of Lee et al. (1977, 1979).

Because of the symmetry of the problem we mesh only half of the U-Notched specimen with 4742 four-noded plane-strain elements, the geometry (which is identical to the experimental specimens used in Lee et al. (1977, 1979)) and the mesh used are shown in Fig. 4-9. For ease of computation we use deformable plane-strain elements to model the top and bottom rollers with an elastic modulus of 1000 GPa, effectively making them rigid. The contact between the rollers and the specimen is frictionless.

The material parameters are given in Table 4.2. For the gradient regularization parameters we chose

$$Z = 2.5\,\text{GPA}, \quad B = 1\,\text{Pa}, \quad \text{and} \quad l = 0.5\,\text{mm}. \tag{4.7}$$

The specific choice of these parameters is based on a brief study on the effects of the regularization parameters l and Z on the simulations performed here which is provided in Section 4.3.1. In order to simulate material imperfections we seed the elements in the simulation with a random variation in the initial yield strength Y_0. The variation is gaussian with a mean of 0 MPa and a standard deviation of 5 MPa. A brief discussion on the effect of the variation in Y_0 is provided in Section 4.3.2.

This simulation has two steps, throughout both steps all nodes are held at a constant temperature $\vartheta_0 = 298\,\text{K}$:

Step 1. Hydrogen charging: in this step we introduce hydrogen through the notch surface. The step begins with all nodes having an initial lattice chemical potential $\mu_{L,i}$. The lattice chemical potential on the notch surface, edge DE, is increased linearly from $\mu_{L,i}$ to $\mu_{L,f}$ in 100 seconds, and is then held constant for 2000 seconds. All other surfaces have a zero hydrogen flux boundary condition. Throughout this step all nodes are prescribed to have displacement components $u_1 = 0$ and $u_2 = 0$.

Step 2. Three-point bending: in this step we deform the specimen in three-point bending. Throughout this step the nodes along the edge AE are prescribed to have displacement component $u_1 = 0$, while the node on point A is prescribed to have displacement components $u_1 = 0$ and $u_2 = 0$. All nodes on the bottom roller are fixed in space, while all nodes on the top roller are prescribed to have displacement component $u_1 = 0$ and a constant velocity in the e_2-direction corresponding to $v_0 = 0.001\,\text{mm/sec}$. Throughout this step all surfaces have a zero hydrogen flux boundary condition.

Step 1 of this simulation is meant to recreate the experimental procedures of Lee et al. (1977, 1979) in which hydrogen was charged electrolytically through the notch surface at a current density of $100\,\text{A/m}^2$ for 2.5 hours, while all other surfaces were insulated with a non-conductive paint. Step 2 recreates the mechanical loading performed on the specimens by the same authors.

The initial lattice chemical potential $\mu_{L,i}$ is computed using (3.13) with a hydrogen gas pressure of $p_{\text{H}_2} = 0.101\,\text{MPa}$, while the final lattice chemical potential $\mu_{L,f}$ is computed using (3.10) with a hydrogen fugacity of $f_{H_2} = 1\,\mathrm{GPa}$, see Table 4.3 [2]. In Lee et al. (1979), the authors estimate that a current density of $100\,\mathrm{A/m^2}$ corresponds to a stead-state hydrogen fugacity of 1 GPa.

Table 4.3: Prescribed chemical potential μ_L and corresponding lattice, trapped, and total hydrogen concentrations

	μ_L (kJ/mol)	C_L (mol/m^3)	C_T (mol/m^3)	C (mol/m^3)
$p_{H_2} = 0.101$ MPa	-20.033	2.530×10^{-3}	1.399×10^{-3}	3.929×10^{-3}
$f_{H_2} = 1$ GPa	-8.636	0.252	1.413×10^{-3}	0.253

We refer to the above described simulation as the *hydrogen-charged* simulation, since hydrogen is charged in the specimen prior to mechanical loading. We also perform a simulation, which we refer to as the *uncharged* simulation, in which we do not charge hydrogen in the specimen prior to deformation, that is $\mu_{L,f} = \mu_{L,i}$.

Figs. 4-10 (a) and (b) show contours of total hydrogen concentration before loading for the hydrogen-charged and uncharged simulations respectively. Fig. 4-11 shows the variation in yield strength Y_0 before the start of the simulations at (a) near the notch and (b) for the entire specimen.

In Fig. 4-12 we qualitatively compare our results with the experiments of Lee et al. (1977). Fig. 4-12 (a) shows the experimental results of Lee et al. (1977) for a specimen charged with hydrogen before being mechanically loaded in three-point bending, while Fig. 4-12 (b) shows the same result for a specimen which has not been charged. Figs. 4-12 (c) and (d) show contours of equivalent tensile plastic strain at a mid-span deflection of 0.15 mm for the hydrogen-charged and uncharged simulations respectively. Due to the high hydrogen content of the hydrogen-charged specimen prior to loading, see Fig. 4-10 (a), there is softening in the vicinity of the notch which results in the formation of shear bands. In the uncharged simulation there is no localization and plastic deformation occurs in a diffuse region around the notch tip. *Our simulations are in good qualitative agreement with the experimental results of Lee et al. (1977) in that pre-charging the specimen with hydrogen induces plastic localization into multiple shear bands at the notch.* Note that no attempt is made here to match the quantitative force versus mid-span deflection results from the experiments of Lee et al. (1977) with our numerical simulations.

For clarity, Fig. 4-13 shows a closer view of the contours of equivalent tensile plastic strain near the notch tip. Finally, as one might expected, hydrogen-charging reduces the force required to deform the U-notched specimen in three-point bending, see Fig. 4-14.

Multiple shear bands, as oppose to a single dominating shear band, form due to the gradient in hydrogen concentration prior to deformation. Fig. 4-15 shows contours of equivalent plastic strain near the notch tip at four times during loading: (a) 80 sec, (b) 100 sec, (c) 120 sec, and (d) 140 sec. The first shear band forms, Fig. 4-15 (a), and grows until it reaches the region in which the total hydrogen concentration is lower than the critical concentration for strain-softening to occur, that is it grows until it hits the portion of the material in which $C < C_c$, see Fig. 4-15 (b). Once this occurs a second shear band forms further away from the notch tip and grows until it reaches the same region where $C < C_c$, see Figs. 4-15 (c) and (d). A third shear band also forms near the

---

[2] The corresponding lattice hydrogen concentrations are computed from (3.7) with the fugacity directly prescribed or computed from the gas pressure p_{H_2} through (3.12). The trapped hydrogen concentrations are computed from the lattice hydrogen concentration using (2.206). All other material properties necessary for computing these boundary conditions are listed in Table 4.2.

symmetry line and grows until it reaches the symmetry line. Our experience with these simulations is that if the hydrogen concentration prior to loading is high but uniform throughout the material, only a single shear band forms, as oppose to multiple shear bands forming as shown in Fig. 4-13 (a).

4.3.1 Effect of the regularization parameters l and Z on the formation of shear bands in the hydrogen-charged simulations

In this section we study the effects of the regularization parameters l and Z on the formation of shear bands in the simulation of a hydrogen-charged U-notched specimen deformed in three point bending. The simulations discussed in this section are identical to the hydrogen-charged simulation described previously except that the parameters l and Z are varied. As discussed in Section 2.11.4, on physical grounds we require that the parameter B be much smaller than Z, and thus do not include variations in B in this study and set $B = 1\,\mathrm{Pa}$ in all simulation.

Fig. 4-16 shows contours of equivalent tensile plastic strain $\bar{\epsilon}^p$ at a mid-span deflection of 0.15 mm with (a) the energetic length scale $l = 0.1\,\mathrm{mm}$, (b) the energetic length scale $l = 0.5\,\mathrm{mm}$, and for (1) the modulus $Z = 1\,\mathrm{GPa}$, (2) the modulus $Z = 2.5\,\mathrm{GPa}$ and (3) the modulus $Z = 5\,\mathrm{GPa}$. As can be seen in Fig. 4-16, higher values of the modulus Z result in wider shear bands and plastic deformation which is diffused over a larger region of the material. Correspondingly, as we increase Z, and plastic deformation occurs over a wider region of the material, the maximum value of $\bar{\epsilon}^p$ is lower. It is also interesting to note that varying Z can affect the pattern and shape of the shear bands that form, compare Figs. 4-16 (b.1) and (b.2). Higher values of the length scale l result in plastic deformation which is localized into narrower bands, and subsequently also results in the formation of more shear bands. Based on this brief study we chose to use $l = 0.5\,\mathrm{mm}$ and $Z = 2.5\,\mathrm{GPa}$, see Fig. 4-16 (b.2), in the simulations presented previously in this Chapter.

4.3.2 Effect of the variation in initial yield strength Y_0

In this section we study the effect of seeding the elements with a random variation in the initial yield strength Y_0 in order to simulate material imperfections. To study this effect we simulate a hydrogen-charged U-notched specimen deformed in three point bending which has *no variation in the yield strength* Y_0 and compare to the hydrogen-charged simulation described previously which has a variation in Y_0, see Fig. 4-11. The two simulations are identical except for the difference in the yield strength Y_0.

Fig. 4-17 (a) shows the initial yield strength Y_0 prior to mechanical loading, for (a.1) a simulation having no variation in the initial yield strength and (a.2) a simulation having a gaussian variation with a mean of 0 MPa and a standard deviation of 5 MPa. Fig. 4-17 (b) shows contours of equivalent tensile plastic strain $\bar{\epsilon}^p$ at a mid-span deflection of 0.15 mm for (b.1) the simulations with no variation in Y_0 and (b.2) the simulation with variation in Y_0. As can be seen from Fig. 4-17 the introduction of a random variation in the initial yield strength Y_0 enhances the formation of multiple shear bands in the vicinity of the notch as well as produces better defined shear bands.

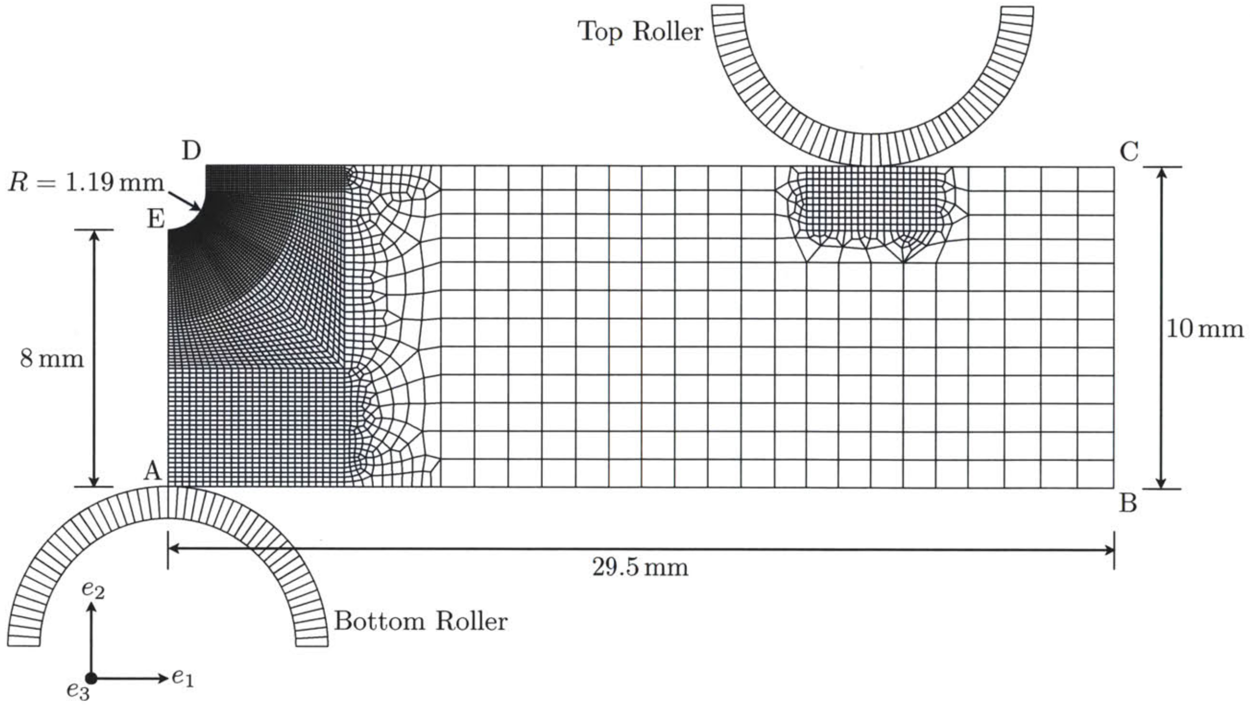

Figure 4-9: Schematic and finite-element mesh used in the U-Notched three-point bending simulations.

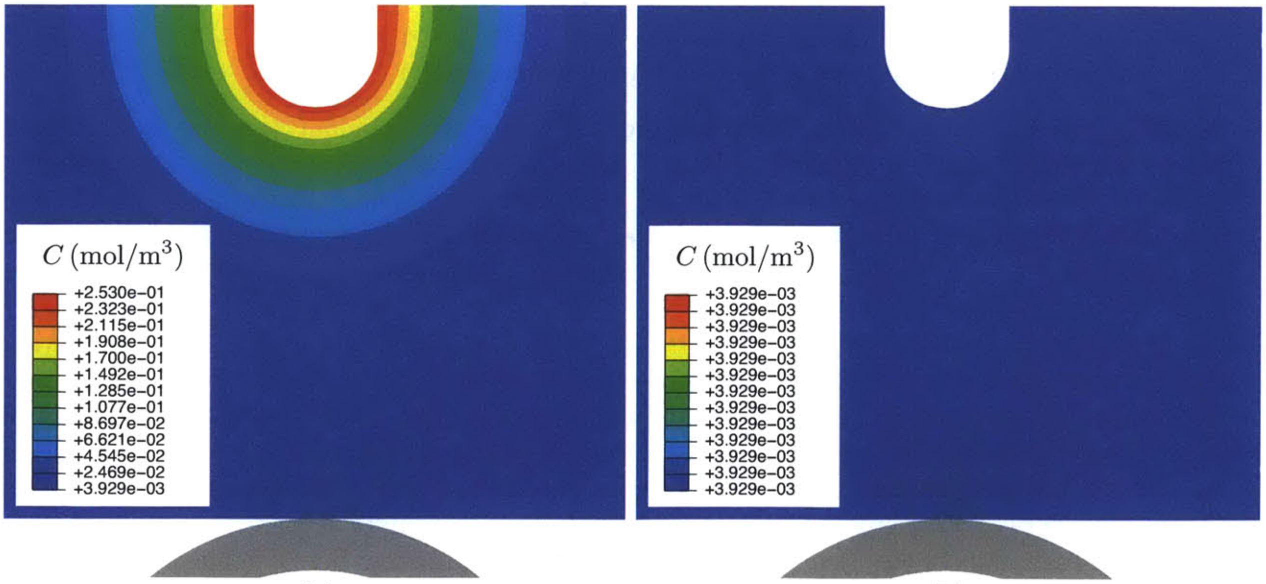

(a)

(b)

Figure 4-10: Contours of total hydrogen concentration before loading for (a) the hydrogen-charged simulation and (b) the uncharged simulation.

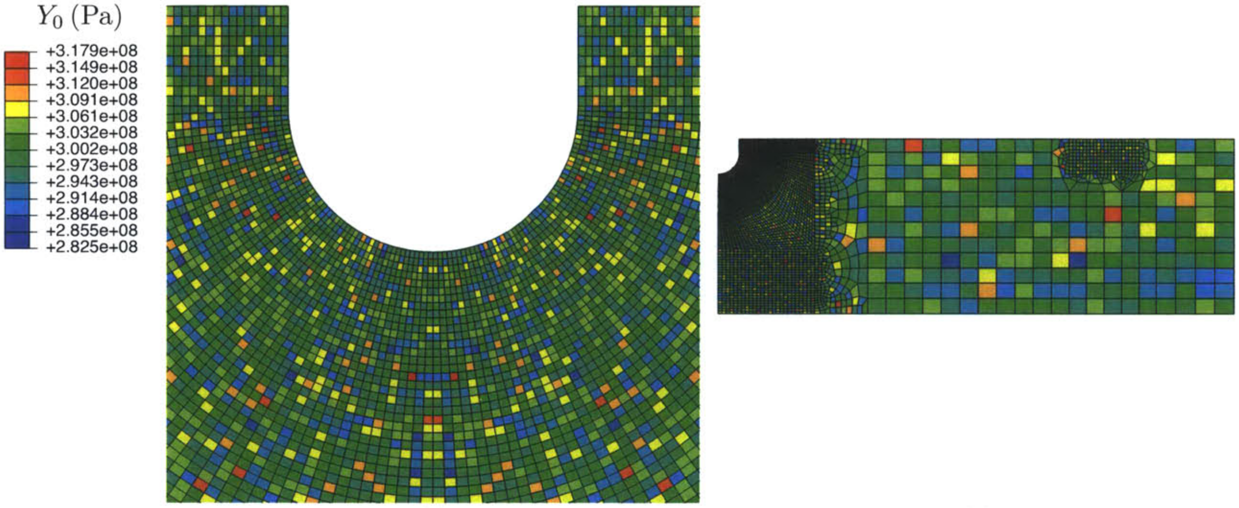

(a) (b)

Figure 4-11: Yield strength Y_0 prior to the start of the simulation (a) in the vicinity of the notch and (b) throughout the entire specimen.

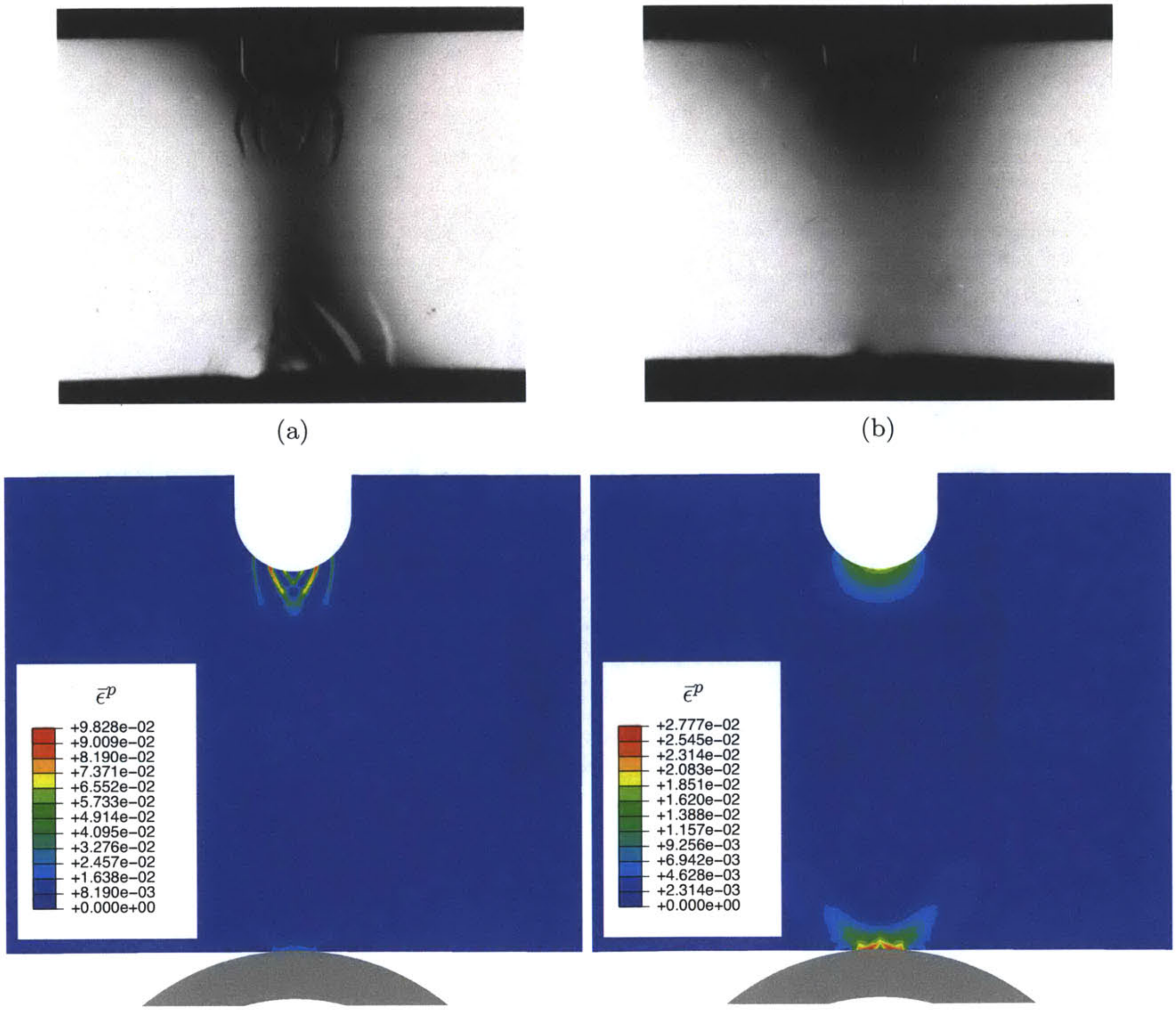

(a) (b)

(c) (d)

Figure 4-12: Effect of hydrogen on three-point bending of a U-notched specimen. (a) and (b) are from Lee et al. (1977) for a hydrogen-charged specimen and an uncharged specimen respectively. (c) and (d) show contours of equivalent plastic strain $\bar{\epsilon}^p$ at a mid-span deflection of 0.15 mm for a hydrogen-charged and an uncharged specimen respectively.

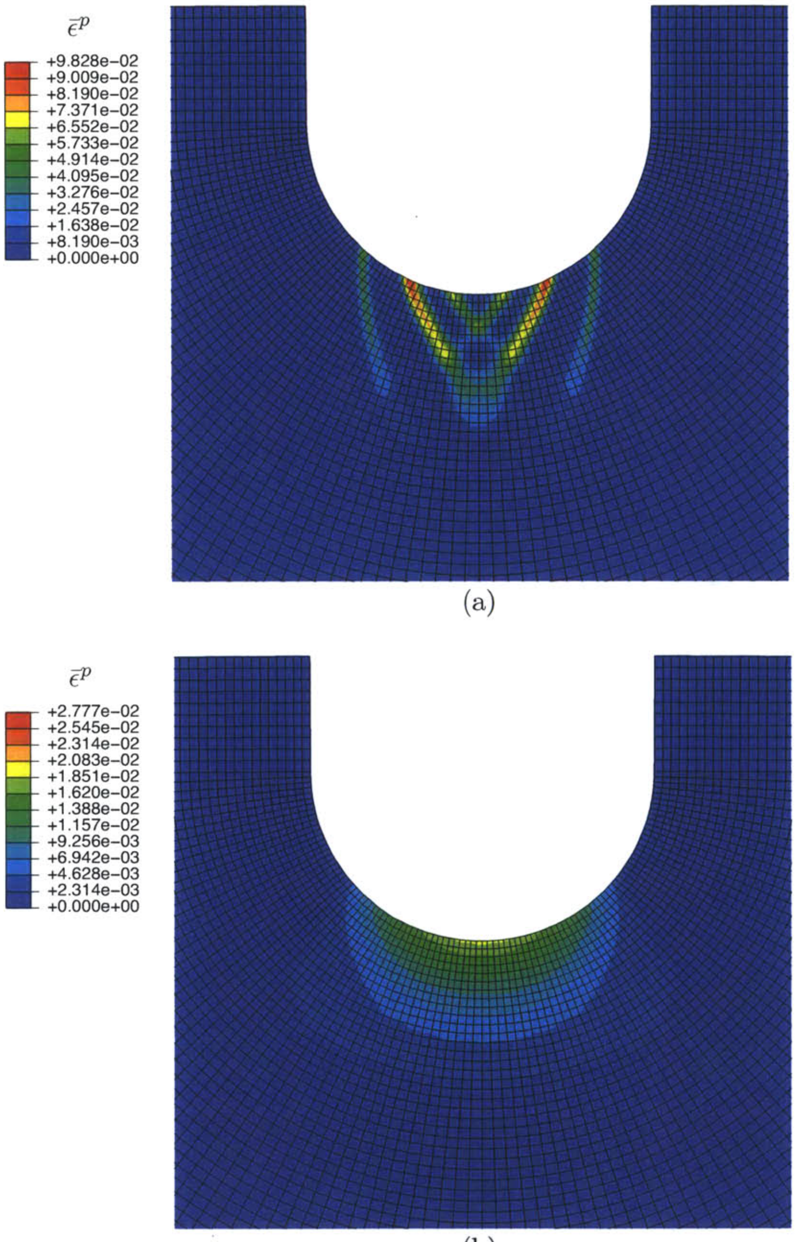

(a)

(b)

Figure 4-13: Contours of equivalent plastic strain $\bar{\epsilon}^p$ at a mid-span deflection of 0.15 mm near the notch for (a) a hydrogen-charged specimen and (b) an uncharged specimen.

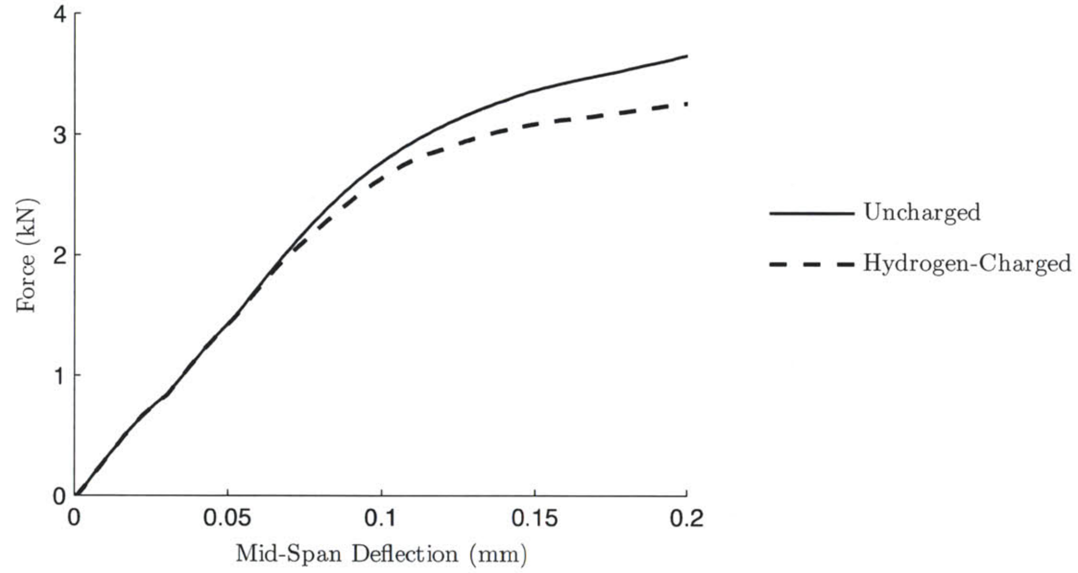

Figure 4-14: Force versus mid-span deflection curves for a hydrogen-charged and uncharged simulations of a U-notched specimen in three-point bending.

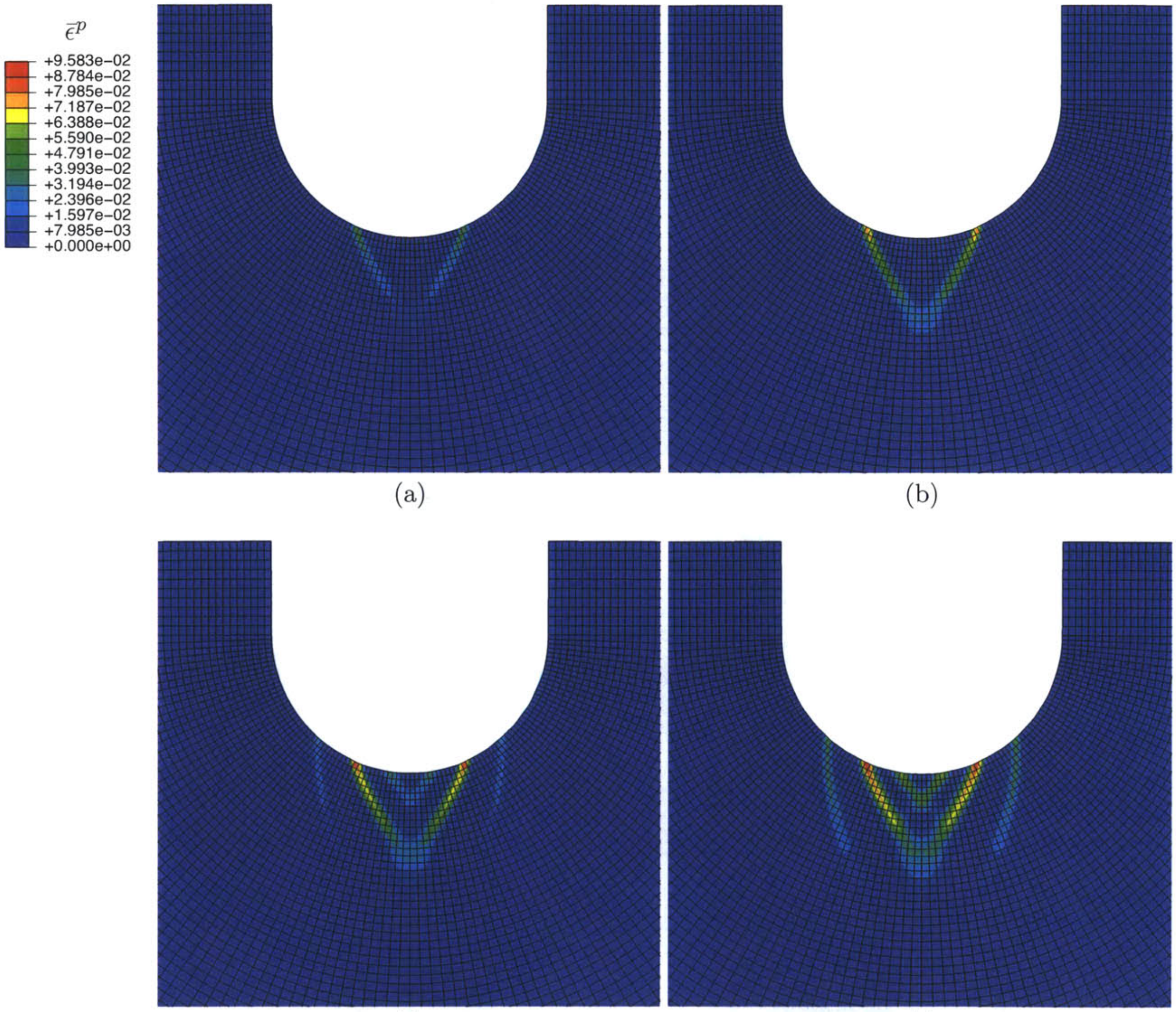

(a) (b)

(c) (d)

Figure 4-15: Contours of equivalent tensile plastic strain $\bar{\epsilon}^p$ for the hydrogen-charged simulation at (a) 80 seconds of loading, (b) 100 seconds of loading, (c) 120 seconds of loading, and (d) 140 seconds of loading.

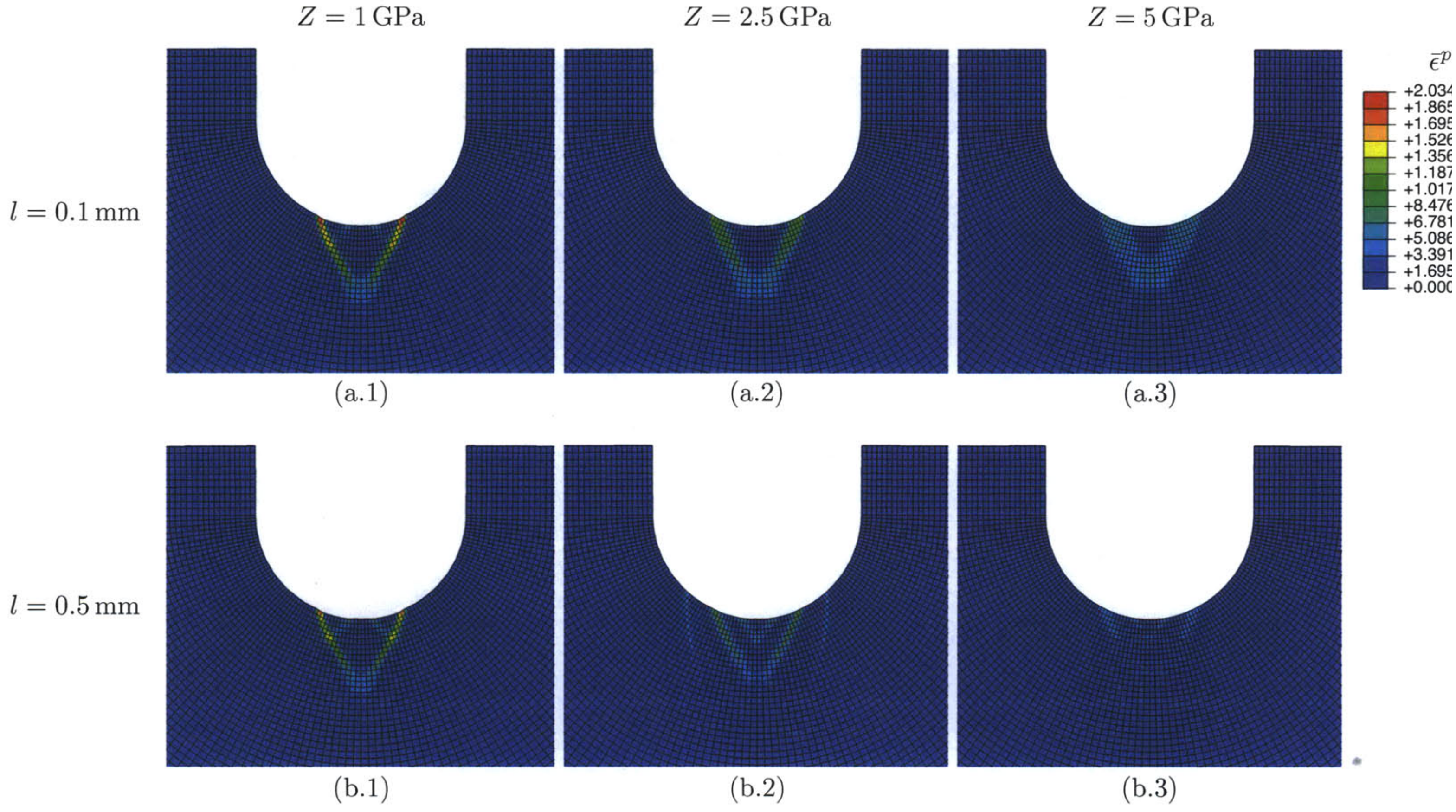

(a.1) (a.2) (a.3)

(b.1) (b.2) (b.3)

Figure 4-16: Contours of equivalent tensile plastic strain $\bar{\epsilon}^p$ for the hydrogen-charged simulation at a mid-span deflection of $0.15\,\mathrm{mm}$ the energetic length scale (a) $l = 0.1\,\mathrm{mm}$, (b) $l = 0.5\,\mathrm{mm}$ and the modulus (1) $Z = 1\,\mathrm{GPa}$, (2) $Z = 2.5\,\mathrm{GPa}$, and (3) $Z = 5\,\mathrm{GPa}$.

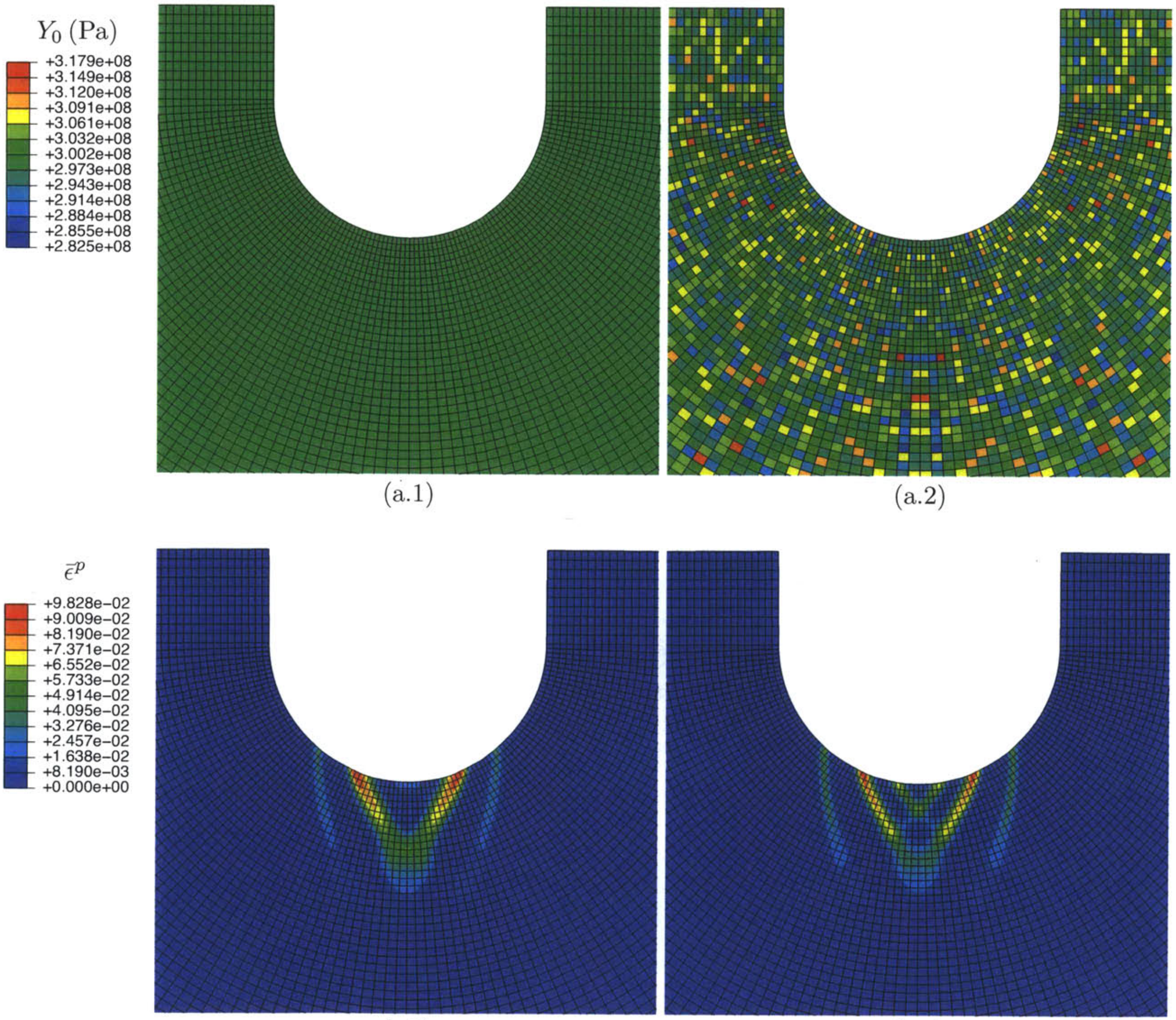

(a.1) (a.2)

(c.2) (b.2)

Figure 4-17: Contours of (a) yield strength Y_0 before mechanical loading and (b) equivalent tensile plastic strain $\bar{\epsilon}^p$ at a mid-span deflection of 0.15 mm for the hydrogen-charged simulation with (1) no variation in the initial yield strength Y_0 and (2) a gaussian variation in the yield strength Y_0 with a mean of 0 MPa and a standard deviation of 5 MPa.

4.4 Concluding remarks

In this Chapter we have numerically studied the effects of hydrogen on the plastic deformation of a BCC Iron system. To do so we have employed a plastic flow rule which undergoes softening when the hydrogen concentration reaches a critical value.

First, we studied the plane-strain tensile deformation of metal specimens that are either hydrogen-charged or uncharged prior to being mechanically deformed. As the specimen is mechanically deformed, while still exposed to hydrogen, we have showed that increases in the hydrogen concentration of the specimen can be attributed to both increases in the hydrogen residing in lattice sites as well as increases in the hydrogen residing in trap sites. We have showed that although the hydrogen atmosphere surrounding the specimen does not change, the lattice hydrogen concentration within the specimen can experience a significant increase due to the presence of volumetric tensile strains. Early in the deformation process the maximum hydrogen concentration within the specimen is governed by the hydrogen residing in lattice sites, while later in the deformation process it is governed by the hydrogen residing in trapping sites. Our theory, and corresponding numerical simulation, is capable of modeling the increase in hydrogen within a specimen as it is mechanically deformed, while exposed to hydrogen, which is crucial in developing a theory which seeks to couple the mechanical response of the material with the hydrogen distribution within it.

We have shown how the plastic deformation within the specimen localizes as the hydrogen concentration reaches a critical value, and the material begins to soften. Simulations which have been charged to different hydrogen concentrations have been compared in order to illustrate the different patterns of localized plastic deformation that form. The patterns depend on wether the total hydrogen concentration is governed by either the lattice hydrogen concentration or the trapped hydrogen concentration, at the moment when the critical hydrogen concentration is reached.

Secondly, we studied a U-notched specimen deformed in three-point bending, and compared our results qualitatively with those of Lee et al. (1977, 1979). As was done in the experimental work of Lee et al., we study a specimen that is hydrogen-charged prior to mechanical deformation and one that is uncharged. Our results are in good qualitative agreement with the experimental work of Lee et al., in that hydrogen-charging results in localized plastic deformation near the notch in the form of multiple shear bands.

Chapter 5

Conclusion

5.1 Summary

We have developed a reasonably general thermodynamically-consistent continuum-level theory to model hydrogen diffusion, trapping of hydrogen, diffusion of heat, and large elastic-plastic deformation of metals. We have specialized our theory with a set of constitutive equations which should be useful in application. Within our specialization, we have placed the widely-used notion of an "equilibrium" between hydrogen residing in normal interstitial lattice sites and hydrogen trapped at microstructural sites of Oriani (1970), within a precise thermodynamic framework.

The specialized theory has been implemented in a finite element program, and the numerical simulation capability has been used to study three important problems. First, we studied hydrogen hydrogen transport near a blunting crack tip with the use of a lattice chemical potential boundary condition, and compared our simulations with those of Sofronis and McMeeking (1989) and Krom et al. (1999) where the authors used a lattice hydrogen concentration boundary condition. We have argued that it is important to use a constant lattice chemical potential boundary condition, as oppose to a constant lattice hydrogen concentration boundary condition, in modeling problems involving a metal specimen exposed to a hydrogen atmosphere at a particular partial pressure and temperature.

Secondly, we numerically studied the plane-strain tensile deformation of metal specimens that are either hydrogen-charged or uncharged prior to being mechanically deformed. We have shown that although the hydrogen atmosphere surrounding the specimen is not changing, the hydrogen concentration within the specimen can significantly increase. This increase is driven both by an increase in the lattice hydrogen concentration, due to the volumetric elastic strains, and an increase in the trapped hydrogen concentration, due to the increase in the number of available trapping sites. Understanding and modeling the increase of hydrogen within a specimen as it is mechanically deformed, while exposed to hydrogen, is crucial in the future development of theories which seek to couple the mechanical response of the material with the hydrogen distribution within it. These numerical studies also illustrated the different patterns of localized plastic deformation that can form when the hydrogen concentration within the material induces plastic softening.

Thirdly, we numerically studied U-notched specimens deformed in three-point bending that are either hydrogen-charged or uncharged prior to being mechanically deformed. Our results are in good qualitative agreement with those of Lee et al. (1977, 1979), in that hydrogen-charging results in localized plastic deformation near the north in the form of multiple shear bands.

5.2 Future work

While much has been accomplished towards the goal of being able to model hydrogen-embrittlement related failures in metallic components, much more remains to be done. Some specific outstanding issues which are left for future work are discussed below:

- The theory presented in this work does not involve a model for material damage. To achieve the goal of modeling hydrogen-embrittlement related failure in metallic components the theory presented thus far needs to be enhanced with a damage model which accounts for damage due to the presence of hydrogen.

- Further work needs to be performed to address the microscopic-scale phenomena that might be pertinent to modeling hydrogen-embrittlement related failures in metallic components. Specifically, the theory can be enhanced to account for (i) crystal plasticity and localization of plastic deformation within the grains, (ii) grain-boundary decohesion enhanced by the presence of hydrogen; and (iii) cleavage within the grains promoted by hydrogen.

- Although our theoretical development, and numerical implementation, is not restricted to isothermal conditions, we have thus far only considered isothermal numerical simulations. Future work needs to consider the effect of thermal variations on the mechanical response of metallic components as well as on the diffusion of hydrogen within the component.

- A complete set of macroscopic experiments is required in order to better understand the effect of hydrogen on the plastic deformation and damage of a specific metal. Specifically, we propose that tension experiments on round-bar specimens need to be performed within a controlled hydrogen atmosphere at varying hydrogen pressures and temperatures, as well as varying strain-rates. The experiments can then be used to calibrate the material parameters of the model.

- Once the theory has been calibrated to a particular metal system, experiments need to be performed to validate the predictive capability of the theoretical model and its corresponding numerical implementation.

Bibliography

L. Anand. A thermo-mechanically-coupled theory accounting for hydrogen diffusion and large elastic-viscoplastic deformations of metals. *International Journal of Solids and Structures*, 48: 962–971, 2011.

L. Anand and M. E. Gurtin. A theory of amorphous solids undergoing large deformations, with applications to polymeric glasses. *International Journal of Solids and Structures*, 40:1465–1487, 2003.

L. Anand, O. Aslan, and S. A. Chester. A large-deformation gradient theory for elastic-plastic materials: strain softening and regularization of shear bands. *Interntional Journal of Plasticity*, 30-31:116–143, 2012.

P. Arkins and J. de Paula. *Physical Chemistry*. W.H. Freeman and Company, 9 edition, 2010.

S. A. Chester. *Mechanics of amorphous polymers and polymer gels*. PhD thesis, Massachusetts Institute of Technology, 2011.

M. Dadfarnia, B.P. Somerday, P. Sofronis, I.M. Robertson, and D. Stalheim. Interaction of hydrogen transport and material elastoplasticity in pipeline steels. *Journal of Pressure Vessel Technology*, 131, 2009.

M. Dadfarnia, P. Novak, D.C. Ahn, J.B. Liu, P. Sofronis, D. D. Johnson, and I.M. Robertson. Recent advances in the study of structural materials compatibility with hydrogen. *Advanced Materials*, 22:1128–1135, 2010.

S. Forest. Micromorphic approach for gradient elasticity, viscoplasticity, and damage. *Journal of Engineering Mechanics*, 135:117–131, 2009.

W.F. Gale and T.C. Totemeier, editors. *Smithells Metals Reference Book*. Butterworth-Heinemann, eight edition, 2004.

M. E. Gurtin. Generalized ginzburg-landau and cahn-hillard equations based on a microforce balance. *Physica D*, 92:178–192, 1996.

M. E. Gurtin. On the plasticity of single crystals" free energy, microscopic forces, plastic strain gradients. *Journal of the Mechanics and Physics of Solids*, 48:989–1036, 2000.

M. E. Gurtin. A gradient theory of single-crystal viscoplasticity that accounts for geometrically necessary dislocations. *Journal of the Mechanics and Physics of Solids*, 50:5–32, 2002.

M. E. Gurtin and L. Anand. The decomposition $\mathbf{F}=\mathbf{F}^e\mathbf{F}^p$, material symmetry, and plastic irrotationality for solids that are isotropic-viscoplastic or amorphous. *International Journal of Plasticity*, 21:1686–1719, 2005.

M. E. Gurtin and L. Anand. Thermodynamics applied to gradient theories involving the accumulated plastic strain; the theories of Aifantis and Fleck and Hutchinson and their generalizations. *Journal of Mechanics and Physics of Solids*, 57:405–421, 2009.

M. E. Gurtin, E. Fried, and L. Anand. *The Mechanics and Thermodynamics of Continua*. Cambridge University Press, 2010.

J. P. Hirth. Effects of hydrogen on the properties of iron and steel. *Metalurgical Transactions A*, 11A:861–890, 1980.

A.H.M. Krom and A. Bakker. Hydrogen trapping models in steel. *Metalurgical and Materials Transactions B*, 31B:1475–1482, 2000.

A.H.M. Krom, R.W.J. Koers, and A. Bakker. Modelling hydrogen-induced cracking in steel using a coupled diffusion stress finite element analysis. *Int. J. Pres. Ves. & Piping*, 72:139–147, 1997.

A.H.M. Krom, R.W.J. Koers, and A. Bakker. Hydrogen transport near a blunting crack tip. *Journal of the Mechanics and Physics of Solids*, 47:971–992, 1999.

L. Kröner. Allgemeine kontinuumstheorie der versetzungen und eigenspannungen. *Archive for Rational Mechanics and Analysis*, 4:273–334, 1960.

E.H. Lee. Elastic plastic deformation at finite strain. *ASME Journal of Applied Mechanics*, 36:1–6, 1969.

T.D. Lee, T. Goldenberg, and J.P. Hirth. Hydrogen and plastic instability in deformed, spheroidized 1090 steel. In D.M.R. Taplin, editor, *Fracture*, volume 2A, pages 243–248, 1977.

T.D. Lee, T. Goldenberg, and J.P. Hirth. Effect of hydrogen on fracture of u-notched bend specimens of spheroidized aisi 1095 steel. *Metallurgical Transactions A*, 10A:199–208, 1979.

J. Lufrano and P. Sofronis. Hydrogen transport and large strain elastoplasticity near a notch in alloy x-750. *Engineering Fracture Mechanics*, 59(6):827–845, 1998.

A. McNabb and P.K. Foster. A new analysis of the diffuion of hydrogen in iron and ferritic steels. *Transaction of the Metallurgical Society of AIME*, 227:618–627, 1963.

P. Novak, R. Yuan, B.P. Somerday, P. Sofronis, and R.O. Ritchie. A statistical, physical-based, micro-mechanical model of hydrogen-induced intergranular fracture in steel. *Journal of the Mechanics and Physics of Solids*, 58:206–226, 2010.

R. A. Oriani. The diffusion and trapping of hydrogen in steel. *Acta Metallurgica*, 18:147–157, 1970.

A. Ramasubramaniam, M. Itakura, M. Ortiz, and E.A. Carter. Effect of atomic scale plasticity on hydrogen diffusion in iron: Quantum mechanically informed and on-the-fly kinetic monte carlo simulations. *Journal of Materials Research*, 23:2757–2773, 2008.

C. San Marchi, B.P. Somerday, and S.L. Robinson. Permeability, solubility and diffusivity of hydrogen isotopes in stainless steels at high gas pressure. *International Journal of Hydrogen Energy*, 32:100–116, 2007.

S. Serebrinsky, E.A. Carter, and M. Ortiz. A quantum-mechanically informed continuum model of hydrogen embrittlement. *Journal of the Mechanics and Physics of Solids*, 52:2403–2430, 2004.

P. Sofronis and R. M. McMeeking. Numerical analysis of hydrogen transport near a blunting crack tip. *J. Mech. Phys. Solids*, 37(3):317–350, 1989.

A. Taha and P. Sofronis. A micromechanics approach to the study of hydrogen transport and embrittlement. *Engineering Fracture Mechanics*, 68:803–837, 2001.

G. Weber and L. Anand. Finite deformation constitutive equations and a time integration procedure for isotropic, hyperelastic-viscoplastic solids. *Computer Methods in Applied Mechanics and Engineering*, 79:173–202, 1990.

J. Zheng, Liu X, P. Xu, P. Liu, Y. Zhao, and J. Yang. Development of high pressure gaseous hydrogen storage technologies. *International Journal of Hydrogen Energy*, 37:1048–1057, 2011.

A. Züttel, A. Remhof, A. Borgschulte, and O. Friedrichs. Hydrogen: the future energy carrier. *Philosophical Transactions of The Royal Society A*, 368:3329–3342, 2010.

Appendix A

Non-equilibrium trapping of hydrogen

The purpose of this appendix is to illustrate how our theory provides a framework in which to model "non-equilibrium" trapping, that is we do not make the specific constitutive assumption (2.202), and assume that

$$\mu_L \quad \text{is not always equal to} \quad \mu_T \quad \text{and hence} \quad \mathcal{F} \quad \text{can be non-zero,} \tag{A.1}$$

and thus that the chemical potentials of the two species are not always in equilibrium.

Recall from Section 2.11.2, equation (2.199), that the time rate of change of trapped hydrogen is constrained by

$$\mathcal{F}\,\dot{C}_T \geq 0, \quad \text{with} \quad \mathcal{F} \overset{\text{def}}{=} \mu_L - \mu_T \tag{A.2}$$

and we are left with the task of determining the specific constitutive form for $\dot{C}_T$. We assume a simple relationship for $\dot{C}_T$ which does not directly depend on $\mathcal{F}$:

$$\dot{C}_T = \begin{cases} \mathcal{R}_{\mathrm{C}} & \text{if} \quad \mathcal{F} > 0, \\ -\mathcal{R}_{\mathrm{R}} & \text{if} \quad \mathcal{F} < 0, \\ 0 & \text{if} \quad \mathcal{F} = 0, \end{cases} \tag{A.3}$$

where the *capture rate* $\mathcal{R}_{\mathrm{C}} \geq 0$ is the rate at which hydrogen transforms from lattice sites to trapped sites and the *release rate* $\mathcal{R}_{\mathrm{R}} \geq 0$ is the rate at which hydrogen transforms from trapped sites to lattice sites. Note that (A.3) always satisfies (A.2).

Following McNabb and Foster (1963), we assume the capture rate $\mathcal{R}_{\mathrm{C}}$ is proportional to the site fraction of lattice hydrogen (i.e. the availability of hydrogen) and to the molar number of trap sites available (a greater number of traps should increase the probability that the random motion of hydrogen within the lattice results in hydrogen being trapped). The release rate $\mathcal{R}_{\mathrm{R}}$ is proportional to the trapped hydrogen concentration and the site fraction of unfilled lattice sites.

Consider now the energy landscape shown in Fig. A-1, where Q is the activation energy for jumping between normal interstitial lattice sites, and W_B is the trap binding energy. We may model trapping as an energy well, corresponding to a microstructural defect in the metal lattice,

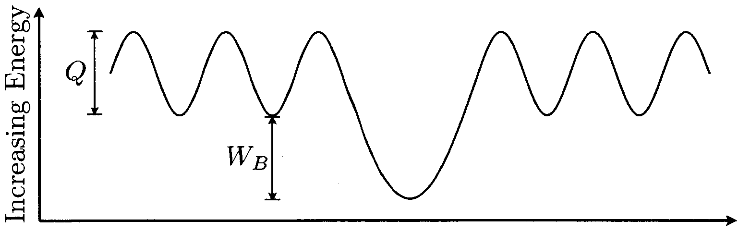

Figure A-1: Schematic of the energy landscape for hydrogen trapping.

surrounded by a region of smaller wells, corresponding to the metal lattice, which govern the standard diffusion process.

Combining the aforementioned ideas the capture and release rates $\mathcal{R}_\mathrm{C}$ and $\mathcal{R}_\mathrm{R}$ are assumed to be given by

$$\mathcal{R}_\mathrm{C} = \theta_L(1-\theta_T)N_T\nu\exp\left(\frac{-Q}{R\vartheta}\right) \tag{A.4}$$

$$\mathcal{R}_\mathrm{R} = \theta_T N_T(1-\theta_L)\nu\exp\left(\frac{W_B-Q}{R\vartheta}\right) \tag{A.5}$$

where ν is the vibration frequency of the hydrogen atoms (presumed to be the same for hydrogen residing in normal interstitial lattice sites and hydrogen residing in trapping sites). From (A.4) it is clear that $\mathcal{R}_\mathrm{C} = 0$ whenever the trap sites are saturated or all lattice hydrogen has been consumed and from (A.5) that $\mathcal{R}_\mathrm{R} = 0$ whenever the trap sites are empty or all lattice sites are saturated, thus effectively modeling saturable trap sites as well as a saturable lattice.

Finally, combining equations (A.4) and (A.5) with (A.3), gives that the time rate of change of trapped hydrogen is

$$\dot{C}_T = \begin{cases} \theta_L(1-\theta_T)N_T\nu\exp\left(\dfrac{-Q}{R\vartheta}\right) & \text{if } \mathcal{F} > 0, \\ -\theta_T N_T(1-\theta_L)\nu\exp\left(\dfrac{W_B-Q}{R\vartheta}\right) & \text{if } \mathcal{F} < 0, \\ 0 & \text{if } \mathcal{F} = 0. \end{cases} \tag{A.6}$$

If the thermodynamic force $\mathcal{F}$ is given by equation (2.201), hydrogen trapping will proceed until it has reached the same equilibrium condition between lattice hydrogen and trapped hydrogen which is used in Section 2.11.2, that is

$$\frac{\theta_T}{1-\theta_T} = \frac{\theta_L}{1-\theta_L}K_T, \tag{A.7}$$

however it will reach this equilibrium condition at a finite trapping rate. With the framework presented here one may chose constitutive equations which result in a thermodynamic force $\mathcal{F}$ different than that shown in (2.201), and thus may be used to model hydrogen traps which do not obey the equilibrium relation (A.7), for example non-saturable traps.

Appendix B

Details on the numerical implementation

Introduction

Following the framework developed by Chester (2011), in this Appendix we present the details of our numerical implementation for the solution of the transient coupled mechanical deformation, hydrogen diffusion, heat conduction, and strain-gradient regularization theory presented in the previous chapters. ABAQUS requires the computation of a 'Residual' vector and a 'Stiffness' matrix for each solution variable in the theory, in order to solve the coupled equations through a Newton-Rhapson method.

In sections B.1 through B.4 we calculate the 'Residual' and 'Stiffness' for each of the solution variables in our theory. In Section B.5 we present the time integration procedure used to update the plastic distortion $\mathbf{F}^p$, and in section B.6 we complete the 'Stiffness' matrix for the displacement solution variables which requires first a development of the time integration procedure for the plastic distortion.

B.1 Variational formulation of the macroscopic force balance

The displacement solution variables are governed by the partial differential equation for the balance of momentum (2.239), the strong form of which, in the *current* configuration, along with appropriate boundary conditions is given by

$$\left.\begin{aligned} \mathrm{div}\mathbf{T} + \mathrm{b} = \mathbf{0} &\quad \text{on} \quad \mathrm{B}_t, \\ \chi = \breve{\chi} &\quad \text{on} \quad \mathcal{S}_1, \\ \mathbf{Tn} = \breve{\mathrm{t}} &\quad \text{on} \quad \mathcal{S}_2, \end{aligned}\right\} \tag{B.1}$$

where B_t denotes the body in the current deformed configuration, on the deformed surface $\mathcal{S}_1$ we prescribe displacements, and on the deformed surface $\mathcal{S}_2$ we prescribe surface tractions. To find the weak form of (B.1) we multiply by a test function $\mathbf{w}$ and integrate over the body

$$0=\int_{\mathrm{B}_t}(\mathbf{w}\cdot\mathrm{div}\mathbf{T}+\mathbf{w}\cdot\mathbf{b})\,dV \tag{B.2}$$

which integrating by parts yields

$$0=\int_{\mathrm{B}_t}(-\mathrm{grad}\,\mathbf{w}\colon\mathbf{T}+\mathbf{w}\cdot\mathbf{b})\;dV+\int_{\partial\mathrm{B}_t}(\mathbf{w}\cdot\mathbf{Tn})\,dA, \tag{B.3}$$

and using $(\mathrm{B}.1)_3$ we have

$$0=\int_{B_t}(-\mathrm{grad}\,\mathbf{w}:\mathbf{T}+\mathbf{w}\cdot\mathbf{b})\,dV+\int_{\mathcal{S}_1}(\mathbf{w}\cdot\breve{\mathbf{t}})\,dA. \tag{B.4}$$

The body is approximated using finite elements $\mathrm{B}_t=\sum\mathrm{B}_t^e$ and the trial solution for the displacement vector is interpolated inside each element by

$$\mathbf{u}=\sum_A N^A\mathbf{u}^A \tag{B.5}$$

with the index $A=1,2,...$ denoting the nodes of the element, $\mathbf{u}^A$ denoting the nodal displacement vector, and N^A the shape functions. We employ a standard Galerking approach, in that the weighting field is interpolated by the same shape functions, such that

$$\mathbf{w}=\sum_A N^A\mathbf{w}^A. \tag{B.6}$$

This yields the element-level relation

$$0=\int_{\mathrm{B}_t^e}(-\mathbf{w}^A\cdot(\mathbf{T}\mathrm{grad}\,N^A+\mathbf{w}^A\cdot\mathbf{b}N^A)\,dV+\int_{\mathcal{S}_1^e}(N^A\mathbf{w}^A\cdot\breve{\mathbf{t}})\,dA \tag{B.7}$$

which must hold for all $\mathbf{w}^A$. Therefore, we define the element level displacement residual

$$\mathbf{R}_{\mathbf{u}}^A=\int_{\mathrm{B}_t^e}(N^A\mathbf{b}-\mathbf{T}\mathrm{grad}\,N^A)\,dV+\int_{\mathcal{S}_1^e}(N^A\breve{\mathbf{t}})\,dA, \tag{B.8}$$

which in index notation is

$$R_{u_i}^A=\int_{\mathrm{B}_t^e}\left(N^Ab_i-T_{ij}\frac{\partial N^A}{\partial x_j}\right)\,dV+\int_{\mathcal{S}_1^e}(N^A\breve{t}_i)\,dA. \tag{B.9}$$

The element stiffness is given by

$$\mathbf{K}_{\mathbf{uu}}^{AB}=-\frac{\partial\mathbf{R}_{\mathbf{u}}^A}{\partial\mathbf{u}^B},\quad\text{or in index notation}\quad K_{u_iu_k}^{AB}=-\frac{\partial R_{u_i}}{\partial u_k^B}. \tag{B.10}$$

Using the residual defined above we have

$$K^{AB}_{u_i u_k} = \int_{\mathrm{B}^e_t} \frac{\partial N^A}{\partial x_j}\frac{\partial T_{ij}}{\partial u^B_k}\, dV - \int_{\mathcal{S}^e_1} N^A N^B \frac{\partial \breve{t}}{\partial u_k}\, dA. \tag{B.11}$$

Furthermore,

$$\frac{\partial T_{ij}}{\partial u^B_k} = \frac{\partial T_{ij}}{\partial F_{mn}}\frac{\partial F_{mn}}{\partial u^B_k} \tag{B.12}$$

and since

$$F_{mn} = \delta_{mn} + \frac{\partial N^A}{\partial x_n} u^A_m, \quad \text{and} \quad \frac{\partial F_{mn}}{\partial u^B_k} = \frac{\partial N^B}{\partial x_n}\delta_{mk} \tag{B.13}$$

we arrive at

$$K^{AB}_{u_i u_k} = \int_{\mathrm{B}^e_t} \frac{\partial N^A}{\partial x_j}\frac{\partial T_{ij}}{\partial F_{kn}}\frac{\partial N^B}{\partial x_n}\, dV - \int_{\mathcal{S}^e_1} N^A N^B \frac{\partial \breve{t}}{\partial u_k}\, dA. \tag{B.14}$$

In section B.6 we present a detail derivation on how to approximately compute the term $\partial T_{ij}/\partial F_{kn}$ in the stiffness matrix.

B.2 Variational formulation for the balance of lattice chemical potential

The lattice chemical potential solution variable, μ_L, is governed by the local balance of hydrogen concentration (2.240), the strong form of which along with appropriate boundary conditions is given by

$$\left.\begin{aligned}
D^*\frac{C_L}{R\vartheta}\dot{\mu}_L &= \mathrm{Div}\,(m_L\nabla\mu_L) - D^*\frac{C_L}{R\vartheta}(3K\beta)\mathrm{tr}\,\dot{\mathbf{E}}^e - \theta_T\frac{dN_T}{d\bar{\epsilon}^p}\dot{\bar{\epsilon}}^p & & \\
&+ \left(D^*C_L\ln\frac{C_L}{N_L} + \frac{C_T(1-\theta_T)W_B}{R\vartheta}\right)\frac{\dot{\vartheta}}{\vartheta} & \text{in} \quad & \mathrm{B} \\
\mu_L &= \breve{\mu}_L & \text{on} \quad & \mathcal{S}_{\mu_L} \\
-m_L(\nabla\mu_L)\cdot\mathbf{n}_{\mathrm{R}} &= \breve{j}_L & \text{on} \quad & \mathcal{S}_{j_L}
\end{aligned}\right\} \tag{B.15}$$

where

$$D^* = 1 + \frac{C_T(1-\theta_T)}{C_L} \quad \text{and} \quad m_L = \frac{D_L C_L}{R\vartheta}, \tag{B.16}$$

with $D_L(\vartheta)$ the lattice diffusivity, K the bulk modulus, β the coefficient of chemical expansion, R the gas constant, W_B the trap binding energy, N_L the molar number of lattice sites per unit reference volume, and $N_T = \hat{N}_T(\bar{\epsilon}^p)$ the molar number of trap sites per unit reference volume. Further, on the surface $\mathcal{S}_{\mu_L}$ we prescribe the lattice chemical potential, and on the surface $\mathcal{S}_{j_L}$ the flux of lattice hydrogen. To find the weak form of (B.15) we multiply by a test function w and integrate over the body

$$0 = \int_{\mathrm{B}} w \left[D^* \frac{C_L}{R\vartheta} \left(\dot{\mu}_L - R\dot{\vartheta} \ln \frac{C_L}{N_L} + (3K\beta) \mathrm{tr}\, \dot{\mathbf{E}}^e \right) + \theta_T \frac{dN_T}{d\bar{\epsilon}^p} \dot{\bar{\epsilon}}^p - \frac{C_T(1-\theta_T)W_B}{R\vartheta} \frac{\dot{\vartheta}}{\vartheta} \right] dV_{\mathrm{R}} - \int_{\mathrm{B}} w \mathrm{Div} \left(m_L \nabla \mu_L \right) dV_{\mathrm{R}} \tag{B.17}$$

then using the identity

$$\alpha \mathrm{Div}\left(\mathbf{u}\right) = \mathrm{Div}\left(\alpha \mathbf{u}\right) - \nabla \alpha \cdot \mathbf{u} \tag{B.18}$$

we obtain

$$0 = \int_{\mathrm{B}} w \left[D^* \frac{C_L}{R\vartheta} \left(\dot{\mu}_L - R\dot{\vartheta} \ln \frac{C_L}{N_L} + (3K\beta) \mathrm{tr}\, \dot{\mathbf{E}}^e \right) + \theta_T \frac{dN_T}{d\bar{\epsilon}^p} \dot{\bar{\epsilon}}^p - \frac{C_T(1-\theta_T)W_B}{R\vartheta} \frac{\dot{\vartheta}}{\vartheta} \right] dV_{\mathrm{R}} + \int_{\mathrm{B}} \left[\nabla w \cdot m_L \nabla \mu_L - \mathrm{Div} \left(w m_L \nabla \mu_L \right) \right] dV_{\mathrm{R}} \tag{B.19}$$

and using the divergence theorem

$$0 = \int_{\mathrm{B}} w \left[D^* \frac{C_L}{R\vartheta} \left(\dot{\mu}_L - R\dot{\vartheta} \ln \frac{C_L}{N_L} + (3K\beta) \mathrm{tr}\, \dot{\mathbf{E}}^e \right) + \theta_T \frac{dN_T}{d\bar{\epsilon}^p} \dot{\bar{\epsilon}}^p - \frac{C_T(1-\theta_T)W_B}{R\vartheta} \frac{\dot{\vartheta}}{\vartheta} \right] dV_{\mathrm{R}} + \int_{\mathrm{B}} \nabla w \cdot m_L \nabla \mu_L \, dV_{\mathrm{R}} - \int_{\partial \mathrm{B}} w (m_L \nabla \mu_L) \cdot \mathbf{n}_{\mathrm{R}} \, dA_{\mathrm{R}}. \tag{B.20}$$

Finally, applying the definition of the prescribed flux boundary condition (B.15)$_3$ yields

$$0 = \int_{\mathrm{B}} w \left[D^* \frac{C_L}{R\vartheta} \left(\dot{\mu}_L - R\dot{\vartheta} \ln \frac{C_L}{N_L} + (3K\beta) \mathrm{tr}\, \dot{\mathbf{E}}^e \right) + \theta_T \frac{dN_T}{d\bar{\epsilon}^p} \dot{\bar{\epsilon}}^p - \frac{C_T(1-\theta_T)W_B}{R\vartheta} \frac{\dot{\vartheta}}{\vartheta} \right] dV_{\mathrm{R}} + \int_{\mathrm{B}} \nabla w \cdot m_L \nabla \mu_L \, dV_{\mathrm{R}} + \int_{\mathcal{S}_{j_L}} w \hat{\jmath}_L \, dA_{\mathrm{R}}. \tag{B.21}$$

The body is approximated using finite elements $\mathrm{B} = \sum \mathrm{B}^e$ and the trial solution for the lattice chemical potential is interpolated inside each element by

$$\mu_L = \sum_A N^A \mu_L^A, \tag{B.22}$$

with the index $A = 1, 2, ...$ denoting the nodes of the element, μ_L^A denoting the nodal lattice chemical potential, and N^A the shape functions. We employ a standard Galerkin approach, in that the weighting field is interpolated by the same shape functions, such that

$$w = \sum_A N^A w^A. \tag{B.23}$$

This yields the element-level relation

$$0 = \int_{\mathrm{B}^e} w^A N^A \left[D^* \frac{C_L}{R\vartheta} \left(\dot{\mu}_L - R\dot{\vartheta} \ln \frac{C_L}{N_L} + (3K\beta) \mathrm{tr}\, \dot{\mathbf{E}}^e \right) + \theta_T \frac{dN_T}{d\bar{\epsilon}^p} \dot{\bar{\epsilon}}^p - \frac{C_T (1-\theta_T) W_B}{R\vartheta} \frac{\dot{\vartheta}}{\vartheta} \right] dV_{\mathrm{R}}$$

$$+ \int_{\mathrm{B}^e} w^A \nabla N^A \cdot m_L \nabla \mu_L \, dV_{\mathrm{R}} + \int_{\mathcal{S}^e_{j_L}} w^A N^A \hat{j}_L \, dA_{\mathrm{R}} \tag{B.24}$$

which must hold for all w^A. Therefore, we define the element level residual for the lattice chemical potential as

$$R^A_{\mu_L} = \int_{\mathrm{B}^e} N^A \left[D^* \frac{C_L}{R\vartheta} \left(\dot{\mu}_L - R\dot{\vartheta} \ln \frac{C_L}{N_L} + (3K\beta) \mathrm{tr}\, \dot{\mathbf{E}}^e \right) + \theta_T \frac{dN_T}{d\bar{\epsilon}^p} \dot{\bar{\epsilon}}^p - \frac{C_T (1-\theta_T) W_B}{R\vartheta} \frac{\dot{\vartheta}}{\vartheta} \right] dV_{\mathrm{R}}$$

$$+ \int_{\mathrm{B}^e} \nabla N^A \cdot m_L \nabla \mu_L \, dV_{\mathrm{R}} + \int_{\mathcal{S}^e_{j_L}} N^A \hat{j}_L \, dA_{\mathrm{R}}. \tag{B.25}$$

The element stiffness is defined by

$$K^{AB}_{\mu_L \mu_L} = - \frac{\partial R^A_{\mu_L}}{\partial \mu^B_L} \tag{B.26}$$

which using the residual defined in (B.25) is given by

$$K^{AB}_{\mu_L \mu_L} = - \int_{\mathrm{B}^e} N^A \left[\frac{\partial \mu_L}{\partial \mu^B_L} \frac{\partial}{\partial \mu_L} \left(D^* \frac{C_L}{R\vartheta} \right) \left(\dot{\mu}_L - R\dot{\vartheta} \ln \frac{C_L}{N_L} + (3K\beta) \mathrm{tr}\, \dot{\mathbf{E}}^e \right) \right.$$

$$\left. + \left(D^* \frac{C_L}{R\vartheta} \right) \frac{\partial \mu_L}{\partial \mu^B_L} \frac{\partial}{\partial \mu_L} \left(\dot{\mu}_L - R\dot{\vartheta} \ln \frac{C_L}{N_L} + (3K\beta) \mathrm{tr}\, \dot{\mathbf{E}}^e \right) \right] dV_{\mathrm{R}}$$

$$- \int_{\mathrm{B}^e} N^A \left[\frac{1}{N_T} \frac{\partial C_T}{\partial C_L} \frac{\partial C_L}{\partial \mu_L} \frac{\partial \mu_L}{\partial \mu^B_L} \frac{dN_T}{d\bar{\epsilon}^p} \dot{\bar{\epsilon}}^p - \left(\frac{\partial C_T}{\partial C_L} - 2\theta_T \frac{\partial C_T}{\partial C_L} \right) \frac{\partial C_L}{\partial \mu_L} \frac{\partial \mu_L}{\partial \mu^B_L} \frac{W_B}{R\vartheta} \frac{\dot{\vartheta}}{\vartheta} \right] dV_{\mathrm{R}}$$

$$- \int_{\mathrm{B}^e} \left[\nabla N^A \cdot \frac{\partial m_L}{\partial \mu_L} \frac{\partial \mu_L}{\partial \mu^B_L} \nabla \mu_L + \nabla N^A \cdot m_L \frac{\partial \mu_L}{\partial \mu^B_L} \frac{\partial}{\partial \mu_L} \frac{\partial \mu_L}{\partial \mathbf{X}} \right] dV_{\mathrm{R}}$$

$$- \int_{\mathcal{S}^e_{j_L}} N^A \frac{\partial \mu_L}{\partial \mu^B_L} \frac{\partial \hat{j}_L}{\partial \mu_L} \, dA_{\mathrm{R}}, \tag{B.27}$$

and can be further simplified to

$$
\begin{aligned}
K^{AB}_{\mu_L\mu_L} = &-\int_{\mathrm{B}^e} N^A N^B \left[\frac{\partial}{\partial\mu_L}\left(D^*\frac{C_L}{R\vartheta}\right)\left(\dot{\mu}_L - R\dot{\vartheta}\ln\frac{C_L}{N_L} + (3K\beta)\mathrm{tr}\,\dot{\mathbf{E}}^e\right) + D^*\frac{C_L}{R\vartheta}\left(\frac{\partial\dot{\mu}_L}{\partial\mu_L} - \frac{\dot{\vartheta}}{\vartheta}\right)\right] dV_{\mathrm{R}} \\
&- \int_{\mathrm{B}^e} N^A N^B \frac{\partial C_T}{\partial C_L}\frac{\partial C_L}{\partial\mu_L}\left[\frac{1}{N_T}\frac{dN_T}{d\bar{\epsilon}^p}\dot{\bar{\epsilon}}^p - (1-2\theta_T)\frac{W_B}{R\vartheta}\frac{\dot{\vartheta}}{\vartheta}\right] dV_{\mathrm{R}} \\
&- \int_{\mathrm{B}^e}\left[\frac{\partial m_L}{\partial\mu_L}N^B\nabla N^A\cdot\nabla\mu_L + \nabla N^A\cdot m_L\nabla N^B\right] dV_{\mathrm{R}} \\
&- \int_{\mathcal{S}^e_{j_L}} N^A N^B \frac{\partial\hat{j}_L}{\partial\mu_L}\, dA_{\mathrm{R}}
\end{aligned}
\tag{B.28}
$$

where, using (B.16)

$$
D^*\frac{C_L}{R\vartheta} = \frac{C_L + C_T(1-\theta_T)}{R\vartheta},
\tag{B.29}
$$

using (B.29), (2.206) and (2.212)

$$
\frac{\partial}{\partial\mu_L}\left(D^*\frac{C_L}{R\vartheta}\right) = \frac{C_L}{(R\vartheta)^2}\left(1 + \frac{C_T}{C_L}(1-2\theta_T)(1-\theta_T)\right),
\tag{B.30}
$$

using (2.206) and (2.212)

$$
\frac{\partial C_T}{\partial C_L}\frac{\partial C_L}{\partial\mu_L} = \frac{C_T}{R\vartheta}(1-\theta_T),
\tag{B.31}
$$

and using (B.16) and (2.212)

$$
\frac{\partial m_L}{\partial\mu_L} = \frac{D_L C_L}{(R\vartheta)^2}.
\tag{B.32}
$$

Finally using equations (B.29) through (B.32) the element stiffness (B.28) may be written as

$$
\begin{aligned}
K^{AB}_{\mu_L\mu_L} = &-\int_{\mathrm{B}^e} N^A N^B \left[\frac{C_L}{(R\vartheta)^2}\left(1 + \frac{C_T}{C_L}(1-2\theta_T)(1-\theta_T)\right)\left(\dot{\mu}_L - R\dot{\vartheta}\ln\frac{C_L}{N_L} + (3K\beta)\mathrm{tr}\,\dot{\mathbf{E}}^e\right)\right. \\
&\qquad\left. + \left(\frac{C_L + C_T(1-\theta_T)}{R\vartheta}\right)\left(\frac{\partial\dot{\mu}_L}{\partial\mu_L} - \frac{\dot{\vartheta}}{\vartheta}\right)\right] dV_{\mathrm{R}} \\
&- \int_{\mathrm{B}^e} N^A N^B \left(\frac{C_T}{R\vartheta}(1-\theta_T)\right)\left[\frac{1}{N_T}\frac{dN_T}{d\bar{\epsilon}^p}\dot{\bar{\epsilon}}^p - (1-2\theta_T)\frac{W_B}{R\vartheta}\frac{\dot{\vartheta}}{\vartheta}\right] dV_{\mathrm{R}} \\
&- \int_{\mathrm{B}^e} \frac{D_L C_L}{R\vartheta}\left[\frac{1}{R\vartheta}N^B\nabla N^A\cdot\nabla\mu_L + \nabla N^A\cdot\nabla N^B\right] dV_{\mathrm{R}} \\
&- \int_{\mathcal{S}^e_{j_L}} N^A N^B \frac{\partial\hat{j}_L}{\partial\mu_L}\, dA_{\mathrm{R}}.
\end{aligned}
\tag{B.33}
$$

The time rate of change of μ_L, ϑ, and $\operatorname{tr}\mathbf{E}^e$ are computed through a backward-Euler method such that

$$\dot{\mu}_L = \frac{\mu_{L,n+1} - \mu_{L,n}}{\Delta t}, \quad \frac{\partial \dot{\mu}_L}{\partial \mu_L} = \frac{1}{\Delta t}, \quad \dot{\vartheta} = \frac{\vartheta_{n+1} - \vartheta_n}{\Delta t}, \quad \text{and} \quad \operatorname{tr}\dot{\mathbf{E}}^e = \frac{\operatorname{tr}{\mathbf{E}^e}_{n+1} - \operatorname{tr}{\mathbf{E}^e}_n}{\Delta t} \tag{B.34}$$

with time discretized as $t_{n+1} = t_n + \Delta t$.

B.3 Variational formulation for the transient heat equation

The temperature solution variable is governed by the partial differential equation for the temperature (2.242), the strong form of which along with corresponding boundary conditions is given by

$$\left.\begin{array}{rcll} c\dot{\vartheta} & = & \operatorname{Div}(k\nabla\vartheta) + \bar{q}_{\mathrm{R}} & \text{in} \quad \mathrm{B} \\ \vartheta & = & \breve{\vartheta} & \text{on} \quad \mathcal{S}_\vartheta \\ -k\nabla\vartheta \cdot \mathbf{n}_{\mathrm{R}} & = & \breve{q}_{\mathrm{R}} & \text{on} \quad \mathcal{S}_q \end{array}\right\} \tag{B.35}$$

with ϑ the temperature, $c(\vartheta)$ the specific heat, $k(\vartheta)$ the thermal conductivity, and $\bar{q}_{\mathrm{R}}$ the scalar heat generation terms. Also, on the surface $\mathcal{S}_\vartheta$ we prescribe temperature, and on the surface $\mathcal{S}_q$ the heat flux. The term $\bar{q}_{\mathrm{R}}$ includes all scalar heat generation terms, from (2.242) it is given by

$$\begin{aligned} \bar{q}_{\mathrm{R}} = q_{\mathrm{R}} + (Y_{\mathrm{conv}} + Z(\bar{e}^p - e^p))\dot{\bar{e}}^p + \frac{1}{2}\vartheta\frac{\partial \mathbf{T}^e}{\partial\vartheta} : \dot{\mathbf{C}}^e \\ + R\vartheta \ln\left(\frac{C_L}{N_L}\right)\dot{C}_L + m_L|\nabla\mu_L|^2 + R\vartheta\ln\left(\frac{\theta_T}{1-\theta_T}\right)\dot{C}_T. \end{aligned} \tag{B.36}$$

In this numerical implementation we neglect all scalar heat generation terms expect those due to plastic working such that

$$\bar{q}_{\mathrm{R}} = (Y_{\mathrm{conv}} + Z(\bar{e}^p - e^p))\dot{\bar{e}}^p. \tag{B.37}$$

To find the weak form of (B.35) we multiply by a test function w and integrate over the body

$$0 = \int_{\mathrm{B}} w\left[c\dot{\vartheta} - \operatorname{Div}(k\nabla\vartheta) - \bar{q}_{\mathrm{R}}\right] dV_{\mathrm{R}} \tag{B.38}$$

then using the identity

$$\operatorname{Div}(\alpha\mathbf{u}) = \alpha\operatorname{Div}(\mathbf{u}) + \nabla\alpha\cdot\mathbf{u} \tag{B.39}$$

we obtain

$$0 = \int_{\mathrm{B}} \left[w(c\dot{\vartheta} - \bar{q}_{\mathrm{R}}) - \operatorname{Div}(wk\nabla\vartheta) + \nabla w\cdot k\nabla\vartheta\right] dV_{\mathrm{R}} \tag{B.40}$$

and using the divergence theorem

$$0 = \int_{\mathrm{B}} \left[w(c\dot{\vartheta} - \bar{q}_{\mathrm{R}}) + \nabla w\cdot k\nabla\vartheta\right] dV_{\mathrm{R}} - \int_{\partial\mathrm{B}} w(k\nabla\vartheta\cdot\mathbf{n}_{\mathrm{R}})\, dA_{\mathrm{R}}. \tag{B.41}$$

Recalling the prescribed heat flux boundary condition

$$-k\nabla\vartheta\cdot\mathbf{n}_{\mathrm{R}}=\breve{q}_{\mathrm{R}} \tag{B.42}$$

we finally arrive at

$$0=\int_{\mathrm{B}}\left[w(c\dot{\vartheta}-\bar{q}_{\mathrm{R}})+\nabla w\cdot k\nabla\vartheta\right]dV_{\mathrm{R}}+\int_{\mathcal{S}_q}w\breve{q}_{\mathrm{R}}\,dA_{\mathrm{R}}. \tag{B.43}$$

The body is approximated using finite elements $B=\sum\mathrm{B}^e$ and the trial solution for the temperature is interpolated inside each element by

$$\vartheta=\sum_A N^A\vartheta^A \tag{B.44}$$

with the index $A=1,2,...$ denoting the node of the element, ϑ^A denoting the nodal temperature, and N^A the shape functions. We employ a standard Galerkin approach, in that the weighting field is interpolated by the same shape functions, such that

$$w=\sum_A N^A w^A. \tag{B.45}$$

This yields the element-level relation

$$0=\int_{\mathrm{B}^e}\left[w^A N^A(c\dot{\vartheta}-\bar{q}_{\mathrm{R}})+w^A\nabla N^A\cdot k\nabla\vartheta\right]dV_{\mathrm{R}}+\int_{\mathcal{S}_q^e}w^A N^A\breve{q}_{\mathrm{R}}\,dA_{\mathrm{R}} \tag{B.46}$$

which must hold for all w^A. Therefore, we define the element level residual for the temperature as

$$R_\vartheta^A=\int_{\mathrm{B}^e}\left[N^A(c\dot{\vartheta}-\bar{q}_{\mathrm{R}})+\nabla N^A\cdot k\nabla\vartheta\right]dV_{\mathrm{R}}+\int_{\mathcal{S}_q^e}N^A\breve{q}_{\mathrm{R}}\,dA_{\mathrm{R}}. \tag{B.47}$$

The element stiffness is defined by

$$K_{\vartheta\vartheta}^{AB}=-\frac{\partial R_\vartheta^A}{\partial\vartheta^B} \tag{B.48}$$

which using the residual defined above is given by

$$\begin{aligned}K_{\vartheta\vartheta}^{AB}=&-\int_{\mathrm{B}^e}\Bigg[N^A\left(\frac{\partial c}{\partial\vartheta}\frac{\partial\vartheta}{\partial\vartheta^B}\dot{\vartheta}+c\frac{\partial\dot{\vartheta}}{\partial\vartheta}\frac{\partial\vartheta}{\partial\vartheta^B}-\frac{\partial\bar{q}_{\mathrm{R}}}{\partial\vartheta}\frac{\partial\vartheta}{\partial\vartheta^B}\right)\\&\qquad+\frac{\partial k}{\partial\vartheta}\frac{\partial\vartheta}{\partial\vartheta^B}\nabla N^A\cdot\nabla\vartheta+k\nabla N^A\cdot\frac{\partial}{\partial\vartheta}\frac{\partial\vartheta}{\partial\vartheta^B}\frac{\partial\vartheta}{\partial\mathbf{X}}\Bigg]dV_{\mathrm{R}}\\&-\int_{\mathcal{S}_q^e}N^A\frac{\partial\breve{q}_{\mathrm{R}}}{\partial\vartheta}\frac{\partial\vartheta}{\partial\vartheta^B}\,dA_{\mathrm{R}}\end{aligned} \tag{B.49}$$

which finally can be expressed as

$$K_{\vartheta\vartheta}^{AB} = -\int_{\mathrm{B}^e} \left[N^A N^B \left(\frac{\partial c}{\partial \vartheta}\dot{\vartheta} + c\frac{\partial \dot{\vartheta}}{\partial \vartheta} - \frac{\partial \bar{q}_{\mathrm{R}}}{\partial \vartheta} \right) + \frac{\partial k}{\partial \vartheta} N^B \nabla N^A \cdot \nabla \vartheta + k \nabla N^A \cdot \nabla N^B \right] dV_{\mathrm{R}}$$
$$- \int_{\mathcal{S}_q^e} N^A N^B \frac{\partial \breve{q}_{\mathrm{R}}}{\partial \vartheta}\, dA_{\mathrm{R}} \tag{B.50}$$

B.4 Variational formulation of the microscopic force balance

The microvariable solution variable is governed by the partial differential equation for the microscopic force balance (2.243), the strong form of which with appropriate boundary conditions is given by

$$\left.\begin{array}{rcll} e^p - l^2 \Delta e^p & = & \bar{\epsilon}^p & \text{on} \quad \mathrm{B} \\ e^p & = & \breve{e}^p & \text{on} \quad \mathcal{S}_{e^p} \\ \gamma(\nabla e^p) \cdot \mathbf{n}_{\mathrm{R}} & = & \breve{\chi} & \text{on} \quad \mathcal{S}_{\chi} \end{array}\right\} \tag{B.51}$$

with e^p the microvariable strain and l an energetic length scale in the theory. Further, on the surface $\mathcal{S}_{e^p}$ we prescribe the microscopic strain, and on the surface $\mathcal{S}_{\chi}$ the microscopic traction. To find the weak form of (B.51) we multiply by a test function w and integrate over the body

$$0 = \int_{\mathrm{B}} w \left[e^p - l^2 \mathrm{Div}\,(\nabla e^p) - \bar{\epsilon}^p \right] dV_{\mathrm{R}} \tag{B.52}$$

then using the identity

$$\alpha \mathrm{Div}\,(\mathbf{u}) = \mathrm{Div}\,(\alpha \mathbf{u}) - \nabla \alpha \cdot \mathbf{u} \tag{B.53}$$

we obtain

$$0 = \int_{\mathrm{B}} \left[w(e^p - \bar{\epsilon}^p) - l^2 \mathrm{Div}\,(w \nabla e^p) + l^2 \nabla w \cdot \nabla e^p \right] dV_{\mathrm{R}} \tag{B.54}$$

and using the divergence theorem

$$0 = \int_{\mathrm{B}} \left[w(e^p - \bar{\epsilon}^p) + l^2 \nabla w \cdot \nabla \bar{\epsilon}^p \right] dV_{\mathrm{R}} - \int_{\partial \mathrm{B}} l^2 (w \nabla e^p) \cdot \mathbf{n}_{\mathrm{R}}\, dA_{\mathrm{R}}. \tag{B.55}$$

Recalling the prescribed microscopic traction boundary condition

$$(\nabla e^p) \cdot \mathbf{n}_{\mathrm{R}} = \breve{\chi} \tag{B.56}$$

we finally arrive at

$$0 = \int_{\mathrm{B}} \left[w(e^p - \bar{\epsilon}^p) + l^2 \nabla w \cdot \nabla e^p \right] dV_{\mathrm{R}} - \int_{\mathcal{S}_{\chi}} w l^2 \breve{\chi}\, dA_{\mathrm{R}}. \tag{B.57}$$

The body is approximated using finite elements $B = \sum \mathrm{B}^e$ and the trial solution for the microvariable is interpolated inside each element by

$$e^p = \sum_A N^A e^{p\,A} \tag{B.58}$$

with the index $A = 1, 2, ...$ denoting the nodes of the element, $e^{p\,A}$ denoting the nodal microscopic strain, and N^A the shape functions. We employ a standard Galerking approach, in that the weighting field is interpolated by the same shape functions, such that

$$w = \sum_A N^A w^A. \tag{B.59}$$

This yields the element-level relation

$$0 = \int_{\mathrm{B}^e} \left[w^A N^A (e^p - \bar{e}^p) + l^2 w^A \nabla N^A \cdot \nabla e^p \right] dV_{\mathrm{R}} - \int_{\mathcal{S}^e_{\breve{\chi}}} w^A N^A l^2 \breve{\chi}\, dA_{\mathrm{R}} \tag{B.60}$$

which must hold for all w^A. Therefore, we define the element level residual for the microvariable as

$$R^A_{e^p} = \int_{\mathrm{B}^e} \left[N^A (e^p - \bar{e}^p) + l^2 \nabla N^A \cdot \nabla e^p \right] dV_{\mathrm{R}} - \int_{\mathcal{S}^e_{\breve{\chi}}} N^A l^2 \breve{\chi}\, dA_{\mathrm{R}}. \tag{B.61}$$

The element stiffness is defined by

$$K^{AB}_{e^p e^p} = -\frac{\partial R^A_{e^p}}{\partial e^{p\,B}} \tag{B.62}$$

which using the residual defined above is given by

$$K^{AB}_{e^p e^p} = -\int_{\mathrm{B}^e} \left[N^A \frac{\partial e^p}{\partial e^{p\,B}} + l^2 \nabla N^A \cdot \frac{\partial}{\partial e^{p\,B}} \frac{\partial e^p}{\partial \mathbf{X}} \right] dV_{\mathrm{R}} + \int_{\mathcal{S}^e_{\breve{\chi}}} N^A l^2 \frac{\partial \breve{\chi}}{\partial e^p} \frac{\partial e^p}{\partial e^{p\,B}}\, dA_{\mathrm{R}} \tag{B.63}$$

which finally can be expressed as

$$K^{AB}_{e^p e^p} = -\int_{\mathrm{B}^e} \left[N^A N^B + l^2 \nabla N^A \cdot \nabla N^B \right] dV_{\mathrm{R}} + \int_{\mathcal{S}^e_{\breve{\chi}}} N^A N^B l^2 \frac{\partial \breve{\chi}}{\partial e^p}\, dA_{\mathrm{R}}. \tag{B.64}$$

B.5 Time integration procedure

In this section, following Weber and Anand (1990), we develop a semi-implicit time integration procedure for the specialized theory presented in this paper. The evolution equation $\dot{\mathbf{F}}^p = \mathbf{D}^p \mathbf{F}^p$, reiterated from (2.162), is integrated by means of the *exponential map* as

$$\mathbf{F}^p_{n+1} = \exp\left(\Delta t \mathbf{D}^p_{n+1}\right) \mathbf{F}^p_n, \qquad \mathbf{D}^p_{n+1} = \hat{\mathbf{D}}^p_{n+1}(\mathbf{M}^e_{n+1}, Y_{n+1}, \vartheta, C) \tag{B.65}$$

where the flow resistance Y is integrated as

$$Y_{n+1} = Y_{\mathrm{conv},n+1} + Z(\bar{e}^p{}_{n+1} - e^p_{n+1}) + B(\bar{e}^p{}_{n+1} - e^p_{n+1}) \tag{B.66}$$

with

$$Y_{\text{conv},n+1} = Y_{\text{conv},n} + \dot{Y}_{\text{conv},n+1}\Delta t \tag{B.67}$$

and

$$\dot{Y}_{\text{conv},n+1} = \begin{cases} H_{\text{hard}}\left(1 - \dfrac{Y_{\text{conv},n}}{Y_{\text{sat}}}\right)\dot{\bar{\epsilon}}^{p}{}_{n+1} & \text{if} \quad C_{n+1} < C_c, \\ H_{\text{hard}}\left(1 - \dfrac{Y_{\text{conv},n}}{Y_{\text{sat}}}\right)\dot{\bar{\epsilon}}^{p}{}_{n+1} - H_{\text{soft}}\dot{\bar{\epsilon}}^{p}{}_{n+1} & \text{if} \quad C_{n+1} \geq C_c. \end{cases} \tag{B.68}$$

Using $\mathbf{F}^e = \mathbf{F}\mathbf{F}^{p-1}$, the elastic distortion at the end of the step is given by

$$\mathbf{F}^e_{n+1} = \mathbf{F}^{e\,\text{trial}}\exp(-\Delta t\mathbf{D}^p_{n+1}) \tag{B.69}$$

where

$$\mathbf{F}^{e\,\text{trial}} \overset{\text{def}}{=} \mathbf{F}_{n+1}\mathbf{F}^{p-1}_{n} \tag{B.70}$$

is a *trial* value of the elastic deformation gradient. The tensors $\mathbf{F}^e_{n+1}$ and $\mathbf{F}^{e\,\text{trial}}$ admit the polar decompositions

$$\mathbf{F}^e_{n+1} = \mathbf{R}^e_{n+1}\mathbf{U}^e_{n+1}, \quad \text{and} \quad \mathbf{F}^{e\,\text{trial}} = \mathbf{R}^{e\,\text{trial}}\mathbf{U}^{e\,\text{trial}}, \tag{B.71}$$

then using (B.69) and (B.71) and rearranging, we obtain

$$\mathbf{R}^e_{n+1}\mathbf{U}^e_{n+1}\exp(\Delta t\mathbf{D}^p_{n+1}) = \mathbf{R}^{e\,\text{trial}}\mathbf{U}^{e\,\text{trial}}. \tag{B.72}$$

Since

$$\mathbf{D}^p_{n+1} = \hat{\mathbf{D}}^p_{n+1}(\mathbf{M}^e_{n+1}, Y_{n+1}, \vartheta, C) \tag{B.73}$$

is an isotropic function of its arguments, the principal directions of $\hat{\mathbf{D}}^p_{n+1}$ are the same as those of $\mathbf{M}^e_{n+1}$. Further since the function

$$\mathbf{M}^e_{n+1} = \hat{\mathbf{M}}^e_{n+1}(\mathbf{U}^e_{n+1}) \tag{B.74}$$

is also isotropic, the principal directions of $\hat{\mathbf{M}}^e_{n+1}$ are the same as those of $\mathbf{U}^e_{n+1}$. Hence the principal directions of the isotropic function $\hat{\mathbf{D}}^p_{n+1}$ are the same as those of $\mathbf{U}^e_{n+1}$ and as a result,

$$\mathbf{U}^e_{n+1}\exp(\Delta t\mathbf{D}^p_{n+1}) \quad \textbf{is symmetric}. \tag{B.75}$$

Then, because of the *uniqueness* of the polar decomposition theorem

$$\mathbf{R}_{n+1} = \mathbf{R}^{e\,\text{trial}}, \tag{B.76}$$

$$\mathbf{U}^e_{n+1}\exp(\Delta t\mathbf{D}^p_{n+1}) = \mathbf{U}^{e\,\text{trial}}, \tag{B.77}$$

equation (B.77) implies that $\mathbf{U}^e_{n+1}$ and $\mathbf{U}^{e\,\text{trial}}$ have the same principal directions. Thus taking the logarithm on both sides and rearranging we have

$$\mathbf{E}^e_{n+1} = \mathbf{E}^{e\,\text{trial}} - \Delta t\mathbf{D}^p_{n+1}, \qquad \text{where} \qquad \mathbf{E}^{e\,\text{trial}} = \ln\mathbf{U}^{e\,\text{trial}}_{n+1}, \tag{B.78}$$

which, since $\mathbf{D}^p$ is deviatoric, yields that the trace of the elastic logarithmic strain is equal to that of the trial elastic logarithmic strain

$$\operatorname{tr}\mathbf{E}^e_{n+1} = \operatorname{tr}\mathbf{E}^{e\,\mathrm{trial}}. \tag{B.79}$$

Using (B.79) we may update the lattice hydrogen concentration C_L as

$$C_{L,n+1} = N_L \exp\left(\frac{\mu_{L,n+1} - \mu^0_L + 3K\beta(\operatorname{tr}\mathbf{E}^{e\,\mathrm{trial}})}{R\vartheta_{n+1}}\right). \tag{B.80}$$

Recall from $(2.192)_1$ that the stress strain relation is given by

$$\mathbf{M}^e = 2G\mathbf{E}^e_0 + K(\operatorname{tr}\mathbf{E}^e)\mathbf{1} - 3K\alpha(\vartheta - \vartheta_0)\mathbf{1} - 3K\beta(C - C_0)\mathbf{1}, \tag{B.81}$$

from (2.20) that the plastic stretching is given by

$$\mathbf{D}^p = \sqrt{3/2}\,\dot{\bar{\epsilon}}^p\mathbf{N}^p, \tag{B.82}$$

and from (2.88) and (2.89) that the direction of plastic flow is given by

$$\mathbf{N}^p = \sqrt{3/2}\left(\frac{\mathbf{M}^e_0}{\bar{\sigma}}\right). \tag{B.83}$$

Then, applying (B.78) to the deviatoric and trace parts of the stress strain relation (B.81) and recalling that $\mathbf{D}^p$ is deviatoric yields the important stress update equations

$$\mathbf{M}^e_{0,n+1} = \mathbf{M}^{e\,\mathrm{trial}}_0 - 2G\Delta t\mathbf{D}^p_{n+1} \tag{B.84}$$

$$\operatorname{tr}\mathbf{M}^e_{n+1} = \operatorname{tr}\mathbf{M}^{e\,\mathrm{trial}} \tag{B.85}$$

with the deviatoric and trace parts of the trial Mandell stress define by

$$\mathbf{M}^{e\,\mathrm{trial}}_0 \stackrel{\mathrm{def}}{=} 2G\mathbf{E}^{e\,\mathrm{trial}}_0 \tag{B.86}$$

$$\operatorname{tr}\mathbf{M}^{e\,\mathrm{trial}} \stackrel{\mathrm{def}}{=} 3K(\operatorname{tr}\mathbf{E}^{e\,\mathrm{trial}}) - 9K\alpha(\vartheta_{n+1} - \vartheta_0) - 9K\beta(C_{n+1} - C_0) \tag{B.87}$$

Finally, using (B.82), the stress update (B.84) for the deviatoric Mandell stress may be written as

$$\mathbf{M}^e_{0,n+1} = \mathbf{M}^{e\,\mathrm{trial}}_0 - \sqrt{6}(\dot{\bar{\epsilon}}^p{}_{n+1}\Delta t)\mathbf{N}^p_{n+1}, \tag{B.88}$$

which may be rearranged as

$$\left(\sqrt{2/3}\bar{\sigma}_{n+1} + \sqrt{6}G(\dot{\bar{\epsilon}}^p{}_{n+1}\Delta t)\right)\mathbf{N}^p_{n+1} = \mathbf{M}^{e\,\mathrm{trial}}_0. \tag{B.89}$$

Let

$$\bar{\sigma}^{\text{trial}} = \sqrt{3/2}\,|\mathbf{M}_0^{e\,\text{trial}}|, \tag{B.90}$$

$$\mathbf{N}^{p\,\text{trial}} = \frac{\mathbf{M}_0^{e\,\text{trial}}}{|\mathbf{M}_0^{e\,\text{trial}}|}. \tag{B.91}$$

Then (B.89) may be written as

$$\left(\sqrt{2/3}\,\bar{\sigma}_{n+1} + \sqrt{6}\,G(\dot{\bar{\epsilon}}^p{}_{n+1}\Delta t)\right)\mathbf{N}^p_{n+1} = \sqrt{2/3}\bar{\sigma}^{\text{trial}}\mathbf{N}^{p\,\text{trial}} \tag{B.92}$$

which yields

$$\mathbf{N}^p_{n+1} = \mathbf{N}^{p\,\text{trial}}, \tag{B.93}$$

$$\bar{\sigma}_{n+1} = \bar{\sigma}^{\text{trial}} - 3G(\dot{\bar{\epsilon}}^p{}_{n+1}\Delta t). \tag{B.94}$$

Thus, equation (B.93) shows that *the direction of plastic flow at the end of the step is determined by the trial direction of plastic flow.*

Next, the implicit form of the flow condition (2.221) is

$$\bar{\sigma}_{n+1} = Y_{n+1}(\bar{\epsilon}^p{}_{n+1}, \vartheta_{n+1}, C_{n+1}), \quad \text{where} \quad \bar{\epsilon}^p{}_{n+1} = \bar{\epsilon}^p{}_n + \dot{\bar{\epsilon}}^p{}_{n+1}\Delta t, \tag{B.95}$$

and where $C_{n+1} = C_{L,n+1} + C_{T,n+1}$, the lattice hydrogen concentration at the end of the increment $C_{L,n+1}$ is known, and trapped hydrogen concentration at the end of the increment $C_{T,n+1}$ depends on $\bar{\epsilon}^p{}_{n+1}$ through (viz. (2.206))

$$C_{T,n+1} = \frac{N_{T,n+1}}{1 + \dfrac{N_L}{K_{T,n+1}C_{L,n+1}}}, \tag{B.96}$$

with

$$K_{T,n+1} = \exp\left(\frac{W_B}{R\vartheta_{n+1}}\right) \quad \text{and} \quad N_{T,n+1} = \hat{N}_{T,n+1}(\bar{\epsilon}^p{}_{n+1}). \tag{B.97}$$

Finally, using (B.95) in (B.94) gives the following important implicit equation for $\dot{\bar{\epsilon}}^p{}_{n+1}$:

$$g(\dot{\bar{\epsilon}}^p{}_{n+1}) = \bar{\sigma}^{\text{trial}} - 3G(\dot{\bar{\epsilon}}^p{}_{n+1}\Delta t) - Y_{n+1}(\bar{\epsilon}^p{}_{n+1}, \vartheta_{n+1}, C_{n+1}) = 0 \tag{B.98}$$

Once a solution for $\dot{\bar{\epsilon}}^p{}_{n+1}$ has been found we can update all necessary quantities as follows.

The update for $\mathbf{F}^p$ is obtained from

$$\mathbf{F}^p_{n+1} = \exp(\Delta t\mathbf{D}^p_{n+1})\mathbf{F}^p_n, \qquad \text{with} \qquad \mathbf{D}^p_{n+1} = \sqrt{3/2}\dot{\bar{\epsilon}}^p\mathbf{N}^{p\,\text{trial}} \tag{B.99}$$

where $\exp(\Delta t\mathbf{D}^p_{n+1})$ is computed by taking the exponential of the eigenvalues of $\Delta t\mathbf{D}^p_{n+1}$. Once $\mathbf{F}^p_{n+1}$ has been computed the elastic deformation gradient is simply given by

$$\mathbf{F}^e_{n+1} = \mathbf{F}_{n+1}\mathbf{F}^{p-1}_{n+1}, \tag{B.100}$$

from which the logarithmic elastic strain $\mathbf{E}^e_{n+1}$ can be updated. The total hydrogen concentration is additively decomposable, viz. (2.64),

$$C_{n+1} = C_{L,n+1} + C_{T,n+1}, \tag{B.101}$$

where, recalling the constitutive equation (2.212), the lattice hydrogen concentration has already been update through

$$C_{L,n+1} = N_L \exp\left(\frac{\mu_{L,n+1} - \mu^0_L + 3K\beta(\operatorname{tr}\mathbf{E}^{e\,\text{trial}})}{R\vartheta_{n+1}}\right), \tag{B.102}$$

and, recalling equation (2.206), the trapped hydrogen concentration is updated as

$$C_{T,n+1} = \frac{N_{T,n+1}}{1 + \dfrac{N_L}{K_{T,n+1}C_{L,n+1}}}, \tag{B.103}$$

with

$$K_{T,n+1} = \exp\left(\frac{W_B}{R\vartheta}\right) \quad \text{and} \quad N_{T,n+1} = \hat{N}_{T,n+1}(\bar{\epsilon}^p{}_{n+1}). \tag{B.104}$$

Finally the Mandel stress can be updated as

$$\mathbf{M}^e_{n+1} = 2G\mathbf{E}^e_{0\,n+1} + K(\operatorname{tr}\mathbf{E}^e_{n+1}) - 3K\alpha(\vartheta_{n+1} - \vartheta_0)\mathbf{1} - 3K\beta(C_{n+1} - C_0)\mathbf{1} \tag{B.105}$$

and using (B.76) the Cauchy stress is given by

$$\mathbf{T}_{n+1} = \frac{1}{\det \mathbf{F}_{n+1}}(\mathbf{R}^{e\,\text{trial}})(\mathbf{M}^e_{n+1})(\mathbf{R}^{e\,\text{trial}})^{\top}. \tag{B.106}$$

B.5.1 Summary of time-integration procedure

Given: $\{\mathbf{T}_n,\ Y_n,\ \mathbf{F}^p_n,\ \bar{\epsilon}^p{}_n\}$, and $\{\mathbf{F}_{n+1}, \mathbf{F}_n, \vartheta_{n+1}, \vartheta_n, \mu_{n+1}, \mu_n\}$ at time t_n
Calculate: $\{\mathbf{T}_{n+1},\ Y_{n+1},\ \mathbf{F}^p_{n+1},\ \bar{\epsilon}^p{}_{n+1},\ C_{n+1},\ C_{L,n+1},\ C_{T,n+1}\}$ at time $t_{n+1} = t_n + \Delta t$

Step 1. Calculate the trial elastic deformation gradient

$$\mathbf{F}^{e\,\text{trial}} = \mathbf{F}_{n+1}\mathbf{F}^{p-1}_{n+1} \tag{B.107}$$

Step 2. Perform the polar decomposition

$$\mathbf{F}^{e\,\text{trial}} = \mathbf{R}^{e\,\text{trial}}\,\mathbf{U}^{e\,\text{trial}} \tag{B.108}$$

Step 3. Perform the spectral decomposition of $\mathbf{U}^{e\,\text{trial}}$ and calculate the trial logarithmic elastic strain

$$\mathbf{E}^{e\,\text{trial}} = \ln \mathbf{U}^{e\,\text{trial}} = \sum_{i=1}^{e} \ln \lambda_i^{e\,\text{trial}}\,\mathbf{r}_i^{e\,\text{trial}} \otimes \mathbf{r}_i^{e\,\text{trial}} \tag{B.109}$$

Step 4. Calculate the lattice hydrogen concentration at the end of the increment

$$C_{L,n+1} = N_L \exp\left(\frac{\mu_{L,n+1} - \mu_L^0 + 3K\beta(\mathrm{tr}\,\mathbf{E}^{e\,\mathrm{trial}})}{R\vartheta_{n+1}}\right), \tag{B.110}$$

Step 5. Calculate the deviatoric trial elastic stress

$$\mathbf{M}_0^{e\,\mathrm{trial}} = 2G\mathbf{E}_0^{e\,\mathrm{trial}} \tag{B.111}$$

Step 6. Calculate the trial equivalent tensile stress, and the trial direction of plastic flow

$$\bar{\sigma}^{\mathrm{trial}} = \sqrt{3/2}\,|\mathbf{M}_0^{e\,\mathrm{trial}}|, \tag{B.112}$$

$$\mathbf{N}^{p\,\mathrm{trial}} = \frac{\mathbf{M}_0^{e\,\mathrm{trial}}}{|\mathbf{M}_0^{e\,\mathrm{trial}}|}. \tag{B.113}$$

Step 7. Calculate $\dot{\bar{\epsilon}}^{p}{}_{n+1}$ by solving

$$g(\dot{\bar{\epsilon}}^{p}{}_{n+1}) = \bar{\sigma}^{\mathrm{trial}} - 3G(\dot{\bar{\epsilon}}^{p}{}_{n+1}\Delta t) - Y(\bar{\epsilon}^{p}{}_{n+1}, \vartheta_{n+1}, C_{n+1}) = 0 \tag{B.114}$$

with $\bar{\epsilon}^{p}{}_{n+1} = \bar{\epsilon}^{p}{}_{n} + \dot{\bar{\epsilon}}^{p}{}_{n+1}\Delta t$.

Step 8. Update $\mathbf{F}^p$

$$\mathbf{F}^p_{n+1} = \exp\left(\Delta t\mathbf{D}^p_{n+1}\right)\mathbf{F}^p_n, \quad \text{with} \quad \mathbf{D}^p_{n+1} = \sqrt{3/2}\,\dot{\bar{\epsilon}}^p\mathbf{N}^{p\,\mathrm{trial}} \tag{B.115}$$

Step 9. Update the elastic deformation gradient, perform the polar decomposition of the elastic deformation gradient, and calculate the elastic logarithmic strain

$$\mathbf{F}^e_{n+1} = \mathbf{F}_{n+1}\mathbf{F}^{p-1}_{n+1} \tag{B.116}$$

$$\mathbf{F}^e_{n+1} = \mathbf{R}^e_{n+1}\mathbf{U}^e_{n+1} \tag{B.117}$$

$$\mathbf{E}^e_{n+1} = \ln\mathbf{U}^e_{n+1} = \sum_{i=1}^{3}\ln\lambda_i^e\mathbf{r}_i^e \otimes \mathbf{r}_i^e \tag{B.118}$$

Step 10. Calculate the trapped and total hydrogen concentration

$$C_{T,n+1} = \frac{N_{T,n+1}}{1 + \dfrac{N_L}{K_{T,n+1}C_{L,n+1}}}, \tag{B.119}$$

with $K_{T,n+1} = \exp\left(\dfrac{W_B}{R\vartheta_{n+1}}\right)$, and $N_{T,n+1} = \hat{N}_{T,n+1}(\bar{\epsilon}^{p}{}_{n+1})$.

$$C_{n+1} = C_{L,n+1} + C_{T,n+1}. \tag{B.120}$$

Step 11. Update the Mandel stress

$$\mathbf{M}^e_{n+1} = 2G\mathbf{E}^e_{0\,n+1} + K(\operatorname{tr}\mathbf{E}^e_{n+1}) - 3K\alpha(\vartheta_{n+1} - \vartheta_0)\mathbf{1} - 3K\beta(C_{n+1} - C_0)\mathbf{1} \tag{B.121}$$

Step 12. Update the Cauchy stress

$$\mathbf{T}_{n+1} = \frac{1}{\det \mathbf{F}_{n+1}}(\mathbf{R}^{e\,\mathrm{trial}})(\mathbf{M}^e_{n+1})(\mathbf{R}^{e\,\mathrm{trial}})^{\top}. \tag{B.122}$$

Step 13. Update the flow resistance

$$Y_{n+1} = Y(\bar{\epsilon}^p{}_{n+1}, \vartheta_{n+1}, C_{n+1}) \tag{B.123}$$

B.6 Jacobian matrix

As outlined in Section B.1, in order to compute the stiffness for the balance of momentum we are required to compute

$$\mathcal{C}_{ijkn} = \frac{\partial T_{ij}}{\partial F_{kn}} \tag{B.124}$$

which is often called the Jacobian matrix. In this section we obtain an *estimate* for the Jacobian matrix. We note that Jacobian matrices are used only in the search for the global finite element solution, and though an approximate Jacobian might affect the rate of convergence, it will not affect the accuracy of our constitutive time-integration algorithm. We begin by approximating (B.124) by a derivative of the elastic Mandel stress with respect to the trial elastic strain, such that

$$\mathcal{C} = \frac{\partial \mathbf{T}_{n+1}}{\partial \mathbf{F}_{n+1}} \approx \frac{\partial \mathbf{M}^e_{n+1}}{\partial \mathbf{E}^{e\,\mathrm{trial}}_{n+1}}. \tag{B.125}$$

In a rate-independent theory we make use of different Jacobians for steps in which the deformation is purely elastic and steps in which there is plastic deformation that is,

$$\left.\begin{aligned} &\mathcal{C} = \mathcal{C}_{\mathrm{elastic}} \quad \text{if} \quad \bar{\sigma}^{\mathrm{trial}} \le 0, \\ &\mathcal{C} = \mathcal{C}_{\mathrm{plastic}} \quad \text{if} \quad \bar{\sigma}^{\mathrm{trial}} > 0 \quad \text{and} \quad \dot{\bar{\epsilon}}^p > 0. \end{aligned}\right\} \tag{B.126}$$

B.6.1 Elastic jacobian matrix

During elastic deformation $\mathbf{E}^e_{n+1} = \mathbf{E}^{e\,\mathrm{trial}}_{n+1}$ and we may write the stress strain relation $(2.192)_1$ as

$$\mathbf{M}^e_{n+1} = 2G\mathbf{E}^{e\,\mathrm{trial}}_{0,n+1} + K(\operatorname{tr}\mathbf{E}^{e\,\mathrm{trial}}_{n+1})\mathbf{1} - 3K\alpha(\vartheta_{n+1} - \vartheta_0)\mathbf{1} - 3K\beta(C_{n+1} - C_0)\mathbf{1} \tag{B.127}$$

with

$$C_{n+1} = C_{L,n+1} + C_{T,n+1}, \tag{B.128}$$

$$C_{L,n+1} = N_L \exp\left(\frac{\mu_{L,n+1} - \mu_L^0 + 3K\beta(\operatorname{tr}\mathbf{E}^e_{n+1})}{R\vartheta_{n+1}}\right), \tag{B.129}$$

$$C_{T,n+1} = \frac{N_{T,n+1}}{1 + \dfrac{N_L}{K_{T,n+1}C_{L,n+1}}}. \tag{B.130}$$

Since $\mathbf{E}^{e\,\text{trial}}_{n+1}$ enters $C_{T,n+1}$ through $C_{L,n+1}$ only

$$\frac{\partial C_{n+1}}{\partial \mathbf{E}^{e,\text{trial}}_{n+1}} = \frac{\partial C_{L,n+1}}{\partial \mathbf{E}^{e\,\text{trial}}_{n+1}} + \frac{\partial C_{T,n+1}}{\partial C_{L,n+1}}\frac{\partial C_{L,n+1}}{\partial \mathbf{E}^{e\,\text{trial}}_{n+1}} = \left(1 + \frac{\partial C_{T,n+1}}{\partial C_{L,n+1}}\right)\frac{\partial C_{L,n+1}}{\partial \mathbf{E}^{e\,\text{trial}}_{n+1}} \tag{B.131}$$

which, using equations (2.208) and (B.129), is given by

$$\frac{\partial C_{n+1}}{\partial \mathbf{E}^{e,\text{trial}}_{n+1}} = \left(1 + \frac{C_{T,n+1}(1-\theta_{T,n+1})}{C_{L,n+1}}\right) C_{L,n+1}\frac{3K\beta}{R\vartheta_{n+1}}\mathbf{1}. \tag{B.132}$$

The elastic jacobian is then simply given by

$$\mathcal{C}_{\text{elastic}} = 2G\left(\mathbb{I} - \frac{1}{3}\mathbf{1}\otimes\mathbf{1}\right) + \left(K - (C_L - C_T(1-\theta_T))\frac{(3K\beta)^2}{R\vartheta}\right)\mathbf{1}\otimes\mathbf{1}. \tag{B.133}$$

B.6.2 Plastic jacobian matrix

Recall from (B.93) in the time-integration procedure that

$$\mathbf{N}^p_{n+1} = \mathbf{N}^{p,\text{trial}} \tag{B.134}$$

which using the definition (B.83) and the definition of the deviator, leads to the update equation

$$\mathbf{M}^e_{0,n+1} = \left(\frac{\bar{\sigma}_{n+1}}{\bar{\sigma}^{\text{trial}}}\right)\mathbf{M}_0^{e\,\text{trial}} + \frac{1}{3}\operatorname{tr}(\mathbf{M}^{e\,\text{trial}})\mathbf{1} \tag{B.135}$$

then deriving with respect to the trial elastic strain

$$\begin{aligned}\mathcal{C}_{\text{plastic}} = {} & \frac{\sigma_{\bar{n}+1}}{\bar{\sigma}^{\text{trial}}}\frac{\partial \mathbf{M}_0^{e\,\text{trial}}}{\partial \mathbf{E}^{e\,\text{trial}}} + \frac{1}{3}\frac{\partial \operatorname{tr}(\mathbf{M}^{e\,\text{trial}})}{\partial \mathbf{E}^{e\,\text{trial}}}\mathbf{1} \\ & + \frac{1}{\bar{\sigma}^{\text{trial}}}\frac{\partial\bar{\sigma}_{n+1}}{\partial \mathbf{E}^{e\,\text{trial}}}\otimes\mathbf{M}_0^{e\,\text{trial}} - \frac{\bar{\sigma}_{n+1}}{(\bar{\sigma}^{\text{trial}})^2}\frac{\partial\bar{\sigma}^{\text{trial}}}{\partial \mathbf{E}^{e\,\text{trial}}}\otimes\mathbf{M}_0^{e\,\text{trial}}.\end{aligned} \tag{B.136}$$

Noting that $\mathbf{E}^{e\,\text{trial}}$ enters the update equations through $\bar{\sigma}^{\text{trial}}$ we may write

$$\frac{\partial\bar{\sigma}_{n+1}}{\partial \mathbf{E}^{e\,\text{trial}}} = \frac{\partial\bar{\sigma}_{n+1}}{\partial\bar{\sigma}^{\text{trial}}}\frac{\partial\bar{\sigma}^{\text{trial}}}{\partial \mathbf{E}^{e\,\text{trial}}}. \tag{B.137}$$

Using (B.137) and the definition of the trial Mandel stress (B.111), the plastic Jacobian matrix (B.136) may be rewritten as

$$\mathcal{C}_{\text{plastic}} = 2G\frac{\bar{\sigma}_{n+1}}{\bar{\sigma}^{\text{trial}}}\left(\mathbb{I} - \frac{1}{3}\mathbf{1}\otimes\mathbf{1}\right) + \left(K - (C_{L,n+1} + C_{T,n+1}(1-\theta_{T,n+1}))\frac{(3K\beta)^2}{R\vartheta_{n+1}}\right)\mathbf{1}\otimes\mathbf{1}$$
$$+ \left(\frac{\partial\bar{\sigma}_{n+1}}{\partial\bar{\sigma}^{\text{trial}}} - \frac{\bar{\sigma}_{n+1}}{\bar{\sigma}^{\text{trial}}}\right)\frac{\partial\bar{\sigma}^{\text{trial}}}{\partial\mathbf{M}_0^{e\,\text{trial}}}\otimes\frac{\mathbf{M}_0^{e\,\text{trial}}}{\bar{\sigma}^{\text{trial}}}. \tag{B.138}$$

For conciseness we define

$$\tilde{G} \overset{\text{def}}{=} \frac{\bar{\sigma}_{n+1}}{\bar{\sigma}^{\text{trial}}}G \quad \text{and}$$
$$\tilde{\mathcal{C}}_{\text{elastic}} \overset{\text{def}}{=} 2\tilde{G}\left(\mathbb{I} - \frac{1}{3}\mathbf{1}\otimes\mathbf{1}\right) + \left(K - (C_{L,n+1} + C_{T,n+1}(1-\theta_{T,n+1}))\frac{(3K\beta)^2}{R\vartheta_{n+1}}\right)\mathbf{1}\otimes\mathbf{1}, \tag{B.139}$$

such that (B.138) may be written as

$$\mathcal{C}_{\text{plastic}} = \tilde{\mathcal{C}}_{\text{elastic}} + \left(\frac{\partial\bar{\sigma}_{n+1}}{\partial\bar{\sigma}^{\text{trial}}} - \frac{\bar{\sigma}_{n+1}}{\bar{\sigma}^{\text{trial}}}\right)\frac{\partial\bar{\sigma}^{\text{trial}}}{\partial\mathbf{E}^{e\,\text{trial}}}\otimes\frac{\mathbf{M}_0^{e\,\text{trial}}}{\bar{\sigma}^{\text{trial}}}. \tag{B.140}$$

Next using the definition of $\bar{\sigma}^{\text{trial}}$, the chain-rule, and the fact that $\mathbf{N}^p$ is deviatoric

$$\begin{aligned}\frac{\partial\bar{\sigma}^{\text{trial}}}{\partial\mathbf{E}^{e\,\text{trial}}} &= \sqrt{\frac{3}{2}}\frac{\partial}{\partial\mathbf{E}^{e\,\text{trial}}}\left(\sqrt{\mathbf{M}_0^{e\,\text{trial}}:\mathbf{M}_0^{e\,\text{trial}}}\right)\\ &= \sqrt{\frac{3}{2}}\frac{\partial\mathbf{M}_0^{e\,\text{trial}}}{\partial\mathbf{E}^{e\,\text{trial}}}\frac{\mathbf{M}_0^{e\,\text{trial}}}{|\mathbf{M}_0^{e\,\text{trial}}|}\\ &= \sqrt{\frac{3}{2}}2G\left(\mathbb{I} - \frac{1}{3}\mathbf{1}\otimes\mathbf{1}\right)\mathbf{N}^{p\,\text{trial}}\\ &= \sqrt{\frac{3}{2}}2G\mathbf{N}^{p\,\text{trial}}.\end{aligned} \tag{B.141}$$

Using the result (B.141) and the fact that

$$\mathbf{N}^{p\,\text{trial}} = \sqrt{\frac{3}{2}}\frac{\mathbf{M}_0^{e\,\text{trial}}}{\bar{\sigma}^{\text{trial}}}, \tag{B.142}$$

we may rewrite the plastic Jacobian matrix (B.140) as

$$\mathcal{C}_{\text{plastic}} = \tilde{\mathcal{C}}_{\text{elastic}} + 2G\left(\frac{\partial\bar{\sigma}_{n+1}}{\partial\bar{\sigma}^{\text{trial}}} - \frac{\bar{\sigma}_{n+1}}{\bar{\sigma}^{\text{trial}}}\right)\mathbf{N}^{p\,\text{trial}}\otimes\mathbf{N}^{p\,\text{trial}}. \tag{B.143}$$

All that remains is to determine the derivative

$$\frac{\partial\bar{\sigma}_{n+1}}{\partial\bar{\sigma}^{\text{trial}}}. \tag{B.144}$$

First, we define an equivalent plastic strain increment as

$$\Delta\bar{\epsilon}^p{}_{n+1} = \dot{\bar{\epsilon}}^p{}_{n+1}\Delta t \quad \text{such that} \quad \bar{\epsilon}^p{}_{n+1} = \bar{\epsilon}^p{}_n + \Delta\bar{\epsilon}^p{}_{n+1} \tag{B.145}$$

and we rewrite the update equations for $\bar{\sigma}_{n+1}$ and $\Delta\bar{\epsilon}^p{}_{n+1}$ as

$$\left.\begin{aligned} \bar{\sigma}_{n+1} &= Y(\bar{\epsilon}^p{}_n + \Delta\bar{\epsilon}^p{}_{n+1}, \vartheta_{n+1}, C_{n+1}) \\ \Delta\bar{\epsilon}^p{}_{n+1} &= \frac{\bar{\sigma}^{\text{trial}} - \bar{\sigma}_{n+1}}{3G} \end{aligned}\right\} \tag{B.146}$$

respectively. Using the definitions

$$\mathbf{X} \overset{\text{def}}{=} \begin{Bmatrix} \bar{\sigma}_{n+1} \\ \Delta\bar{\epsilon}^p{}_{n+1} \end{Bmatrix}, \quad \text{and} \quad \mathbf{Y} \overset{\text{def}}{=} \left\{\bar{\sigma}^{\text{trial}}\right\}, \tag{B.147}$$

the system of equations (B.146) may be written as

$$\mathbf{X} = \mathbf{G}(\mathbf{X};\mathbf{Y}) \tag{B.148}$$

where

$$\mathbf{G} = \begin{Bmatrix} Y(\bar{\epsilon}^p{}_n + \Delta\bar{\epsilon}^p{}_{n+1}, \vartheta_{n+1}, C_{n+1}) \\ (\bar{\sigma}^{\text{trial}} - \bar{\sigma}_{n+1})/(3G) \end{Bmatrix}. \tag{B.149}$$

Differentiating (B.148) with respect to $\mathbf{Y}$ (at the solution point) we obtain

$$\frac{\partial \mathbf{X}}{\partial \mathbf{Y}} = \frac{\partial \mathbf{G}(\mathbf{X};\mathbf{Y})}{\partial \mathbf{Y}} + \frac{\partial \mathbf{G}(\mathbf{X};\mathbf{Y})}{\partial \mathbf{X}}\frac{\partial \mathbf{X}}{\partial \mathbf{Y}} \tag{B.150}$$

from which[1]

$$\frac{\partial \mathbf{X}}{\partial \mathbf{Y}} = \left[\mathcal{I} - \frac{\partial \mathbf{G}(\mathbf{X};\mathbf{Y})}{\partial \mathbf{X}}\right]^{-1} \frac{\partial \mathbf{G}(\mathbf{X};\mathbf{Y})}{\partial \mathbf{Y}}. \tag{B.151}$$

Straightforward calculations show

$$\frac{\partial \mathbf{G}(\mathbf{X};\mathbf{Y})}{\partial \mathbf{X}} = \begin{bmatrix} 0 & \left.\dfrac{\partial Y}{\partial \Delta\bar{\epsilon}^p{}_{n+1}}\right|_{\bar{\epsilon}^p{}_{n+1}} \\ \dfrac{1}{3G} & 0 \end{bmatrix}, \quad \text{and} \quad \frac{\partial \mathbf{G}(\mathbf{X},\mathbf{Y})}{\partial \mathbf{Y}} = \begin{bmatrix} 0 \\ \dfrac{1}{3G} \end{bmatrix}. \tag{B.152}$$

Let

$$H_{n+1} = \left.\frac{\partial Y(\bar{\epsilon}^p{}_n + \Delta\bar{\epsilon}^p{}_{n+1}, \vartheta_{n+1}, C_{n+1})}{\partial \Delta\bar{\epsilon}^p{}_{n+1}}\right|_{\bar{\epsilon}^p{}_{n+1}}, \tag{B.153}$$

then

$$\frac{\partial \mathbf{X}}{\partial \mathbf{Y}} = \frac{1}{1 + \dfrac{H_{n+1}}{3G}} \begin{bmatrix} 1 & H_{n+1} \\ -\dfrac{1}{3G} & 1 \end{bmatrix} \begin{bmatrix} 0 \\ \dfrac{1}{3G} \end{bmatrix}. \tag{B.154}$$

---

[1] Here $\mathcal{I}$ is the second-order identity matrix.

Finally, we obtain

$$\frac{\bar{\sigma}_{n+1}}{\bar{\sigma}^{\text{trial}}} = \left[\frac{\partial \mathbf{X}}{\partial \mathbf{Y}}\right]_1 = \frac{H_{n+1}}{3G + H_{n+1}} \tag{B.155}$$

and the plastic Jacobian matrix is given by

$$\mathcal{C}_{\text{plastic}} = \tilde{\mathcal{C}}_{\text{elastic}} - 2G\left(\frac{\bar{\sigma}_{n+1}}{\bar{\sigma}^{\text{trial}}} - \frac{H_{n+1}}{3G + H_{n+1}}\right)\mathbf{N}^{p\,\text{trial}} \otimes \mathbf{N}^{p\,\text{trial}}. \tag{B.156}$$

In the numerical implementation it might be useful to write (B.156 as

$$\mathcal{C}_{\text{plastic}} = \tilde{\mathcal{C}}_{\text{elastic}} - 2G\left(\frac{3G}{3G + H_{n+1}} - \frac{3G\dot{\bar{\epsilon}}^{p}{}_{n+1}\Delta t}{\bar{\sigma}^{\text{trial}}}\right)\mathbf{N}^{p\,\text{trial}} \otimes \mathbf{N}^{p\,\text{trial}}. \tag{B.157}$$